

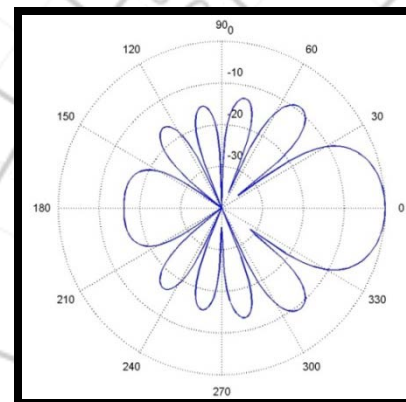
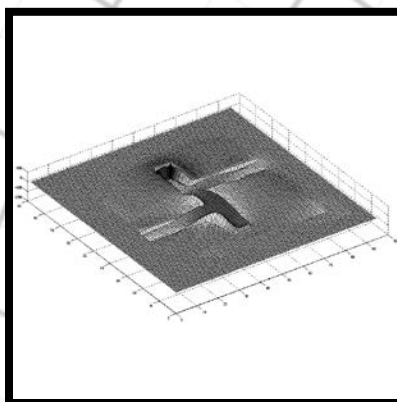
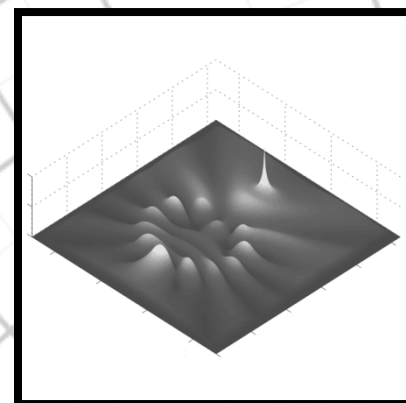
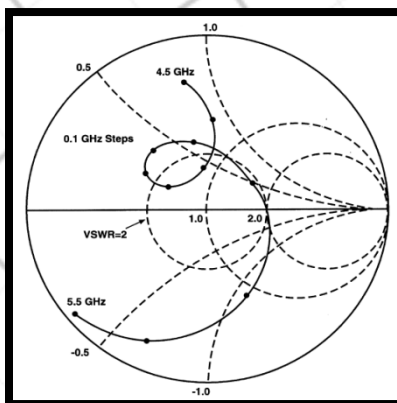
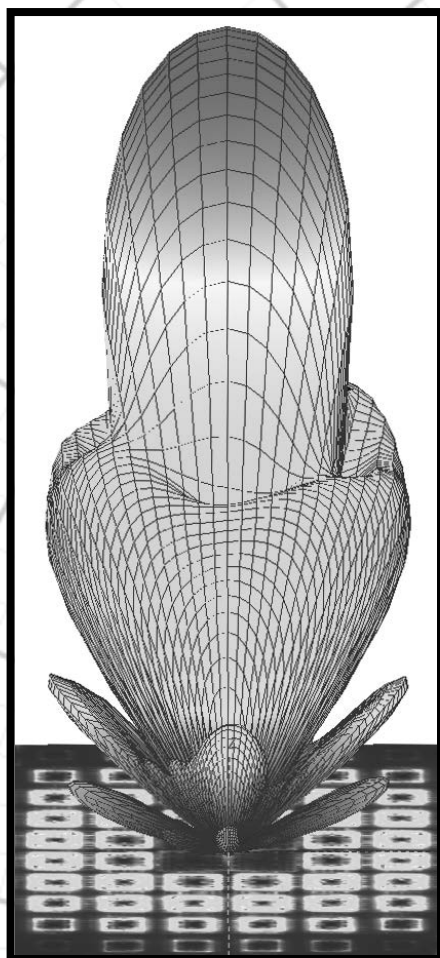
Applied Computational Electromagnetics Society

Journal



July 2012

Vol. 27 No. 7



ISSN 1054-4887

GENERAL PURPOSE AND SCOPE: The Applied Computational Electromagnetics Society (*ACES*) Journal hereinafter known as the *ACES Journal* is devoted to the exchange of information in computational electromagnetics, to the advancement of the state-of-the art, and the promotion of related technical activities. The primary objective of the information exchange is to inform the scientific community on the developments of new computational electromagnetics tools and their use in electrical engineering, physics, or related areas. The technical activities promoted by this publication include code validation, performance analysis, and input/output standardization; code or technique optimization and error minimization; innovations in solution technique or in data input/output; identification of new applications for electromagnetics modeling codes and techniques; integration of computational electromagnetics techniques with new computer architectures; and correlation of computational parameters with physical mechanisms.

SUBMISSIONS: The *ACES Journal* welcomes original, previously unpublished papers, relating to applied computational electromagnetics. Typical papers will represent the computational electromagnetics aspects of research in electrical engineering, physics, or related disciplines. However, papers which represent research in applied computational electromagnetics itself are equally acceptable.

Manuscripts are to be submitted through the upload system of *ACES* web site <http://aces.ee.olemiss.edu> See "Information for Authors" on inside of back cover and at *ACES* web site. For additional information contact the Editor-in-Chief:

Dr. Atef Elsherbeni
Department of Electrical Engineering
The University of Mississippi
University, MS 386377 USA
Phone: 662-915-5382
Email: atef@olemiss.edu

SUBSCRIPTIONS: All members of the Applied Computational Electromagnetics Society are entitled to access and download the *ACES Journal* any published journal article available at <http://aces.ee.olemiss.edu>. Printed issues of the *ACES Journal* are delivered to institutional members. Each author of published papers receives a printed issue of the *ACES Journal* in which the paper is published.

Back issues, when available, are \$50 each. Subscription to *ACES* is through the web site. Orders for back issues of the *ACES Journal* and change of address requests should be sent directly to *ACES* office at:

Department of Electrical Engineering
The University of Mississippi
University, MS 386377 USA
Phone: 662-915-7231
Email: aglisson@olemiss.edu

Allow four weeks advance notice for change of address. Claims for missing issues will not be honored because of insufficient notice, or address change, or loss in the mail unless the *ACES* office is notified within 60 days for USA and Canadian subscribers, or 90 days for subscribers in other countries, from the last day of the month of publication. For information regarding reprints of individual papers or other materials, see "Information for Authors".

LIABILITY. Neither *ACES*, nor the *ACES Journal* editors, are responsible for any consequence of misinformation or claims, express or implied, in any published material in an *ACES Journal* issue. This also applies to advertising, for which only camera-ready copies are accepted. Authors are responsible for information contained in their papers. If any material submitted for publication includes material which has already been published elsewhere, it is the author's responsibility to obtain written permission to reproduce such material.

**APPLIED
COMPUTATIONAL
ELECTROMAGNETICS
SOCIETY
JOURNAL**

July 2012
Vol. 27 No. 7
ISSN 1054-4887

The ACES Journal is abstracted in INSPEC, in Engineering Index, DTIC, Science Citation Index Expanded, the Research Alert, and to Current Contents/Engineering, Computing & Technology.

The illustrations on the front cover have been obtained from the research groups at the Department of Electrical Engineering, The University of Mississippi.

THE APPLIED COMPUTATIONAL ELECTROMAGNETICS SOCIETY

<http://aces.ee.olemiss.edu>

EDITOR-IN-CHIEF

Atef Elsherbeni

University of Mississippi, EE Dept.
University, MS 38677, USA

ASSOCIATE EDITORS-IN-CHIEF

Sami Barmada

University of Pisa, EE Dept.
Pisa, Italy, 56126

Fan Yang

University of Mississippi, EE Dept.
University, MS 38677, USA

Mohamed Bakr

McMaster University, ECE Dept.
Hamilton, ON, L8S 4K1, Canada

Yasushi Kanai

Niigata Inst. of Technology
Kashiwazaki, Japan

Mohammed Hadi

Kuwait University, EE Dept.
Safat, Kuwait

Mohamed Abouzahra

MIT Lincoln Laboratory
Lexington, MA, USA

EDITORIAL ASSISTANTS

Matthew J. Inman

University of Mississippi, EE Dept.
University, MS 38677, USA

Anne Graham

University of Mississippi, EE Dept.
University, MS 38677, USA

EMERITUS EDITORS-IN-CHIEF

Duncan C. Baker

EE Dept. U. of Pretoria
0002 Pretoria, South Africa

Allen Glisson

University of Mississippi, EE Dept.
University, MS 38677, USA

David E. Stein

USAF Scientific Advisory Board
Washington, DC 20330, USA

Robert M. Bevensee

Box 812
Alamo, CA 94507-0516, USA

Ahmed Kishk

University of Mississippi, EE Dept.
University, MS 38677, USA

EMERITUS ASSOCIATE EDITORS-IN-CHIEF

Alexander Yakovlev

University of Mississippi, EE Dept.
University, MS 38677, USA

Erdem Topsakal

Mississippi State University, EE Dept.
Mississippi State, MS 39762, USA

EMERITUS EDITORIAL ASSISTANTS

Khaled ElMaghoub

University of Mississippi, EE Dept.
University, MS 38677, USA

Mohamed Al Sharkawy

Arab Academy for Science and
Technology, ECE Dept.
Alexandria, Egypt

Christina Bonnington

University of Mississippi, EE Dept.
University, MS 38677, USA

JULY 2012 REVIEWERS

**Ahmed Abdelrahman
Iftikhar Ahmed
Abdul Ali Babar
Mohamed Bakr
Toni Björninen
Ru-shan Chen
Mohammed Hadi
Mario-Alberto Ibarra-Manzano
Arkom Kaewrawang
Fadi Khalil**

**Sébastien Lalléchère
Kai-Fong Lee
Samir Mahmoud
Alexei Maradudin
Zahéra Mekkioui
Adam Mock
Andrew Peterson
Mehdi Salehi
Yury Shestopalov
Joshua Wilson**

THE APPLIED COMPUTATIONAL ELECTROMAGNETICS SOCIETY
JOURNAL

Vol. 27 No. 7

July 2012

TABLE OF CONTENTS

“Analysis of Composite Scattering from a Target Above/Below a Dielectric Rough Surface using Higher Order Basis Functions” Y. An, R. S. Chen, P. Xu, Z. Liu, and L. Zha.....	541
“The Meshless Local Boundary Equation Method” B. Honarbakhsh and A. Tavakoli.....	550
“PEC Condition Implementation for the Novel Weakly Conditionally Stable Finite-Difference Time-Domain Method” J. Chen, J. Wang, and C. Tian.....	561
“Analysis and Application of Inverse Detecting Method Based on Local Electric Field” Z. Zhang, Z. Zhu, Q. Xin, X. Xie, J. Lei, and S. Huang.....	566
“Low RCS Antenna Design Using Genetic Algorithm Combined with Tabu List” X. Zhu, W. Shao, and J. L. Li.....	574
“A Novel Dual Narrow Band-Notched CPW-Fed UWB Slot Antenna with Parasitic Strips” X. L. Ma, W. Shao, and G. Q. He.....	581
“Application of Inductive Loadings for the Dual and Broad Banding of CPW-Fed Ring Antennas” H. Oraizi and B. Rezaei.....	587
“Accurate Modeling of a Patterned Ground and its Application to Microwave Filters” W. Shao and J. L. Li.....	596
“Scattering by Chiral Lossy Metamaterial Elliptic Cylinders” A. K. Hamid.....	603
“Effects of Surface Roughness on Lossy Rectangular Waveguide” J. Chen and B. Huang.....	610

Analysis of Composite Scattering from a Target Above/Below a Dielectric Rough Surface using Higher Order Basis Functions

Yuyuan An¹, Rushan Chen¹, Pingping Xu¹, Zhiwei Liu², and Liping Zha¹

¹Department of Communication Engineering
Nanjing University of Science and Technology, Nanjing, 210094, China
ayy.2@163.com, eerschen@njust.edu.cn, xupingping921@126.com, daisy918@163.com

²School of Information Engineering
East China Jiaotong University, Nanchang, 330013, China
zwliu1982@hotmail.com

Abstract — In this paper, the validity of four types of higher order basis functions for analyzing the 3D EM scattering from the target and dielectric rough surface is investigated. Although the higher order basis functions can reduce the number of unknowns significantly, the iterative solution time may increase with the order of the basis because the matrix condition numbers deteriorates with the basis order increase. This may be relative to: (a) The truncation of the dielectric rough surface and the interaction between the object and the rough surface; (b) the properties of the basis functions adopted. In this paper, a variety of models including a rough surface only, an object above or below the rough surface are investigated with different higher order basis functions. The program is based on the Poggio-Miller-Chang-Harrington-Wu-Tsai (PMCHW) integral equations. The multilevel fast multipole algorithm (MLFMA) and flexible generalized minimal residual (FGMRES) techniques are used to further accelerate the iteration solution.

Index Terms — Electromagnetic scattering, higher order basis functions, MLFMA, rough surface.

I. INTRODUCTION

Electromagnetic scattering from dielectric rough surfaces has a large number of applications, such as remote sensing, radar surveillance, and ground-penetration radar probing [1-9, 29]. Specific examples include detection of landmines

and remote sensing of soil moisture content to retrieve snow depth. Numerical simulation of the combined target and rough surface model is complicated by the interactions between the target and the rough surface background [1]. During the past few decades, both the approximate and rigorous methods have been developed to tackle this problem. Among the approximate methods, some are based on small perturbation method (SPM) [10], Kirchhoff approximation (KA) [3], small slope approximation (SSA) [11] and so on. However, the height value must be very small compared to the electromagnetic wave length in the SPM; the radius of the surface must be larger than a wavelength in the KA; the slope must be small and the height must be moderate for the first order in the SSA.

Numerical solution, on the other hand, is a rigorous approach which can deal with most of the cases without considering the profile of the rough surfaces. For the 2D problems, the generalized forward backward method with spectral acceleration algorithm (GFBM/SAA) [12], the finite element method (FEM) [13], the extended boundary condition method (EBCM) [33], and the steepest descent-fast multipole algorithm have been successfully used to the target and rough surface composite model. However, scattering from a 3D target and rough surface composite model is much more complicated than in a 2D case because of the large computational complexity [4]. Till now, only very few reports have been found for the 3D case, e.g. the UV

method [4], the FDTD method [14, 30], and the steepest descent-fast multipole method (SDFMM) [2,6].

In order to reduce the computational complexity, some efficient algorithms have been developed. The sparse matrix flat surface iterative approach (SMFSIA) [15, 16] takes advantage of the fact that rough surfaces are “nearly” planar. In this approach, the Green’s function for the weak matrix elements has been expanded in a Taylor’s series about the flat surface, which maps the problem to a flat 2D surface. The FFT technique is then used to accelerate the matrix-vector product for the Toeplitz structure of the interaction matrix on the flat surface. The complexity of the SMFSIA is $O(N \log N)$. Another approach is SDFMM [31], which has expressed the free-space dyadic Green’s function in terms of a rapidly converging Sommerfeld steepest descent integral. The source and observation points are evaluated efficiently by using a multilevel FMM-like algorithm based on inhomogeneous plane wave expansion. The time and memory complexity are $O(N)$.

There is still an efficient approach that is based on the consideration of basis functions [7] [17-18, 34-38]. For example, the characteristic basis function method (CBFM) [7] proposed for electromagnetic scattering over rough terrain profiles, is based on the constructing of high-level basis functions on macro-domains. The higher order hierarchical basis functions [17-18] have been used to analyze the electromagnetic scattering from breaking waves [19].

In this paper, four types of higher order basis functions, that is, the hierarchical tangential vector basis functions [20, 35-36] with curvilinear triangle patch mesh, the higher order hierarchical basis functions [17-18] with curvilinear quadrilateral patch mesh, and the maximally orthogonalized higher order basis functions [21] with curvilinear quadrilateral patch mesh are used to analyze the electromagnetic scattering from the target and dielectric rough surface. The validities of these functions are compared. To the knowledge of the author, the higher order basis functions have not been used to analyze scattering from rough surfaces.

The remainder of this paper is organized as follows. In Section II, theory and formulations are discussed. Numerical results are presented and

discussed in Section III. Section IV concludes this paper. The time factor $e^{j\omega t}$ is assumed and suppressed throughout this paper.

II. THEORY AND FORMULATION

A. Rough surface modeling and PMCHW integral equation

In practical cases, in order to eliminate the edge effects caused by truncation of the finite surface length, the tapered wave [16] is usually employed. Figure 1 shows the geometry of the proposed problem. The width of the tapered wave should be large enough to illuminate upon the surface. The incident electric and magnetic fields are \mathbf{E}^{inc} and \mathbf{H}^{inc} . Region 1 and Region 2 are characterized by medium parameters (ϵ_1, μ_1) and (ϵ_2, μ_2) , respectively. The equivalent electric and magnetic surface currents $\mathbf{J}(\mathbf{r})$ and $\mathbf{M}(\mathbf{r})$ are impressed on the rough surface. For simplicity, the rough surface without object is considered here, the formulations for an object under a dielectric rough surface can be found in references [2, 23]. To obtain \mathbf{J} and \mathbf{M} , the PMCHW [5, 22] formulation enforces the continuity of the tangential electric and magnetic field components across S :

$$\mathbf{E}^{inc}(\mathbf{r})|_{\tan} = (L_1 + L_2)\mathbf{J}(\mathbf{r})|_{\tan} - (K_1 + K_2)\mathbf{M}(\mathbf{r})|_{\tan}. \quad (1)$$

$$\mathbf{H}^{inc}(\mathbf{r})|_{\tan} = (K_1 + K_2)\mathbf{J}(\mathbf{r})|_{\tan} + \left(\frac{1}{\eta_1}L_1 + \frac{1}{\eta_2}L_2\right)\mathbf{M}(\mathbf{r})|_{\tan}. \quad (2)$$

where η_1 and η_2 are the wave impedance of regions 1 and 2, respectively, and operators L_p and K_p ($p=1,2$) are defined by

$$L_p \mathbf{X}(\mathbf{r}) = \int_S ds' [j\omega\mu_p \mathbf{X}(\mathbf{r}') + \frac{j}{\omega\epsilon_p} \nabla \nabla' \cdot \mathbf{X}(\mathbf{r}')] g_p(\mathbf{r}, \mathbf{r}'), \quad (3)$$

$$K_p \mathbf{X}(\mathbf{r}) = \int_S ds' \mathbf{X}(\mathbf{r}') \times \nabla g_p(\mathbf{r}, \mathbf{r}'), \quad (4)$$

where $g_p(\mathbf{r}, \mathbf{r}')$ is the scalar Green’s function

$$g_p(\mathbf{r}, \mathbf{r}') = \frac{e^{-jk_p|\mathbf{r}-\mathbf{r}'|}}{4\pi|\mathbf{r}-\mathbf{r}'|}. \quad (5)$$

The solution of the PMCHW (equations (1-4)) obtains the electric and magnetic surface current densities \mathbf{J} and \mathbf{M} , which are required in the computation of the bistatic scattering coefficient (normalized RCS) [23].

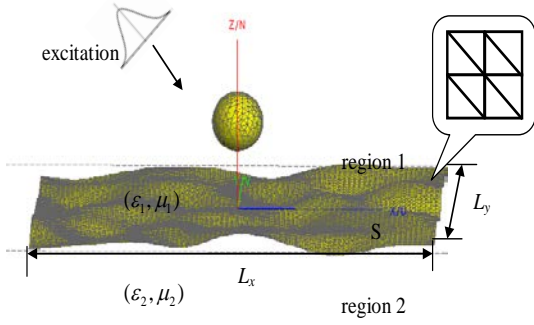


Fig. 1. Geometric model of EM scattering from the rough surface.

B. Higher order basis functions

In this paper, four types of higher order basis functions are used to analyze the electromagnetic scattering from the target and dielectric rough surface. For simplicity, the higher order hierarchical Legendre basis functions defined on the curvilinear quadrilateral surface are provided here. The specific forms of the hierarchical tangential vector basis functions on the curvilinear triangle patch [20, 35-36] and the maximally orthogonalized higher order basis functions on the curvilinear quadrilateral patch [21] can be found in the references.

The higher order hierarchical Legendre basis functions defined on the curvilinear quadrilateral surface [8-10] are

$$\mathbf{J}_S = J_S^u \mathbf{a}_u + J_S^v \mathbf{a}_v, \quad (6)$$

where \mathbf{a}_u and \mathbf{a}_v are the co-variant unitary vectors as $\mathbf{a}_u = \partial \mathbf{r} / \partial u$ and $\mathbf{a}_v = \partial \mathbf{r} / \partial v$. Without loss of generality, we consider only u-directed currents

$$J_S^u(u, v) = \frac{1}{\mathcal{J}_S(u, v)} \sum_{m=0}^{M^u} \sum_{n=0}^{N^v} a_{mn}^u \tilde{C}_m \tilde{P}_m(u) C_n P_n(v), \quad (7)$$

where $\mathcal{J}_S(u, v) = |\mathbf{a}_u \times \mathbf{a}_v|$ is the surface Jacobian, a_{mn}^u are unknown coefficients, and M^u and N^v are basis orders along the u-directed current flow direction and the transverse direction respectively. $P_n(v)$ are Legendre polynomials, and $\tilde{P}_m(u)$ are modified Legendre polynomials, which can be defined as

$$\tilde{P}_m(u) = \begin{cases} 1-u, & m=0 \\ 1+u, & m=1, \\ P_m(u) - P_{m-2}(u), & m \geq 2 \end{cases} \quad (8)$$

where \tilde{C}_m and C_n are the scaling factors

$$\tilde{C}_m = \begin{cases} \frac{\sqrt{3}}{4}, & m=0,1 \\ \frac{1}{2} \sqrt{\frac{(2m-3)(2m+1)}{2m-1}}, & m \geq 2 \end{cases} \quad (9)$$

$$C_n = \sqrt{n + \frac{1}{2}}. \quad (10)$$

C. Matrix vector product accelerated by the MLFMA

In the process of MLFMA, interactions between the elements are classified as near zone and far zone. The near-zone elements are calculated directly using the MoM, and the far-zone elements are calculated by using the MLFMA [24,32]. The Green's function in the FMM is

$$\frac{e^{-jk|\mathbf{r}+\mathbf{d}|}}{|\mathbf{r}+\mathbf{d}|} \approx -jk \sum_{l=0}^L (-1)^l (2l+1) j_l(kd) h_l^{(1)}(kr) P_l(\hat{\mathbf{d}} \cdot \hat{\mathbf{r}}), \quad (11)$$

where k is the wavenumber, j_l is a spherical Bessel function of the first kind, and P_l is a Legendre polynomial. \mathbf{r} and \mathbf{d} are two vectors with r and d being their amplitudes with $d < r$, and $\hat{\mathbf{r}}$ and $\hat{\mathbf{d}}$ being their unit vectors respectively. The number of modes L is usually chosen as $L = kd + \ln(\pi + kd)$. In the MLFMA, a matrix-vector product can be executed as follows: all basis functions in a group can be aggregated into an outgoing radiation pattern which is then translated to an incoming radiation pattern at the receiving group. The incoming radiation pattern is then disaggregated to the test functions. In order to accelerate the solving process, the FGMRES [25, 26] iterative solver is used.

III. NUMERICAL RESULTS

In this section several numerical results are presented for various models and basis functions, in which a Gaussian dielectric rough surface with the following Gaussian spectrum [27].

$$W(k_x, k_y) = \frac{l_x l_y h^2}{4\pi} e^{-\frac{l_x^2 k_x^2 + l_y^2 k_y^2}{4}}, \quad (12)$$

is used. Here, l_x and l_y are the correlation lengths in x – and y – directions respectively. h is the *rms* height of the rough surface.

The GMRES restart counts are set to 30 and the inner and outer restart counts of FGMRES are both 10. The stop precision for restarted GMRES is set to 1.E-3 and that for the inner and outer iteration in the FGMRES algorithm are 1.E-2 and 1.E-3 respectively. The method is implemented on a personal computer with Intel Dual-core CPU. The CPU and memory sizes are 2.99GHz and 3.24GB, respectively. In the numerical figures presented below, “0.5-t” denotes 0.5-order hierarchical tangential vector basis functions based on the curvilinear triangle mesh defined in [20]. “1.5-t” denotes 1.5-order hierarchical tangential vector basis functions based on the curvilinear triangle mesh defined in [20]. “1-q” denotes 1-order hierarchical Legendre basis functions based on curvilinear quadrilateral mesh, “2-q” denotes 2-order hierarchical Legendre basis functions based on the curvilinear quadrilateral mesh, and “2-m” denotes 2-order maximally orthogonalized higher order basis functions based on the curvilinear quadrilateral mesh. It should be noted that the expressions for 1-order maximally orthogonalized higher order basis functions are the same as those of 1-order hierarchical Legendre basis functions.

Firstly, the PMCHW computer code with different basis functions is compared with the shooting and bouncing rays method (SBR) [28]. The size of the rough surface is $16\lambda \times 16\lambda$, with $h = 0.04\lambda$ and $l_x = l_y = 0.5\lambda$, where λ is the free-space wavelength. The dielectric constant is set to $\epsilon_1 = 1, \epsilon_2 = 5.4 - j0.04$. The tapered wave is incident at the elevation angle $\theta_i = 30^\circ$ and the azimuth angle $\varphi_i = 0^\circ$, with tapering parameter $g = 5.0\lambda$. Figure 2 is the bistatic RCS for HH polarization of these methods, which shows a reasonably good agreement.

In the second example the efficiency of the proposed method with different basis functions is evaluated. The size of the rough surface is $6\lambda \times 6\lambda$, with $h = 0.08\lambda$ and $l_x = l_y = 1.5\lambda$. The dielectric constant is set to be $\epsilon_1 = 1, \epsilon_2 = 2.25$. The tapered wave is incident at the elevation angle

$\theta_i = -30^\circ$ and the azimuth angle $\varphi_i = 0^\circ$, with tapering parameter $g = 3.0\lambda$. The size of the finest level blocks is $0.5\lambda \times 0.5\lambda \times 0.5\lambda$. Figure 3 is the bistatic RCS of different basis functions for HH polarization, which shows a good agreement. Table 1 gives comparisons of memory and time consumption, where “1.5-t [35,36]” denotes 1.5-order hierarchical tangential vector basis functions based on the curvilinear triangle mesh defined in [35, 36]. It should be noted that the expressions for 0.5-order hierarchical vector basis functions defined in [35, 36] are the same as those for 0.5-order hierarchical basis functions defined in [20].

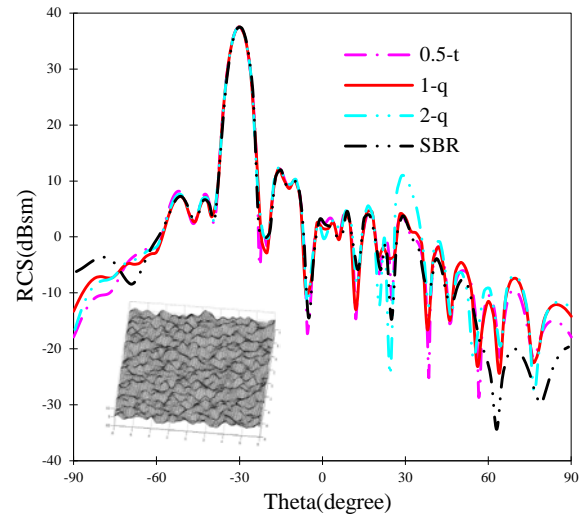


Fig. 2. Comparison of bistatic RCS of the dielectric rough surface for HH polarization.

The table shows that, the hierarchical Legendre basis functions based on the curvilinear quadrilateral mesh lead to a less total CPU time cost than the hierarchical tangential vector basis functions based on the curvilinear triangle mesh. For triangle cells, the basis functions defined in [35,36] lead to better condition numbers than the ones defined in [20], and results in less CPU time cost. Furthermore, the orthogonality of the maximally orthogonalized higher order basis functions enable fast convergence of the iteration, which results in a minimum requirement of total CPU time.

In the third example, we consider a perfectly electrical conducting (PEC) sphere buried under a rough surface published in [23]. The size of the rough surface is $8\lambda \times 8\lambda$, with $h = 0.02\lambda$ and

$l_x = l_y = 0.5\lambda$. The tapering parameter is $g = 2.0\lambda$. The dielectric constant is set to $\epsilon_1 = 1, \epsilon_2 = 2 - j0.2$. A sphere of radius $a = 0.3\lambda$ is buried under the rough surface at a depth of $d = 0.6\lambda$.

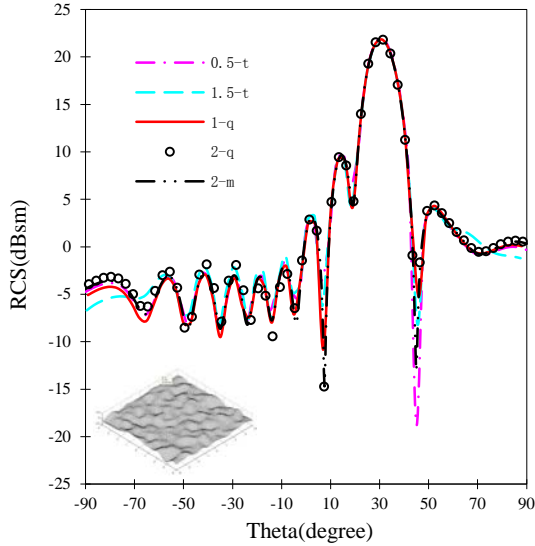


Fig. 3. Bistatic RCS of the dielectric rough surface for HH polarization.

Table 1: Cost comparison among different basis functions

Basis functions	Mesh size (λ)	Total unknowns	Near field filling time (sec.)
0.5-t	0.1	21,360	105
1.5-t	0.2	17,760	56
1.5-t-[35][36]	0.2	17,760	54
1-q	0.1	14,160	151
2-q	0.2	14,160	33
2-m	0.2	14,160	33

Basis functions	Iteration Number	Total time(sec.)	Memory cost(MB)
0.5-t	19	209	211
1.5-t	44	253	158
1.5-t-[35][36]	27	181	158
1-q	13	197	112
2-q	31	138	112
2-m	18	94	112

Figure 4 is the normalized RCS of different basis functions for HH polarization. The difference between the method presented in this paper and the references for some observation angles can be interpreted as that the rough surface used in this example is different from that in the references, which is a Gaussian stationary stochastic process. Table 2 gives comparisons of memory and time consumption. The table shows that the fill time of near field for “1.5-t” is smaller than that for “0.5-t”. However, due to the truncation of the dielectric rough surface, the interaction between the object and the rough surface, and the individual characteristics of the higher order basis functions, the condition numbers of the system become higher with the basis order increase. Consequently, the iteration time of the “1.5-t” is longer than that of “0.5-t”, which also applies to the Legendre basis functions. However, the maximally orthogonalized higher order basis functions, have a smaller iteration steps compared to “1.5-t” and “2-q”, which results in a minimum requirement of total CPU time.

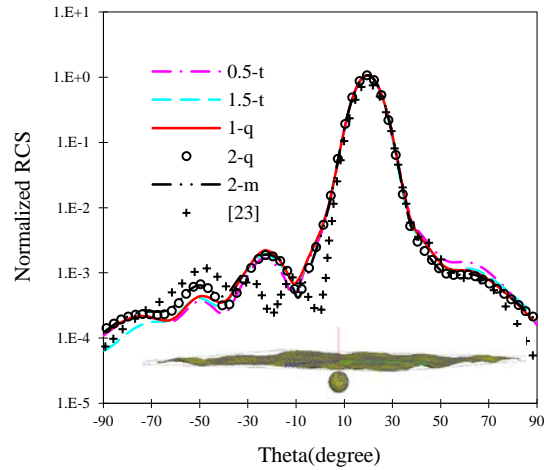


Fig. 4. Normalized RCS for a PEC sphere buried under a rough surface.

Finally, we consider a PEC sphere above a rough surface. The size of the rough surface is $8\lambda \times 8\lambda$, with $h = 0.02\lambda$ and $l_x = l_y = 0.5\lambda$. The tapering parameter is $g = 3.0\lambda$. The dielectric constant is set to $\epsilon_1 = 1, \epsilon_2 = 2 - j0.2$. A sphere of radius $a = 0.3\lambda$ is above the rough surface at a height of $d = 0.6\lambda$. Figure 5 is the bistatic RCS of different basis functions for HH polarization, and Table 3 gives comparisons on memory and time

consumption. Different from the third example, the CPU time cost of the three types basis functions decreases with the basis order increase, and the maximally orthogonalized higher order basis functions have a minimum requirement in total CPU time.

Table 2: Cost comparison among different basis functions

Basis functions	Mesh size (λ)	Total unknowns	Near field filling time (sec.)
0.5-t	0.1	38,404	276
1.5-t	0.2	32,000	110
1-q	0.1	25,592	298
2-q	0.2	25,472	64
2-m	0.2	25,472	64

Basis functions	Iteration number	Iteration time(sec.)	Total time(sec.)	Memory cost(MB)
0.5-t	17	188	487	393
1.5-t	57	506	631	296
1-q	12	88	493	211
2-q	87	577	663	210
2-m	18	124	210	210

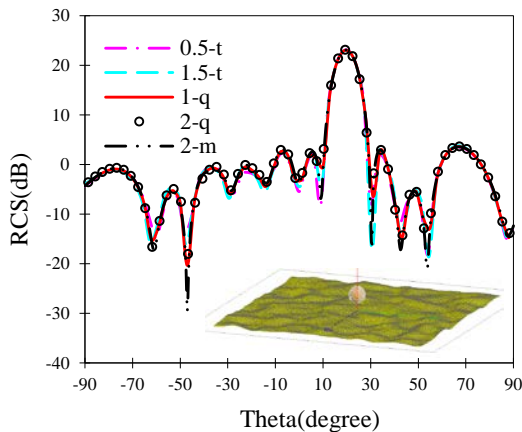


Fig. 5. Bistatic RCS for a PEC sphere above a rough surface.

Table 3: Cost comparison among different basis functions

Basis functions	Mesh size (λ)	Total unknowns	Near field filling time (sec.)
0.5-t	0.1	38,401	415
1.5-t	0.2	32,000	160
1-q	0.1	25,592	439
2-q	0.2	25,472	89
2-m	0.2	25,472	89

Basis functions	Iteration Number	Iteration time(sec.)	Total time(sec.)	Memory cost(MB)
0.5-t	16	191	606	559
1.5-t	47	437	597	415
1-q	11	74	513	292
2-q	28	178	267	289
2-m	15	98	187	289

IV. CONCLUSION

Numerical simulation of the combined target and rough surface model is complicated by the truncation of the dielectric rough surface and the interaction between the object and rough surface. In this paper, four types of higher order basis functions are used to analyze the EM scattering from the target and dielectric rough surface. Numerical simulation shows a reasonably good agreement with the SBR and references. For the target above the rough surface or only the rough surface case, the hierarchical Legendre basis functions based on the curvilinear quadrilateral mesh are more efficient than the hierarchical tangential vector basis functions based on the curvilinear triangle mesh in CPU time with the increase of the basis order. The maximally orthogonalized higher order basis functions show an excellent efficiency in dealing with all of the three cases.

ACKNOWLEDGMENT

The authors would like to thank the support of Major State Basic Research Development Program of China (973 Program: 2009CB320201), Natural Science Foundation of 61001009, and Jiangsu Natural Science Foundation of BK2008048.

REFERENCES

- [1] J. T. Johnson, "A Numerical Study of Scattering from an Object Above a Rough Surface," *IEEE Trans. Antennas Propag.*, vol. 50, no. 10, pp. 1361-1367, Oct. 2002.
- [2] M. El-Shenawee, C. Rappaport, E. L. Miller, and M. B. Silevitch, "Three-Dimensional Subsurface Analysis of Electromagnetic Scattering from Penetrable/PEC Objects Buried under Rough Surfaces: Use of the Steepest Descent Fast Multipole Method," *IEEE Trans. Geosci. Remote Sens.*, vol. 39, no. 6, pp. 1174-1182, June 2001.
- [3] H. Ye and Y.-Q. Jin, "A Hybrid Analytic-Numerical Algorithm of Scattering from an Object above a Rough Surface," *IEEE Trans. Geosci. Remote Sens.*, vol. 45, no. 5, pp. 1174-1180, May 2007.
- [4] F.-S. Deng, S.-Y. He, H.-T. Chen, W.-D. Hu, W.-X. Yu, and G.-Q. Zhu, "Numerical Simulation of Vector Wave Scattering from the Target and Rough Surface Composite Model with 3-D Multilevel UV Method," *IEEE Trans. Antennas Propag.*, vol. 58, no. 5, pp. 1625-1634, May 2010.
- [5] V. Jandhyala, B. Shanker, E. Michielssen, and W. C. Chew, "Fast Algorithm for the Analysis of Scattering by Dielectric Rough Surfaces," *J. Opt. Soc. Am. A*, vol. 15, no. 7, pp. 1877-1885, July 1998.
- [6] V. Jandhyala, E. Michielssen, S. Balasubramaniam, and W. C. Chew, "A Combined Steepest Descent-Fast Multipole Algorithm for the Fast Analysis of Three-Dimensional Scattering by Rough Surfaces," *IEEE Trans. Geosci. Remote Sens.*, vol. 36, no. 3, pp. 738-748, May 1998.
- [7] A. Yagbasan, C. A. Tunc, V. B. Ertürk, A. Altintas, and R. Mittra, "Characteristic Basis Function Method for Solving Electromagnetic Scattering Problems over Rough Terrain Profiles," *IEEE Trans. Antennas Propag.*, vol. 58, no. 5, pp. 1579-1589, May 2010.
- [8] C.-H. Kuo and M. Moghaddam, "Electromagnetic Scattering from a Buried Cylinder in Layered Media with Rough Interfaces," *IEEE Trans. Antennas Propag.*, vol. 54, no. 8, pp. 2392-2401, August 2006.
- [9] B. Liu, Z. Li, and Y. Du, "A Fast Numerical Method for Electromagnetic Scattering from Dielectric Rough Surfaces," *IEEE Trans. Antennas Propag.*, vol. 59, no. 1, pp. 180-188, January 2011.
- [10] A. Tabatabaenejad and M. Moghaddam, "Bistatic Scattering from Three-Dimensional Layered Rough Surfaces," *IEEE Trans. Geosci. Remote Sens.*, vol. 44, no. 8, pp. 2102-2114, 2006.
- [11] A. G. Voronovich, "Small-Slope Approximation for Electromagnetic Wave Scattering at a Rough Interface of Two Dielectric Half-Spaces," *Waves in Random Media*, vol. 4, iss. 3, pp. 337-367, 1994.
- [12] M. R. Pino, R. J. Burkholder, and F. Obelleiro, "Spectral Acceleration of the Generalized Forward-Backward Method," *IEEE Trans. Antennas Propag.*, vol. 50, no. 6, pp. 785-797, June 2002.
- [13] P. Liu and Y. Q. Jin, "Numerical Simulation of Bistatic Scattering from a Target at Low Altitude above Rough Sea Surface under an EM-Wave Incidence at Low Grazing Angle by Using the Finite Element Method," *IEEE Trans. Antennas Propag.*, vol. 52, no. 5, pp. 1205-1210, May 2004.
- [14] L. Kuang and Y. Q. Jin, "Bistatic Scattering from a Three-Dimensional Object over a Randomly Rough Surface using the FDTD Algorithm," *IEEE Trans. Antennas Propag.*, vol. 55, no. 8, pp. 2302-2312, August 2007.
- [15] J. T. Johnson, L. Tsang, R. T. Shin, K. Pak, C. H. Chan, A. Ishimaru, and Y. Kuga, "Backscattering Enhancement of Electromagnetic Waves from Two-Dimensional Perfectly Conducting Random Rough Surfaces—a Comparison of Monte Carlo Simulations with Experimental Data," *IEEE Trans. Antennas Propag.*, vol. 44, pp. 748-756, May 1996.
- [16] L. Tsang, J. A. Kang, F. H. Ding, and C. D. Ao, *Scattering of Electro Magnetic Wave; Numerical Simulation*, New York: Wiley, 2001.
- [17] E. Jørgensen, J. L. Volakis, P. Meincke, and O. Breinbjerg, "Higher Order Hierarchical Legendre Basis Functions for Electromagnetic Modeling," *IEEE Trans. Antennas Propag.*, vol. 52, no. 11, pp. 2985-2995, 2004.
- [18] E. Jørgensen, O. S. Kim, P. Meincke, and O. Breinbjerg, "Higher Order Hierarchical Discretization Scheme for Surface Integral Equations for Layered Media," *IEEE Trans. Geosci. Remote Sens.*, vol. 42, no. 4, pp. 346-352, 2004.
- [19] W. Yang, Z. Zhao, C. Qi, and Z. Nie, "Electromagnetic Modeling of Breaking Waves at Low Grazing Angles with Adaptive Higher Order Hierarchical Legendre Basis Functions," *IEEE Trans. Geosci. Remote Sens.*, vol. 49, no. 1, pp. 346-352, 2011.
- [20] L. S. Andersen and J. L. Volakis, "Hierarchical Tangential Vector Finite Elements for Tetrahedra," *IEEE Microwave and Guided Wave Letters*, vol. 8 no. 3 pp. 127-129, March 1998.
- [21] D. S. Sumic and B. M. Kolundzija, "Efficient Iterative Solution of Surface Integral Equation Based on Maximally Orthogonalized Higher

- Order Basis Functions,” *Proc. IEEE Antennas Propag. Society Int. Sym.*, session 116, 2005.
- [22] A. J. Poggio and E. K. Miller, *Integral Equation Solutions of Three-Dimensional Scattering Problems, Computer Techniques for Electromagnetics*, pp. 159-264, Pergamon Press, Oxford and New York, 1973.
- [23] G. Zhang and L. Tsang, “Angular Correlation Function and Scattering Coefficient of Electromagnetic Waves Scattered by a Buried Object under a Two-Dimensional Rough Surface,” *J. Opt. Soc. Am. A*, vol. 15, no. 12, pp. 2995-3002, Dec. 1998.
- [24] J. Song, C. C. Lu, and W. C. Chew, “Multilevel Fast Multipole Algorithm for Electromagnetic Scattering by Large Complex Objects,” *IEEE Trans. Antennas Propag.*, vol. 45, no. 10, pp. 1488-1493, Oct. 1997.
- [25] Y. Saad and M. H. Schultz, “GMRES: A Generalized Minimal Residual Algorithm for Solving Nonsymmetric Linear Systems,” *SIAM J. Sci. Statist. Comput.*, vol. 7, pp. 856-869, July 1986.
- [26] Y. Saad., “A Flexible Inner-Outer Preconditioned GMRES Algorithm,” *SIAM J. Sci. Statist. Comput.*, vol. 14, pp. 461-469, 1993.
- [27] K. Pak, L. Tsang, C. H. Chan, and J. T. Johnson, “Back Scattering Enhancement of Electromagnetic Waves from Two-Dimensional Perfectly Conducting Random Rough Surface Based on Monte Carlo Simulations,” *J. Opt. Soc. Amer. A, Opt. ImageSci.*, vol. 12, no. 11, pp. 2491-2499, Nov. 1995.
- [28] H. Ling, R. C. Chou, and S. W. Lee, “Shooting and Bouncing Rays: Calculating the RCS of an Arbitrarily Shaped Cavity,” *IEEE Trans. Antennas Propag.*, vol. 37, no. 2, pp. 194-205, Feb. 1989.
- [29] R. Araneo and S. Barmada, “Advanced Image Processing Techniques for the Discrimination of Buried Objects,” *Applied Computational Electromagnetics Society (ACES) Journal*, vol. 26, no. 5, pp. 437-446, May 2011.
- [30] J. Li, L. X. Guo, and H. Zeng, “FDTD Investigation on Electromagnetic Scattering from Two-Dimensional Layered Rough Surfaces,” *Applied Computational Electromagnetics Society (ACES) Journal*, vol. 25, no. 5, pp. 450-457, May 2010.
- [31] M. El-Shenawee and C. M. Rappaport, “Monte Carlo Simulations for Clutter Statistics in Minefields: AP-Mine-Like-Target Buried Near a Dielectric Object beneath 2-D Random Rough Ground Surfaces,” *IEEE Trans. Geosci. Remote Sens.*, vol. 40, no. 6, pp. 1416-1426, 2002.
- [32] Z. Jiang, Y. Xu, R. S. Chen, Z.H. Fan, and D. Z. Ding, “Efficient Matrix Filling of Multilevel Simply Sparse Method Via Multilevel Fast Multipole Algorithm,” *Radio Science*, 2011.
- [33] C.-H. Kuo and M. Moghaddam, “Scattering from Multilayer Rough Surfaces Based on the Extended Boundary Condition Method and Truncated Singular Value Decomposition,” *IEEE Trans. Antennas Propag.*, vol. 54, no. 10, pp. 2917-2929, Oct. 2006.
- [34] P. Ingelström, “A New Set of H (Curl)-Conforming Hierarchical Basis Functions for Tetrahedral Meshes,” *IEEE Transactions on Microwave Theory and Techniques*, vol. 54, no. 1, pp. 106-114, Jan. 2006.
- [35] R. D. Graglia, A. F. Peterson, and F. P. Andriulli, “Curl-Conforming Hierarchical Vector Bases for Triangles and Tetrahedral,” *IEEE Trans. Antennas Propag.*, vol. 59, no. 3, pp. 950-959, Mar. 2011.
- [36] L. P. Zha, Y. Q. Hu, and T. Su, “Efficient Surface Integral Equation using Hierarchical Vector Bases for Complex EM Scattering Problems,” *IEEE Trans. Antennas Propag.*, vol. 60, no. 2, pp. 952-957, Feb. 2012.
- [37] A. F. Peterson and R. D. Graglia, “Scale Factors and Matrix Conditioning Associated with Triangular-Cell Hierarchical Vector Basis Functions,” *IEEE Antennas and Wireless Propagation Letters*, vol. 9, pp. 40-43, 2010.
- [38] A. F. Peterson and R. D. Graglia, “Evaluation of Hierarchical Vector Basis Functions for Quadrilateral Cells,” *IEEE Trans. Magnetics*, vol. 47, pp. 1190-1193, May 2011.



Yuyuan An was born in Sichuan province, China, in 1986. He received the B.S. degree from Nanjing University of Science and Technology (NJUST) in 2009, and is currently working toward the Ph.D. degree at NJUST. His current research interests include

computational electromagnetics, antennas, electromagnetic scattering and propagation, and electromagnetic modeling of microwave integrated circuits.



Rushan Chen was born in Jiangsu, P. R. China. He received his B.Sc. and M.Sc. degrees from the Dept. of Radio Engineering, Southeast University, in 1987 and in 1990, respectively, and his Ph.D. from the Dept. of Electronic Engineering, City University of Hong Kong in

2001. He joined the Dept. of Electrical Engineering, Nanjing University of Science & Technology (NJUST), where he became a Teaching Assistant in 1990 and a

Lecturer in 1992. He has authored or co-authored more than 200 papers, including over 140 papers in international journals. He is the recipient of the Foundation for China Distinguished Young Investigators presented by the National Science Foundation (NSF) of China in 2003. In 2008, he became a Chang-Jiang Professor under the Cheung Kong Scholar Program awarded by the Ministry of Education, China. His research interests mainly include microwave/millimeter-wave systems, measurements, antenna, RF-integrated circuits, and computational electromagnetics.



Pingping Xu was born in Jiangsu province, China. She received the B.S. degree from Huaiyin Normal College in 2009, and is currently working toward the M.S. degree at NJUST. Her current research interests include computational electromagnetics, antennas, electromagnetic scattering and propagation, and electromagnetic modeling of microwave integrated circuits.



Zhiwei Liu was born in Nanchang, Jiangxi, China in 1982. He received B.S. degree in Computer Science from Nanjing University of Science and Technology in 2003, M.S. degree in Nanjing Institute of Electronics and Technology in 2006, and Ph.D. degree in Nanjing University of Science and Technology in 2011, respectively. He was with the Department of Electrical and Computer Engineering, Iowa State University, as a visiting scholar in 2009. He is currently working at School of Information Engineering, East China Jiaotong University. His research interests focus on the theory of electromagnetic scattering and inverse scattering.



Liping Zha was born in Anhui Province, China, in 1987. She received the B.S. degree in Electronic Information Engineering from Anhui University of Architecture, China, in 2008, and is currently working toward the Ph.D. degree at Nanjing University of Science and Technology (NJUST), Nanjing, China. Her current research interests include computational electromagnetics, electromagnetic modeling of scattering problems, wave scattering and propagation from random media, and numerical techniques for electrically large objects.

The Meshless Local Boundary Equation Method

B. Honarbakhsh¹ and A. Tavakoli^{1,2}

¹Department of Electrical Engineering

²Institute of Communications Technology and Applied Electromagnetics
Amirkabir University of Technology (Tehran Polytechnic), Tehran, IRAN
b_honarbaksh@aut.ac.ir, tavakoli@aut.ac.ir

Abstract — A method similar to the local boundary integral equation method that preserves its properties and is free from singular integrals is proposed. The approach is based on selection of the weighting functions from a homogeneous solution of the problem rather than the fundamental solution. Many examples of 2D Laplace and Helmholtz equations and 3D vector wave equation are presented for verification. The method shows optimistic performance over piecewise smooth boundaries. Radial basis functions of thin plate spline type are used for meshless discretization. The dependable performance of the proposed method provides a hopeful applicability to numerical solutions of partial differential equations.

Index Terms — Helmholtz, Laplace, meshless, vector wave equation.

I. INTRODUCTION

Recently, meshless methods have become an attractive research area for electrical engineers [1-19]. In its evolution, one can recognize three turning points. First, the development of the meshless local Petrov-Galerkin (MLPG) method that removes the entire-domain integration leading to computational efficiency [20]. Second, the development of the local boundary integral equation (LBIE) method that not only makes imposing the Dirichlet (essential) boundary condition (EBC) with a weak form of the problem possible, but also reduces the computational cost [21]. Third, the construction of the multi-dimensional interpolation functions (interpolants) with non-singular moment matrix that simplifies the imposition of essential boundary conditions (EBCs) [22].

Since the weighting function in the LBIE is constructed from the fundamental solution of the problem, singular integrands appear at the boundary nodes. Obviously, the order of the singularity of the aforementioned weighting function (companion solution) depends on the differential operator and the dimension of the problem. For example, the companion solution of a 2D Laplace equation is weak singular and is hyper-singular for a 3D vector wave equation. Consequently, numerical implementation of the LBIE is not as straightforward as other meshfree methods. Therefore, a method that has the same valuable properties of the LBIE but is free from singular integrands is desirable.

The main purpose of this paper is to suggest an approach that could circumvent the singular integrands. Our approach is based on selection of the weighting functions from a homogeneous solution of the problem, which is in general, a well-behaved function. Inspired by the well-known MLPG, we call this method meshless local boundary equation (MLBE). In MLPG, the local form of the Petrov-Galerkin statement of the problem is discretized by meshless shape functions. Similarly, in MLBE, the local form of the proposed boundary equation governing the problem is discretized by meshless shape functions.

We applied the method to a number of abstract examples including Laplace, Helmholtz and vector wave equations, all with piecewise smooth boundaries. We have also verified the two important capabilities of the meshfree methods, i.e., their robustness in dealing with irregular node arrangements and their flexibility in hybridization.

II. THE BOUNDARY EQUATION

Consider the following two-dimensional second-order boundary value problem (BVP):

$$\begin{cases} \nabla^2 u(\mathbf{x}) + k_0^2 u(\mathbf{x}) = p(\mathbf{x}), & \mathbf{x} \in \Omega \\ u = \bar{u}, & \mathbf{x} \in \Gamma_u \\ u_{,n} + \xi u = \bar{q}, & \mathbf{x} \in \Gamma_q \end{cases} \quad (1)$$

Where Ω is the problem domain and $\partial\Omega \equiv \Gamma = \Gamma_u \cup \Gamma_q$ is the problem boundary. With the above definition, four different problems can be formulated, which are named P1 through P4 as follows:

$$\begin{cases} k_0 = 0 \begin{cases} p = 0 & \text{(P1)} \\ p \neq 0 & \text{(P2)} \end{cases} \\ k_0 \neq 0 \begin{cases} p = 0, (\bar{u} \vee \bar{q}) \neq 0 \\ p \neq 0 \\ p = 0, (\bar{u} \wedge \bar{q}) = 0 & \text{(P4)} \end{cases} \end{cases} \quad \text{(P3)} \quad (2)$$

Where P1, P2 and P3 are Laplace, Poisson and Helmholtz equations respectively. P4 is a Helmholtz eigenvalue problem. Since the first three of the above are different in nature from the last, we will split this part to two sections and discuss each case separately.

A. Boundary equation for P1-P3

Following the method of weighted residuals [23], one can seek the solution of these cases by considering the following weighted integral:

$$\int_{\Omega} w(\nabla^2 u + k_0^2 u - p) d\Omega = 0. \quad (3)$$

Where w is the weighting function. Applying the scalar Green's theorem to (3) results in an equivalent weak formulation of the original problem:

$$\int_{\Omega} u(\nabla^2 w + k_0^2 w) d\Omega + \int_{\Gamma} (wu_{,n} - w_{,n}u) d\Gamma - \int_{\Omega} wp d\Omega = 0. \quad (4)$$

Imposing the boundary conditions leads to:

$$\begin{aligned} & \int_{\Omega} u(\nabla^2 w + k_0^2 w) d\Omega + \int_{\Gamma_u} wu_{,n} d\Gamma - \int_{\Gamma_q} (w\xi + w_{,n})u d\Gamma \\ & = \int_{\Omega} wp d\Omega + \int_{\Gamma_u} w_{,n}\bar{u} d\Gamma - \int_{\Gamma_q} \bar{w}q d\Gamma. \end{aligned} \quad (5)$$

By a proper choice of w , the domain (surface for 2D and volume for 3D problems) integral of the left hand side could be eliminated. Obviously, there exist at least two possibilities. First, w is the fundamental solution of the main problem. Here,

w is unique and will lead to the boundary integral equation (BIE) introduced in [21]:

$$\begin{aligned} u(\mathbf{y}) + \int_{\Gamma_u} wu_{,n} d\Gamma - \int_{\Gamma_q} (w\xi + w_{,n})u d\Gamma \\ = \int_{\Omega} wp d\Omega + \int_{\Gamma_u} w_{,n}\bar{u} d\Gamma - \int_{\Gamma_q} \bar{w}q d\Gamma. \end{aligned} \quad (6)$$

Second, w is a homogeneous solution of the main problem. Such a weight function is not unique and leads to our developed boundary equation (BE):

$$\begin{aligned} \int_{\Gamma_u} wu_{,n} d\Gamma - \int_{\Gamma_q} (w\xi + w_{,n})u d\Gamma \\ = \int_{\Omega} wp d\Omega + \int_{\Gamma_u} w_{,n}\bar{u} d\Gamma - \int_{\Gamma_q} \bar{w}q d\Gamma. \end{aligned} \quad (7)$$

Both methods have two important features. First, they make it possible to generate the coefficient (stiffness) matrix with (m-1)-dimensional integrals for m-dimensional problems. Second, the EBCs can be imposed by the weak statement directly. On the other hand, both methods suffer from one difficulty. In the BIE, the integrands of the boundary integrals are singular since w is made from the Green's function; and in the BE, it is not easy to find a proper homogeneous solution. The second and third integrals of the right hand side of (7) impose the boundary conditions. Being proper is assured only if:

$$\begin{cases} w \neq 0, & \mathbf{x} \in \Gamma_q \\ w_{,n} \neq 0, & \mathbf{x} \in \Gamma_u \end{cases} \quad (8)$$

Together, they put a sever restriction on choosing a homogeneous solution of the problem. Finding a proper homogeneous solution is an open problem. Of course, we have found one such solution for Laplace, Helmholtz and 3D vector wave equations, admitting that they may not be the best. We anticipate that the convergence rate and accuracy of the method could be improved by other solutions.

B. Boundary equation for P4

This is the most interesting case and is discussed in more detail. The mathematical description of the problem is:

$$\begin{cases} \nabla^2 u(\mathbf{x}) = -k_0^2 u(\mathbf{x}), & \mathbf{x} \in \Omega \\ u = 0, & \mathbf{x} \in \Gamma_u \\ u_{,n} + \xi u = 0, & \mathbf{x} \in \Gamma_q \end{cases} \quad (9)$$

With k_0 and u as unknowns. Based on [23], the BE solution of the above follows: first, multiply both sides of the Eigen-equation by a weighting function w and integrate over Ω :

$$\int_{\Omega} w \nabla^2 u d\Omega = -k_0^2 \int_{\Omega} w u d\Omega. \quad (10)$$

Second, construct the weak form of the left hand side of (10) and impose the boundary conditions. In BE, it is carried out by applying the scalar Green's theorem and leads to:

$$\int_{\Omega} u \nabla^2 w d\Omega + \int_{\Gamma_u} w u_{,n} d\Gamma - \int_{\Gamma_q} (w \xi + w_{,n}) u d\Gamma = -k_0^2 \int_{\Omega} w u d\Omega. \quad (11)$$

Third, choose w to be a proper homogeneous solution of the Laplace equations. This simplifies (11) to:

$$\int_{\Gamma_u} w u_{,n} d\Gamma - \int_{\Gamma_q} (w \xi + w_{,n}) u d\Gamma = -k_0^2 \int_{\Omega} w u d\Omega. \quad (12)$$

Fourth, discretize (12). This step *maps* the main continuous operator eigenvalue equation to a generalized matrix eigenvalue problem. Finally, solve the resulting generalized eigenvalue problem.

III. PROPER HOMOGENEOUS SOLUTIONS

A. Laplace/Poisson equation

In this case, the proper homogeneous solution corresponding to the i^{th} node should satisfy:

$$\begin{cases} \nabla^2 w_i(\mathbf{x}) = 0 \\ w_i(\mathbf{x}) \neq 0, \mathbf{x}_i \in \Gamma_q \\ w_{i,n}(\mathbf{x}) \neq 0, \mathbf{x}_i \in \Gamma_u \end{cases} \quad (13)$$

Therefore, one such solution is:

$$w_i(\mathbf{x} + \mathbf{x}_i) = 1 + (\alpha_i x + \beta_i y) + xy. \quad (14)$$

which is a linear combination of three harmonic functions and α_i and β_i are non-zero constant scalar.

The above solution is proper because:

$$\begin{cases} w_i(\mathbf{x}_i) = 1 \neq 0 \\ w_{i,x}(\mathbf{x}_i) = \alpha_i \neq 0 \\ w_{i,y}(\mathbf{x}_i) = \beta_i \neq 0 \end{cases} \quad (15)$$

Although for arbitrary shaped boundary, the first of (15) is sufficient for imposing the derivative boundary condition, imposition of Dirichlet type needs non-zero $w_{i,n}$. Suppose n_x and n_y be the Cartesian components of unit normal to

Γ . Noting that $w_{i,n} = \alpha_i n_x + \beta_i n_y$, for any curvature α_i and β_i can be selected such that $w_{i,n} \neq 0$.

B. Helmholtz equation

Similarly, the proper homogeneous solution corresponding to the i^{th} node should satisfy:

$$\begin{cases} \nabla^2 w_i(\mathbf{x}) + k_0^2 w_i(\mathbf{x}) = 0 \\ w_i(\mathbf{x}) \neq 0, \mathbf{x}_i \in \Gamma_q \\ w_{i,n}(\mathbf{x}) \neq 0, \mathbf{x}_i \in \Gamma_u \end{cases} \quad (16)$$

Thus, one proper solution is:

$$w_i(\mathbf{x} + \mathbf{x}_i) = \sin(\alpha_i x + \beta_i y + \pi/4). \quad (17)$$

Where $\alpha_i^2 + \beta_i^2 = k_0^2$. The above solution is proper because:

$$\begin{cases} w_i(\mathbf{x}_i) = \sin(\pi/4) \neq 0 \\ w_{i,x}(\mathbf{x}_i) = \alpha_i \cos(\pi/4) \neq 0 \\ w_{i,y}(\mathbf{x}_i) = \beta_i \cos(\pi/4) \neq 0 \end{cases} \quad (18)$$

For Cartesian problems both of Laplace and Helmholtz equations can be solved using the aforementioned scalars such that the most symmetric form of the weights results; i.e., $\alpha_i = \beta_i = 1$ for Laplace and $\alpha_i = \beta_i = k_0/\sqrt{2}$ for Helmholtz equation. To explain that a nonzero weigh function and its normal derivative at their local coordinate origin are sufficient, consider that satisfactory results are obtained by local domains with radii much smaller than the average nodal spacing [21]. Thus, the variations of the weight functions over the integration limits are tolerable. The validity of this argument is shown by examples in the paper.

IV. THE LOCAL BOUNDARY EQUATION

In this section, we apply (7), which is a global form to local domains of Ω and generate the local boundary equation (LBE) for P1 through P3. Generalization to P4 is straightforward. Based on the existence of an intersection between the boundaries of a local domain, $\partial\Omega_s$ with the global boundary of the problem Γ , two situations are distinguished (see Fig. 1):

A. Non-intersecting boundaries ($\partial\Omega_s \cap \Gamma = \emptyset$)

In this case, the local form becomes:

$$\int_{\partial\Omega_s} (wu_{,n} - w_{,n}u) d\Gamma = \int_{\Omega_s} wpd\Omega. \quad (19)$$

B. Intersecting boundaries ($\partial\Omega_s \cap \Gamma = \Gamma_s$)

The boundary of the local domain is decomposed into two parts, L_s is located completely in Ω without an intersection with Γ , and the other, Γ_s intersects Γ . Therefore, (7) becomes:

$$\begin{aligned} & \int_{L_s} (wu_{,n} - w_{,n}u) d\Gamma + \int_{\Gamma_s \cap \Gamma_u} wu_{,n} d\Gamma - \int_{\Gamma_s \cap \Gamma_q} (w\xi + w_{,n}) u d\Gamma \\ & = \int_{\Omega_s} wpd\Omega + \int_{\Gamma_s \cap \Gamma_u} w_{,n} \bar{u} d\Gamma - \int_{\Gamma_s \cap \Gamma_q} w \bar{q} d\Gamma. \end{aligned} \quad (20)$$

This completes the formulation of the LBE method. The remainder is discretization of the local form that maps either (19) or (20) to a system of linear equations. For this purpose, meshless shape functions are used.

V. SHAPE FUNCTION GENERATION

There exist two types of shape functions in meshless literature: approximants and interpolants. Approximants have a longer history than interpolants. Each one has its advantages and disadvantages. There are a number of strategies in generating each also [24]. Here, we have employed radial basis function (RBF) interpolants. Suppose the problem domain, Ω is described by N nodes. RBF shape functions interpolate the function u by a linear combination of N radial functions $\varphi_i, i = 1, \dots, N$, at any point of Ω . Thus:

$$u^h(\mathbf{x}) = \Phi^T(\mathbf{x}) \cdot \hat{\mathbf{u}} = \sum_{i=1}^N \varphi_i(\mathbf{x}) \hat{u}_i. \quad (21)$$

in which $\hat{\mathbf{u}} = [\hat{u}_1 \dots \hat{u}_N]^T$ and u^h is the RBF interpolation of u ; therefore, $u^h(\mathbf{x}_i) \equiv u_i = \hat{u}_i$. If the shape functions were approximants, then $u^h(\mathbf{x}_i) \equiv u_i \neq \hat{u}_i$. The coefficient vector $\hat{\mathbf{u}}$ is found by collocating (21) at the nodes. In this paper, φ_i is taken to be 9th and 5th order thin plate spline (TPS) function for 2D and 3D problems.

VI. MESHLESS DISCRETIZATION

For meshless discretization, the unknown function u in the final local form, i.e. (19) and (20) should be replaced by its equivalent expression, i.e. (21). Therefore:

$$\mathbf{K}\hat{\mathbf{u}} = \mathbf{f}. \quad (22)$$

with $\hat{\mathbf{u}}$ as unknowns, and entries of \mathbf{K} and \mathbf{f} are given by:

$$f_i = \begin{cases} \int_{\Omega_{si}} w_i p d\Omega, \partial\Omega_{si} \cap \Gamma = \emptyset \\ \int_{\Omega_{si}} w_i p d\Omega + \int_{\Gamma_{si} \cap \Gamma_u} w_{i,n} \bar{u} d\Gamma - \int_{\Gamma_{si} \cap \Gamma_q} w_i \bar{q} d\Gamma, \partial\Omega_{si} \cap \Gamma = \Gamma_{si} \end{cases}. \quad (23)$$

and:

$$K_{ij} = \begin{cases} \int_{\partial\Omega_{si}} (w_i \varphi_{j,n} - w_{i,n} \varphi_j) d\Gamma \\ , \partial\Omega_{si} \cap \Gamma = \emptyset \\ \int_{L_{si}} (w_i \varphi_{j,n} - w_{i,n} \varphi_j) d\Gamma + \int_{\Gamma_{si} \cap \Gamma_u} w \varphi_{j,n} d\Gamma \\ - \int_{\Gamma_{si} \cap \Gamma_q} (w \xi + w_{,n}) \varphi_j d\Gamma \\ , \partial\Omega_{si} \cap \Gamma = \Gamma_{si}. \end{cases} \quad (24)$$

Once $\hat{\mathbf{u}}$ is computed, the unknown function can be approximated/interpolated at any point of the problem domain.

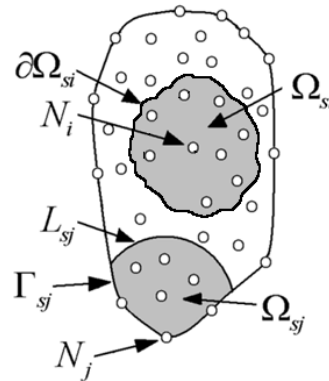


Fig. 1. Nodal geometry description of the problem and necessary definitions for meshless discretization. N_i : i^{th} node at \mathbf{x}_i , Ω_{si} : i^{th} local domain, $\partial\Omega_{si}$: i^{th} local boundary, L_{sj} : non-intersecting part of $\partial\Omega_{sj}$, Γ_{sj} : intersecting part of $\partial\Omega_{sj} = L_{sj} \cup \Gamma_{sj}$.

VII. VALIDATION PROCEDURE

Following the principal work of James Rautio [25], i.e., the convergence analysis, we designed a number of abstract problems. The MLBE is applied to each and the convergence of the solutions is investigated by convergence curves.

For error estimation, we use the relative error of energy defined as:

$$r_e = \|u - u_{exact}\| / \|u_{exact}\|. \quad (25)$$

$$\text{with } \|u\| = 1/2 \left(\int_{\Omega} |u|^2 d\Omega \right)^{1/2}.$$

VIII. 2D EXAMPLES

In this section, 2D Laplace and Helmholtz equations with various boundary conditions are solved. We have divided these examples into two types; elementary and advanced. Elementary examples are rectangular with a well-behaved boundary conditions and smooth solutions. On the other hand, advanced examples are non-rectangular or with a singular boundary condition or have a more complex solution. Nodal spacing is expressed by $h_x, h_y = x, y$, in corresponding directions with $h = (h_x^2 + h_y^2)^{1/2}$. Unless otherwise stated, the problem domains are described by regular node arrangements with equal spacing. In addition, for all problems α_i and β_i are selected as mentioned in part III. Local domains are assumed rectangular for internal nodes. For boundary nodes, they are rectangular for straight and circular for curved parts of the main boundary. In all cases, the largest sides of the rectangles are denoted by L and the radii by R . Finally, the number integration points for Gauss-Legendre quadrature is indicated by N_{GL} .

A. Elementary examples

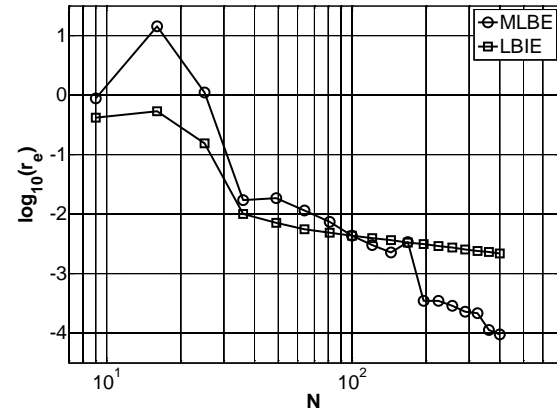
The domain of these examples is a 2×2 squares centered at the origin. The bottom, right, top, and left boundaries are named $\Gamma_1, \Gamma_2, \Gamma_3$ and Γ_4 , respectively. For all Laplace problems, the exact solution is selected to be [21]:

$$u_{exact}^{Laplace} = -x^3 - y^3 + 3x^2y + 3xy^2. \quad (26)$$

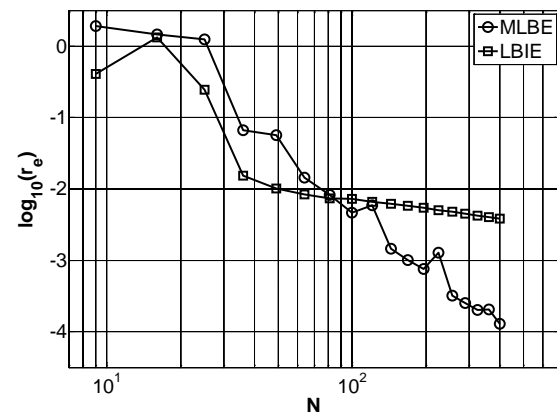
Similarly, for all Helmholtz problems:

$$u_{exact}^{Helmholtz} = \sin(2x)\sin(\sqrt{5}y). \quad (27)$$

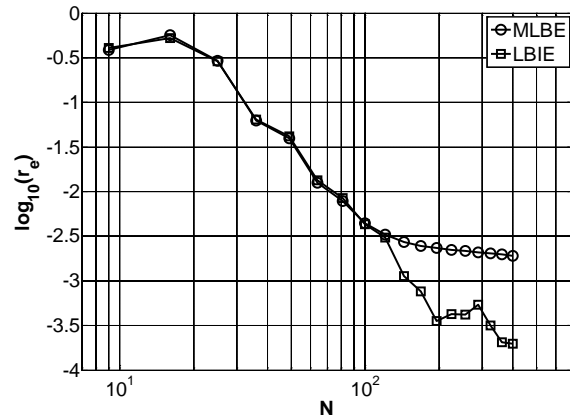
The details of these problems and the figures containing the corresponding convergence curves are listed in Table 1. For all these examples $L \leq 0.1h$ and $N_{GL} = 10$. To demonstrate that MLBE is an alternative to LBIE, all these examples are also solved by LBIE with the same discretization parameters.



(a)



(b)



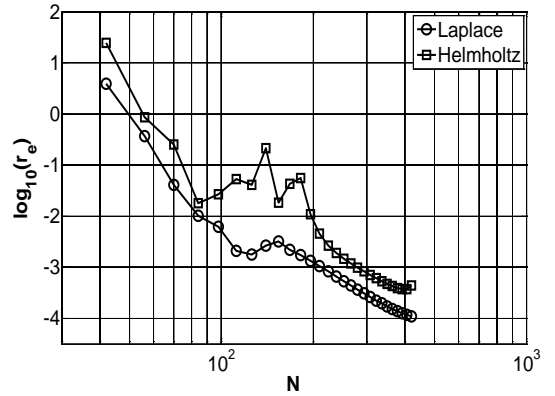
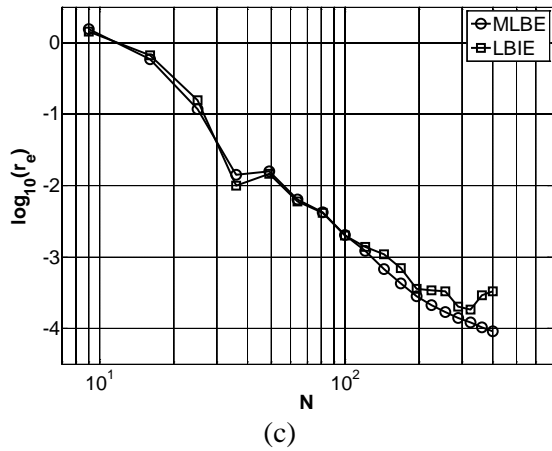
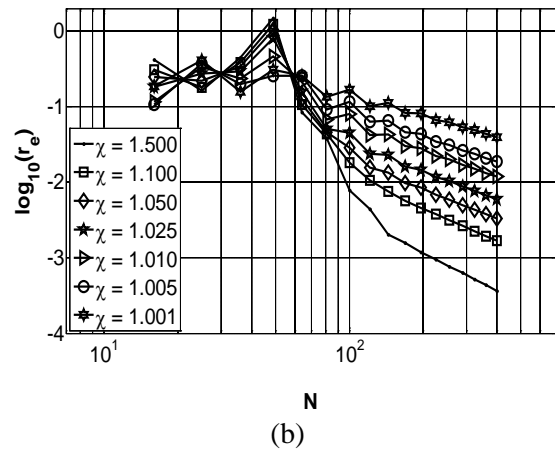
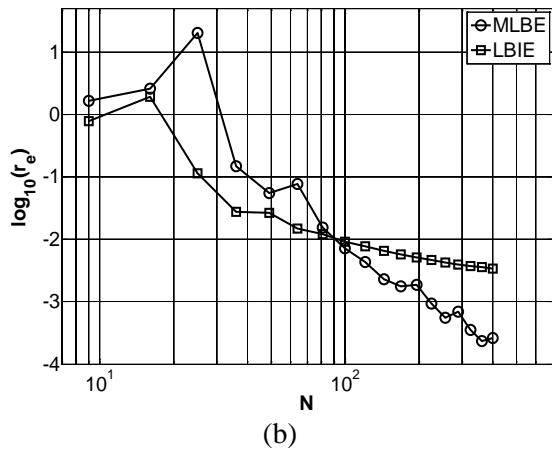
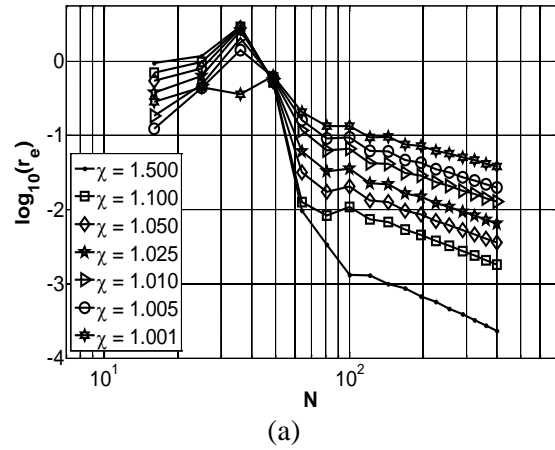
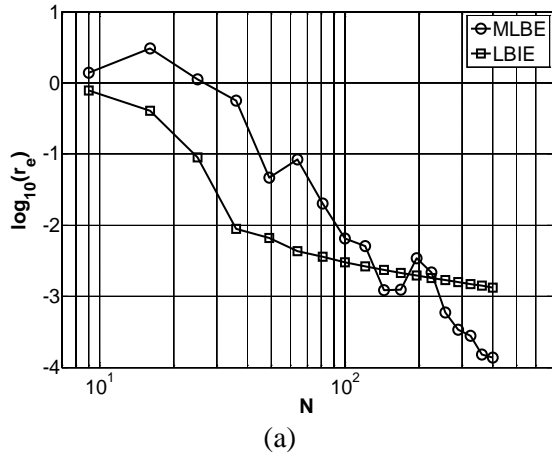


Fig. 3. Convergence of Helmholtz equation for (a) Dirichlet, (b) Dirichlet/Neumann and (c) Neumann boundary conditions.

Fig. 4. Convergence of the first advanced example for (a) Laplace and (b) Helmholtz equation.

Fig. 5. Convergence curves of the second advanced example.

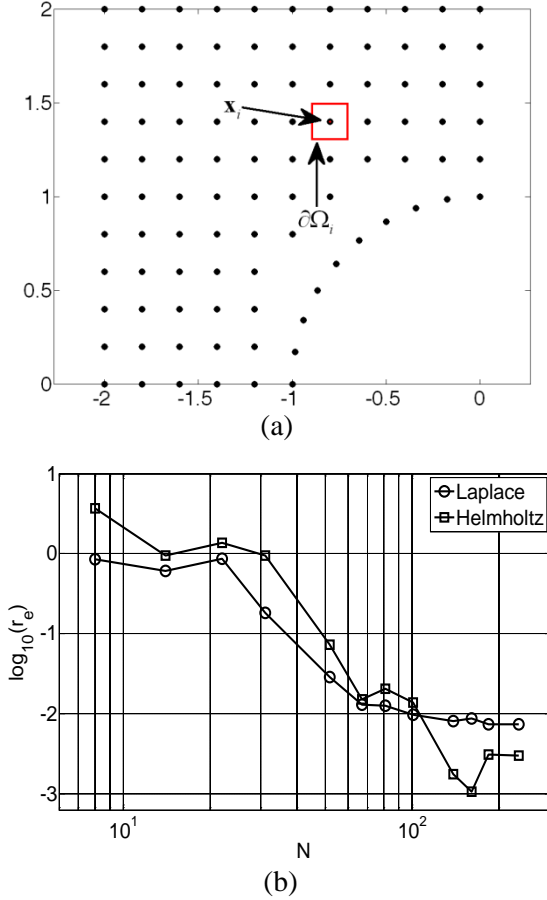


Fig. 6. (a) Nodal arrangement and the shape of a sample test domain and (b) convergence curves of the third advanced example.

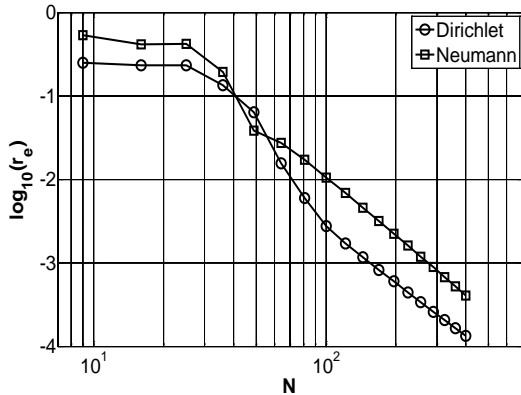


Fig. 7. Convergence of the sequence of the first nine eigenvalues for the last advanced example.

B. Advanced examples

The first of these examples has a domain similar to the elementary ones, but with singular Dirichlet boundary condition:

$$u(\mathbf{x}) = \left[(x^2 - \chi)(y^2 - \chi) \right]^{-1/2}, \mathbf{x} \in \partial\Omega. \quad (28)$$

where $\chi \in \{1.5, 1.1, 1.05, 1.025, 1.01, 1.005, 1.001\}$ and $k_0 = 3$ for Helmholtz equation. In this example, $L \leq 0.001h$ and $N_{GL} = 3$. Convergence curves corresponding to solutions of Laplace and Helmholtz equations by the MLBE method are depicted in Fig. 4.

The domain of our second advanced example is a circular disc with inner and outer radii equal to $r_{\min} = 0.1$ and $r_{\max} = 1$, respectively. The exact solution for Laplace and Helmholtz equations are selected to be:

$$u_{\text{exact}}^{\text{Laplace}} = r^3 \cos(3\theta). \quad (29)$$

and

$$u_{\text{exact}}^{\text{Helmholtz}} = J_3(3r) \cos(3\theta). \quad (30)$$

Table 1: Mathematical statement of the elementary examples and address of the related convergence curves

Boundary conditions	Equation	
	Laplace	Helmholtz
$u(\Gamma_i) = \bar{u}_i, i = 1, 2, 3, 4$	Fig. 2(a)	Fig. 3(a)
$\begin{cases} u(\Gamma_i) = \bar{u}_i, i = 1, 3 \\ u_{,n}(\Gamma_i) = \bar{q}_i, i = 2, 4 \end{cases}$	Fig. 2(b)	Fig. 3(b)
$u_{,n}(\Gamma_i) = \bar{q}_i, i = 1, 2, 3, 4$	Fig. 2(c)	Fig. 3(c)

In addition, the boundary condition is selected to be Dirichlet. This example has two important features. First, its geometry is not Cartesian. Second, since its boundary condition is all Dirichlet, it can validate the theoretical statements of the third section, i.e. the method is capable of imposing the essential boundary conditions on a curved boundary. Nodal arrangement for this example is polar with fixed 10 angular samples and radial samples increase from 3 to 20. For local domains, $L = 0.001h$ and $R = 0.001h$ are selected with $N_{GL} = 10$. Note that, although the spacing of nodes increases with radial distance, the size of local domains is fixed. In general, one can choose these sizes with respect to distance of each node from its neighbors. Since at any boundary node, either $\sin(\theta_i) \neq 0$ or $\cos(\theta_i) \neq 0$, imposition of the Dirichlet boundary condition at each node i on the boundary is guaranteed by:

$$\begin{cases} \sin(\theta_i) = 0 \Rightarrow \alpha_i = \cos(\theta_i)^{-1}, \beta_i = 0 \\ \cos(\theta_i) = 0 \Rightarrow \alpha_i = 0, \beta_i = \sin(\theta_i)^{-1} \\ \sin(2\theta_i) \neq 0 \Rightarrow \alpha_i = 2^{-1} \cos(\theta_i)^{-1}, \beta_i = 2^{-1} \sin(\theta_i)^{-1} \end{cases} \quad (31)$$

for Laplace, and:

$$\begin{cases} \sin(\theta_i) = 0 \Rightarrow \begin{cases} \alpha_i = 2^{1/2} \cos(\theta_i)^{-1} \\ \beta_i = (k_0^2 - \alpha_i^2)^{1/2} \end{cases} \\ \cos(\theta_i) = 0 \Rightarrow \begin{cases} \alpha_i = (k_0^2 - \beta_i^2)^{1/2} \\ \beta_i = 2^{1/2} \sin(\theta_i)^{-1} \end{cases} \\ \sin(2\theta_i) \neq 0 \Rightarrow \begin{cases} \alpha_i = 2^{1/2} \cos(\theta_i) + (k_0^2 - 2)^{1/2} \sin(\theta_i) \\ \beta_i = 2^{1/2} \sin(\theta_i) - (k_0^2 - 2)^{1/2} \cos(\theta_i) \end{cases} \end{cases} \quad (32)$$

for the Helmholtz equation. It is straightforward to see that such selections correspond to $w_{i,n}(\mathbf{x}_i) = 1 \neq 0$. One important point remains to be mentioned. In contrast to mesh/grid based methods that approximate curved boundaries with piecewise linear functions, in meshfree methods, it is possible to either move exactly on the boundary or to interpolate/approximate their curvature with proper shape functions [24]. In this example, the first choice was possible and is applied. Convergence curves are depicted in Fig. 5.

The third advanced example is devoted to a domain with irregular boundary. The nodal description of its geometry for a sample pass is shown in Fig. 6(a). Evidently, both the geometry and the nodal arrangement are irregular. The exact solution for Laplace and Helmholtz equations are selected the same as the elementary examples with the following mixed boundary conditions:

$$\begin{cases} \text{Neumann, } x = 0 \\ \text{Dirichlet, otherwise} \end{cases} \quad (33)$$

Solution parameters are the same as the previous example except the number of quadrature points is reduced to 3. Convergence curves are depicted in Fig. 6(b). As a final 2D example, the Helmholtz eigenvalue problem is solved over a square domain of unit side length. The convergence analysis is based on the sequence of the first nine eigenvalues. The corresponding convergence curves for all-Neumann and all-Dirichlet homogeneous boundary conditions are depicted in Fig. 7. For this problem $L \leq 0.4h$ and $N_{GL} = 10$.

IX. APPLICATION TO 3D VECTOR WAVE EQUATION

In this section, we extend the use of the MLBE method to a highly complicated equation; e.g., the 3D vector wave equation:

$$\begin{cases} \nabla \times \nabla \times \mathbf{U}(\mathbf{r}) - k_0^2 \mathbf{U}(\mathbf{r}) = 0, \mathbf{r} \in V \\ \mathbf{n} \times \mathbf{U}(\mathbf{r}) = \bar{\mathbf{U}}, \mathbf{r} \in S_U \\ \mathbf{n} \times \nabla \times \mathbf{U}(\mathbf{r}) = \bar{\mathbf{Q}}, \mathbf{r} \in S_Q \end{cases} \quad (34)$$

where V is the volume bounded by $S = S_U \cup S_Q$ and \mathbf{n} the unit normal to S [23]. Suppose the vector function \mathbf{w} is a proper homogeneous solution of the vector wave equation. Following the vectorial equivalent steps of Section II,

$$\begin{aligned} & \int_{S_U} (\mathbf{w} \times \mathbf{n}) \cdot (\nabla \times \mathbf{U}) dS + \int_{S_Q} (\mathbf{n} \times \mathbf{U}) \cdot (\nabla \times \mathbf{w}) dS \\ &= - \int_{S_U} \bar{\mathbf{U}} \cdot (\nabla \times \mathbf{w}) dS - \int_{S_Q} \mathbf{w} \cdot \bar{\mathbf{Q}} dS + \int_V \mathbf{w} \cdot \mathbf{P} dV. \end{aligned} \quad (35)$$

The next step is finding a proper \mathbf{w} , which for the i th node should satisfy:

$$\begin{cases} \nabla \times \nabla \times \mathbf{w}_i(\mathbf{r}) - k_0^2 \mathbf{w}_i(\mathbf{r}) = 0 \\ \mathbf{w}_i(\mathbf{r}) \neq 0, \mathbf{r}_i \in S_Q \\ \nabla \times \mathbf{w}_i(\mathbf{r}) \neq 0, \mathbf{r}_i \in S_U \end{cases} \quad (36)$$

Since (34) is a vector equation, we need three linearly independent proper vector weights. Making use of electromagnetic potentials, it is straightforward to show that for the i th node, the following is a set of proper homogeneous solutions:

$$\begin{cases} \mathbf{w}_{i1}(\mathbf{x} + \mathbf{x}_i) = \sin(\alpha_{i1}x + \beta_{i1}y + \gamma_{i1}z + \pi/4) \\ \quad \times (\alpha_{i1}^2 - k_0^2, \alpha_{i1}\beta_{i1}, \alpha_{i1}\gamma_{i1}) \\ \mathbf{w}_{i2}(\mathbf{x} + \mathbf{x}_i) = \sin(\alpha_{i2}x + \beta_{i2}y + \gamma_{i2}z + \pi/4) \\ \quad \times (\alpha_{i2}\beta_{i2}, \beta_{i2}^2 - k_0^2, \beta_{i2}\gamma_{i2}) \\ \mathbf{w}_{i3}(\mathbf{x} + \mathbf{x}_i) = \sin(\alpha_{i3}x + \beta_{i3}y + \gamma_{i3}z + \pi/4) \\ \quad \times (\alpha_{i3}\gamma_{i3}, \beta_{i3}\gamma_{i3}, \gamma_{i3}^2 - k_0^2) \\ \alpha_{ij}^2 + \beta_{ij}^2 + \gamma_{ij}^2 = k_0^2, j = 1, 2, 3 \end{cases} \quad (37)$$

where α_{ij} , β_{ij} and γ_{ij} are non-zero constant scalars, provided that they are selected such that linear independency is assured. The reason for introducing the aforementioned parameters is similar to statements of Section III. Now, consider three scenarios of Cartesian coordinate problems. The most symmetric selection is linear dependent and makes the coefficient matrix unsolvable. One choice that leads to satisfactory results is:

$$\begin{cases} \alpha_{i1} = -k_0/\sqrt{3}, \beta_{i1} = k_0/\sqrt{3}, \gamma_{i1} = k_0/\sqrt{3} \\ \alpha_{i2} = k_0/\sqrt{3}, \beta_{i2} = -k_0/\sqrt{3}, \gamma_{i2} = k_0/\sqrt{3} \\ \alpha_{i3} = k_0/\sqrt{3}, \beta_{i3} = k_0/\sqrt{3}, \gamma_{i3} = -k_0/\sqrt{3} \end{cases} \quad (38)$$

There exists another choice that can be regarded as a trivial solution:

$$\begin{cases} \alpha_{i1} = 0, \beta_{i1} = k_0/\sqrt{2}, \gamma_{i1} = k_0/\sqrt{2} \\ \alpha_{i2} = k_0/\sqrt{2}, \beta_{i2} = 0, \gamma_{i2} = k_0/\sqrt{2} \\ \alpha_{i3} = k_0/\sqrt{2}, \beta_{i3} = k_0/\sqrt{2}, \gamma_{i3} = 0 \end{cases} \quad (39)$$

Although this set of functions is linear independent, it is not reliable. A comparison between the weighting functions sets (38) and (39) will be made in what follows. To numerically verify the validity of the aforementioned analytical expressions, we first apply it to a rectangular block of $1.0\lambda_0 \times 1.0\lambda_0 \times 0.1\lambda_0$, $-l \leq x, y \leq l, 0 \leq z \leq t$ and singular Dirichlet boundary condition. The exact solution is selected to be:

$$\begin{aligned} \mathbf{U}_I = & \hat{\mathbf{x}} \sin[k_0(y+z)/\sqrt{2} + \pi/4] \\ & + \hat{\mathbf{y}} \sin[k_0(x+z)/\sqrt{2} + \pi/4] \\ & + \hat{\mathbf{z}} \sin[k_0(x+y)/\sqrt{2} + \pi/4], \mathbf{r} \in \Omega. \end{aligned} \quad (40)$$

subject to:

$$\begin{aligned} \mathbf{U}_B = & \hat{\mathbf{x}} \sin[k_0(y+z)/\sqrt{2} + \pi/4] \\ & + \hat{\mathbf{y}} \sin[k_0(x+z)/\sqrt{2} + \pi/4] \\ & + \hat{\mathbf{z}} \frac{\sin[k_0(x+y)/\sqrt{2} + \pi/4]}{\sqrt{|x^2 - (\chi l)^2| + |y^2 - (\chi l)^2| + |z - (\chi t)|^2}}, \mathbf{r} \in \partial\Omega \end{aligned} \quad (41)$$

where $\chi \in \{1.5, 1.1, 1.05, 1.025, 1.01, 1.005, 1.001\}$. For this problem, we have hybridized the MLBE and the meshfree collocation methods [26]. The later is applied to all boundaries except the top one and the former to other nodes. This is simply done by switching to Dirac delta as weight function for the nodes to be solved by the collocation method. In harmony with the problem domain, the local domains for internal and top-boundary nodes are selected to be $L_x \times L_y \times L_z$ rectangular blocks with $L_x \leq 0.3h$, $L_y \leq 0.3h$ and $L_z \leq 0.03h$ where $h = (h_x^2 + h_y^2 + h_z^2)^{1/2}$. For numerical integration over each surface, $N_{GL} = 9$ is used. Since the rest of the nodes are solved by the collocation method, the concept of local domain is inapplicable. Equation

set (38) is used as weight function. The convergence of the electric field is depicted in Fig. 8(a). For comparison, this example is also solved by equation set (39) with $\chi = 0.001$ as depicted in Fig. 8(b). Definitely, solution parameters are the same.

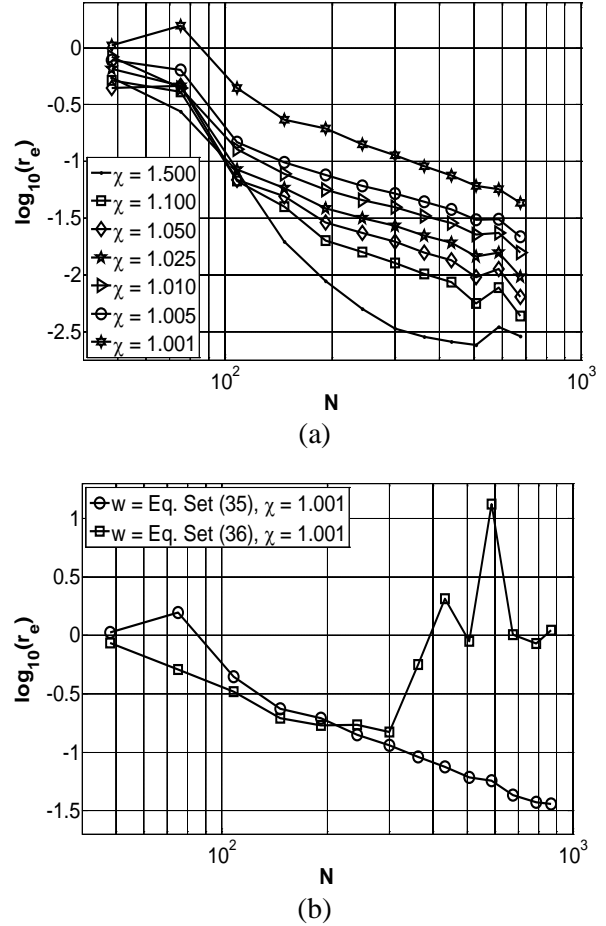


Fig. 8. Convergence of the problem corresponding to 3D vector wave equation over a rectangular block by (a) equation set (35) and (b) equation set (35) and (36) as weighting.

X. CONCLUSION

It is shown that the MLBE method is a good candidate for the numerical solution of PDEs. Comparison with the LBIE method also shows better convergence in the limit. The main advantage of the MLBE method over the LBIE method is the absence of singular integrands.

ACKNOWLEDGMENT

The authors appreciate Prof. M. Dehghan for inputs in meshfree methods, and Prof. R. F. Dana, for inputs regarding validation techniques.

REFERENCES

- [1] Y. Marechal, "Some Meshless Methods for Electromagnetic Field Computations," *IEEE Trans. Magn.*, vol. 34, no. 5, pp. 3351-3354, 1998.
- [2] C. Herault and Y. Marechal, "Boundary and Interface Conditions in Meshless Methods," *IEEE Trans. Magn.*, vol. 35, no. 3, pp. 1450-1453, 1999.
- [3] S. L. Ho, S. Yang, J. M. Machado, and H. C. Wong, "Application of a Meshless Method in Electromagnetics," *IEEE Trans. Magn.*, vol. 37, no. 5, pp. 3198-3201, 2001.
- [4] L. Xuan, Z. Zeng, B. Shanker, and L. Udpa, "Meshless Method for Numerical Modeling of Pulsed Eddy Currents," *IEEE Trans. Magn.*, vol. 40, no. 6, pp. 3457-3462, 2004.
- [5] S. L. Ho, S. S. Yang, H. C. Wong, and G. Ni, "Meshless Collocation Method Based on Radial Basis Functions and Wavelets," *IEEE Trans. Magn.*, vol. 40, no. 2, pp. 1021-1024, 2004.
- [6] S. L. Ho, S. S. Yang, G. Ni, H. C. Wong, and Y. Wang, "Numerical Analysis of Thin Skin Depths of 3-D Eddy-Current Problems using a Combination of Finite Element and Meshless Methods," *IEEE Trans. Magn.*, vol. 40, no. 2, pp. 1354-1357, 2004.
- [7] S. L. Ho, S. S. Yang, H. C. Wong, E. W. C. Lo and G. Ni, "Refinement Computations of Electromagnetic Fields using FE and Meshless Methods," *IEEE Trans. Magn.*, vol. 41, no. 5, pp. 1456-1459, 2005.
- [8] Y. Zhang, K. R. Shao, D. X. Xie and J. D. Lavers, "Meshless Method Based on Orthogonal Basis for Electromagnetics," *IEEE Trans. Magn.*, vol. 41, no. 5, pp. 1432-1435, 2005.
- [9] Q. Li and K. Lee, "Adaptive Meshless Method for Magnetic Field Computation," *IEEE Trans. Magn.*, vol. 42, no. 8, pp. 1996-2003, 2006.
- [10] R. K. Gordon and W. E. Hutchcraft, "The Use of Multiquadric Radial Basis Functions in Open Region Problems," *Applied Computational Electromagnetics Society (ACES) Journal*, vol. 21, no. 2, pp. 127-134, July 2006.
- [11] Y. Zhang, K. R. Shao, J. Zhu, D. X. Xie, and J. D. Lavers, "A Comparison of Point Interpolative Boundary Meshless Method Based on PBF and RBF for Transient Eddy-Current Analysis," *IEEE Trans. Magn.*, vol. 43, no. 4, pp. 1497-1500, 2007.
- [12] F. G. Guimaraes, R. R. Saldanha, R. C. Mesquita, D. A. Lowther, and J. A. Ramirez, "A Meshless Method for Electromagnetic Field Computation Based on the Multiquadratic Technique," *IEEE Trans. Magn.*, vol. 43, no. 4, pp. 1281-1284, 2007.
- [13] S. Ikuno, K. Takakura, and A. Kamitani, "Influence of Method for Imposing Essential Boundary Condition on Meshless Galerkin/Petrov-Galerkin Approaches," *IEEE Trans. Magn.*, vol. 43, no. 4, pp. 1501-1504, 2007.
- [14] S. McFee, D. Ma, and M. Golshayan, "A Parallel Meshless Formulation for H-P Adaptive Finite Element Analysis," *IEEE Trans. Magn.*, vol. 44, no. 6, pp. 786-789, 2008.
- [15] T. Kaufmann, C. Fumeaux, and R. Vahldieck, "The Meshless Radial Point Interpolation Method for Time-Domain Electromagnetics," *IEEE MTT-S Int. Microwave Symp. Dig.*, Atlanta, pp. 61-64, 2008.
- [16] Y. Yu and Z. Chen, "A 3-D Radial Point Interpolation Method for Meshless Time-Domain Modeling," *IEEE Trans. Microwave Theory Tech.*, vol. 57, no. 8, pp. 2015-202, 2009.
- [17] Y. Yu and Z. Chen, "Towards the Development of an Unconditionally Stable Time-Domain Meshless Method," *IEEE Trans. Microwave Theory Tech.*, vol. 58, no. 3, pp. 578-586, 2010.
- [18] T. Kaufmann, C. Engström, C. Fumeaux, and R. Vahldieck, "Eigenvalue Analysis and Longtime Stability of Resonant Structures for the Meshless Radial Point Interpolation Method in Time Domain," *IEEE Trans. Microwave Theory Tech.*, vol. 58, no. 12, pp. 3399-3408, 2010.
- [19] R. D. Soares, R. C. Mesquita, F. J. S. Moreira, "Axisymmetric Electromagnetic Resonant Cavity Solution by a Meshless Local Petrov-Galerkin Method," *Applied Computational Electromagnetics Society (ACES) Journal*, vol. 26, no. 10, pp. 792-799, October 2011.
- [20] S. N. Atluri and T. A. Zhu, "A New Meshless Local Petrov-Galerkin (MLPG) Approach in Computational Mechanics," *CMES*, vol. 22, pp. 117-127, 1998.
- [21] T. Zhu, J.-D. Zhang, and S. N. Atluri, "A Local Boundary Integral Equation (LBIE) Method in Computational Mechanics, and a Meshless Discretization Approach," *CMES*, vol. 3, no.1, pp. 223-235, 1998.
- [22] J. G. Wang and G. R. Liu, "Radial Point Interpolation Method for Elastoplastic Problems," presented at 1st *Int. Conf. Structural Stability and Dynamics*, Taipei, Taiwan, 2000.
- [23] J. Jin, *The Finite Element Method in Electromagnetics*, Second Edition. John Wiley & Sons, 2002.
- [24] G. R. Liu, *Mesh Free Methods*, CRC Press, 2003.
- [25] J. C. Rautio, "The Microwave Point of View on Software Validation," *IEEE Antennas Propagat. Mag.*, vol. 38, no. 2, pp. 68-71, 1996.

- [26] G. R. Liu and Y. T. Gu, *An Introduction to MeshFree Methods and Their Programming*, Springer, 2005.



Babak Honarbakhsh was born in Tehran, Iran. He received his B.S. and M.S. degrees in Electrical Engineering from Amirkabir University of Technology where he is currently working toward his Ph.D. degree. His current research interest is numerical solution of electromagnetic problems by meshfree methods.



Ahad Tavakoli was born in Tehran, Iran on March 8, 1959. He received the B.S. and M.S. degrees from the University of Kansas, Lawrence, and the Ph.D. degree from the University of Michigan, Ann Arbor, all in Electrical Engineering, in 1982, 1984, and 1991, respectively.

In 1991, he joined the Amirkabir University of Technology, Tehran, Iran where he is currently a Professor in the Department of Electrical Engineering. His research interests include EMC, scattering of electromagnetic waves and microstrip antennas.

PEC Condition Implementation for the Novel Weakly Conditionally Stable Finite-Difference Time-Domain Method

Juan Chen, Jianguo Wang, and Chunming Tian

School of Electronic and Information Engineering, Xi'an Jiaotong University, Xi'an 710049, China
tianchm@mail.xjtu.edu.cn

Abstract — The perfect-electric-conductor (PEC) condition implementation for the novel weakly conditionally stable finite-difference time-domain (NWCS-FDTD) method is discussed in this paper. It shows that the method that the PEC condition is directly incorporated within the tri-diagonal matrix is more accurate and the burden on the computation efficiency is trivial. The theory proposed in this article is validated through numerical example.

Index Terms — FDTD method, perfect-electric-conductor (PEC) condition, weakly conditionally stable FDTD method.

I. INTRODUCTION

To overcome the Courant limit on the time step size of the FDTD method, unconditionally stable methods such as the alternating-direction implicit FDTD (ADI-FDTD) scheme [1-6] have been studied extensively. Although the time step size in the ADI-FDTD simulation is no longer bounded by the Courant–Friedrich–Levy (CFL) criterion, the method exhibits a splitting error [7, 8] that is proportional to the square of the time step size and the spatial derivatives of the field. When field variation and/or the time step size are large, the splitting error becomes pronounced. The accuracy of the ADI-FDTD method is limited.

Based on the theory of the ADI-FDTD method, a novel weakly conditionally stable finite-difference time-domain (NWCS-FDTD) method has been developed recently [9]. In this method, the CFL condition is not removed totally, but being weaker than that of the conventional FDTD method. The time step in this scheme is only

determined by one discretization, which is extremely useful for a problem where a very fine mesh is needed in one or two directions. Compared with the ADI-FDTD scheme, the NWCS-FDTD method is with trivial split error, so the accuracy of the NWCS-FDTD technique is better than that of the ADI-FDTD scheme. By defining the field components at only two time steps, the NWCS-FDTD method requires the solution of four tri-diagonal matrices and four explicit updates at each time step. While maintaining the same time step size, the CPU time for the NWCS-FDTD method can be reduced to about 2/3 of that for the ADI-FDTD scheme.

Compared with the conventional weakly conditionally stable finite-difference time-domain (WCS-FDTD) method [10, 11], the NWCS-FDTD method has less split error, so the accuracy of the NWCS-FDTD method is also better than that of the conventional WCS-FDTD method. The detailed comparison between these two methods has been presented in reference [12].

In the NWCS-FDTD method, updating of H_y component needs the unknown E_x and E_z components at the same time step, thus, the perfect-electric-conductor condition implementation for the E_x and E_z components must be incorporated within the solving of the H_y component. This paper gives a simple strategy of the PEC condition implementation of the E_x and E_z components. It shows that the method that the PEC condition is directly incorporated within the tri-diagonal matrix is more accurate and the computation burden of this method is trivial. The

theory proposed in this article is validated through numerical example.

II. PEC CONDITION IMPLEMENTATION FOR THE NWCS-FDTD METHOD

Considering the PEC condition implementation for the E_x and E_z components, the updating of the H_y component become,

$$H_y^{n+1} = H_y^n + \frac{\Delta t \partial}{2\mu \partial x} l_z \times (E_z^{n+1} + E_z^n) - \frac{\Delta t \partial}{2\mu \partial z} l_x \times (E_x^{n+1} + E_x^n) \quad (1)$$

where, μ is permeability of the medium; n and Δt are the index and size of time-step; l_x and l_z are the length factors. At the surface of the perfect-electric-conductor, the values of the length factors are zeros; at other mesh points, the values of l_x and l_z are equal to 1.

The updating equations of the E_x and E_z components are same as those in the reference [9],

$$E_x^{n+1} = E_x^n + \frac{\Delta t \partial}{\epsilon \partial y} H_z^{n+1/2} - \frac{\Delta t \partial}{2\epsilon \partial z} (H_y^{n+1} + H_y^n) \quad (2)$$

$$E_z^{n+1} = E_z^n - \frac{\Delta t \partial}{\epsilon \partial y} H_x^{n+1/2} + \frac{\Delta t \partial}{2\epsilon \partial x} (H_y^{n+1} + H_y^n) \quad (3)$$

Substituting equations (2) and (3) into equation (1), and approximating each derivative in space by centered second-order finite differences, the updating equation for H_y field is given as,

$$H_y^{n+1} \left(i + \frac{1}{2}, j, k + \frac{1}{2} \right) - \frac{b'}{\Delta x^2} \left[l_z \left(i + 1, j, k + \frac{1}{2} \right) \times \left[H_y^{n+1} \left(i + \frac{3}{2}, j, k + \frac{1}{2} \right) - H_y^{n+1} \left(i + \frac{1}{2}, j, k + \frac{1}{2} \right) \right] - l_z \left(i, j, k + \frac{1}{2} \right) \times \left[H_y^{n+1} \left(i + \frac{1}{2}, j, k + \frac{1}{2} \right) - H_y^{n+1} \left(i - \frac{1}{2}, j, k + \frac{1}{2} \right) \right] \right] - \frac{b'}{\Delta z^2} \left[l_x \left(i + \frac{1}{2}, j, k + 1 \right) \times \left[H_y^{n+1} \left(i + \frac{1}{2}, j, k + \frac{3}{2} \right) - H_y^{n+1} \left(i + \frac{1}{2}, j, k + \frac{1}{2} \right) \right] - l_x \left(i + \frac{1}{2}, j, k \right) \times \left[H_y^{n+1} \left(i + \frac{1}{2}, j, k + \frac{1}{2} \right) - H_y^{n+1} \left(i + \frac{1}{2}, j, k - \frac{1}{2} \right) \right] \right]$$

$$= H_y^n \left(i + \frac{1}{2}, j, k + \frac{1}{2} \right) - \frac{b'}{\Delta x^2} \left[l_z \left(i + 1, j, k + \frac{1}{2} \right) \times \left[H_y^n \left(i + \frac{3}{2}, j, k + \frac{1}{2} \right) - H_y^n \left(i + \frac{1}{2}, j, k + \frac{1}{2} \right) \right] - l_z \left(i, j, k + \frac{1}{2} \right) \times \left[H_y^n \left(i + \frac{1}{2}, j, k + \frac{1}{2} \right) - H_y^n \left(i - \frac{1}{2}, j, k + \frac{1}{2} \right) \right] \right] - \frac{b'}{\Delta z^2} \left[l_x \left(i + \frac{1}{2}, j, k + 1 \right) \times \left[H_y^n \left(i + \frac{1}{2}, j, k + \frac{3}{2} \right) - H_y^n \left(i + \frac{1}{2}, j, k + \frac{1}{2} \right) \right] - l_x \left(i + \frac{1}{2}, j, k \right) \times \left[H_y^n \left(i + \frac{1}{2}, j, k + \frac{1}{2} \right) - H_y^n \left(i + \frac{1}{2}, j, k - \frac{1}{2} \right) \right] \right] - S_{xy} \left\{ l_z \left(i + 1, j, k + \frac{1}{2} \right) \times \left[H_x^{n+1/2} \left(i + 1, j + \frac{1}{2}, k + \frac{1}{2} \right) - H_x^{n+1/2} \left(i + 1, j - \frac{1}{2}, k + \frac{1}{2} \right) \right] - l_z \left(i, j, k + \frac{1}{2} \right) \times \left[H_x^{n+1/2} \left(i, j + \frac{1}{2}, k + \frac{1}{2} \right) - H_x^{n+1/2} \left(i, j - \frac{1}{2}, k + \frac{1}{2} \right) \right] \right\} - S_{xz} \left\{ l_x \left(i + \frac{1}{2}, j, k + 1 \right) \times \left[H_z^{n+1/2} \left(i + \frac{1}{2}, j + \frac{1}{2}, k + 1 \right) - H_z^{n+1/2} \left(i + \frac{1}{2}, j - \frac{1}{2}, k + 1 \right) \right] - l_x \left(i + \frac{1}{2}, j, k \right) \times \left[H_z^{n+1/2} \left(i + \frac{1}{2}, j + \frac{1}{2}, k \right) - H_z^{n+1/2} \left(i + \frac{1}{2}, j - \frac{1}{2}, k \right) \right] \right\} - \frac{\Delta t}{\mu \Delta z} \left[l_x \left(i + \frac{1}{2}, j, k + 1 \right) \times E_x^n \left(i + \frac{1}{2}, j, k + 1 \right) - l_x \left(i + \frac{1}{2}, j, k \right) \times E_x^n \left(i + \frac{1}{2}, j, k \right) \right] + \frac{\Delta t}{\mu \Delta x} \left[l_z \left(i + 1, j, k + \frac{1}{2} \right) \times E_z^n \left(i + 1, j, k + \frac{1}{2} \right) - l_z \left(i, j, k + \frac{1}{2} \right) \times E_z^n \left(i, j, k + \frac{1}{2} \right) \right] \quad (4)$$

$$\text{where, } b' = \frac{\Delta t^2}{4\epsilon\mu}, S_{xy} = \frac{\Delta t^2}{2\epsilon\mu\Delta x\Delta y}, \text{ and } S_{xz} = \frac{\Delta t^2}{2\epsilon\mu\Delta x\Delta z}.$$

The other updating of the E_y , H_x and H_z components are according to the scheme shown in reference [9] and the implementation of the PEC condition for the E_y component is according to the strategy presented in reference [3].

III. NUMERICAL VALIDATION

To demonstrate the accuracy and efficiency of the proposed theory, a numerical example is presented here. A metal plate with dimension 60mm \times 60mm is shown in Fig. 1. Twenty five apertures of 2 mm length and 2 mm width are cut on the plate. All the distances between the apertures are 10 mm. A uniform plane wave polarized along the z -direction is normally incident on the aperture, and the time dependence of the excitation function is as follows,

$$E_z(t) = \exp\left[-\frac{4\pi}{T^2}(t-t_0)^2\right] \quad (5)$$

where T and t_0 are constants, and both equal to 2×10^{-9} s. In such a case, the highest frequency of interest is 1 GHz and the smallest wavelength is 0.3m. The observation point is set at the front of the plate and is 50mm far from the plate.

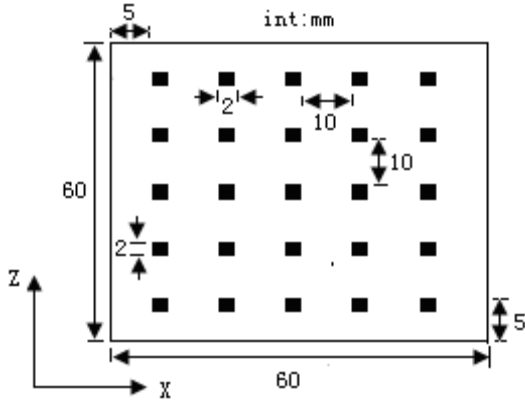


Fig. 1. Geometric configuration of the metal plate.

Applying the FDTD method to compute the time domain electric field component E_z at the observation point, to simulate the apertures precisely, the cell size around the aperture must be small. We choose $\Delta x = \Delta z = 0.5$ mm around the apertures. The cell size Δy is set to be 25mm which is 1/12 of the smallest wavelength of interest. The computational region is $60 \times 30 \times 60$ meshes. To satisfy the stability condition of the FDTD algorithm, the time-step size for the conventional FDTD is $\Delta t \leq 1.17$ ps. For the NWCS-FDTD scheme, the maximum time increment is only related to the space increments Δy , that is, $\Delta t \leq 83.33$ ps. The outer boundary of computational region is truncated by using the 5 layers CPML absorbing boundary condition.

There are two methods to implement the PEC boundary condition for the E_x and E_z components in the NWCS-FDTD scheme, referred as NWCS-FDTD-1 and NWCS-FDTD-2, respectively. In NWCS-FDTD-1 scheme, it solves the H_y component by using equations (13) and (14) in reference [9], then set the tangential electric field values at the boundary to be zeros directly after the E_x and E_z components are updated by using

equations (2) and (3). The NWCS-FDTD-2 method is also to set the tangential electric field values at the boundary to be zeros directly, but the component H_y is implicitly updated by using equation (4).

To demonstrate the high computational efficiency and accuracy of the NWCS-FDTD method, we perform the numerical simulations for a 5 ns time history by using the conventional FDTD, NWCS-FDTD-1 and NWCS-FDTD-2 methods, and compare the computation times and accuracy of these methods. In the conventional FDTD method, the time-step size keeps a constant of 1.17 ps. While in the NWCS-FDTD method, we use time-step size 83.33 ps.

Figure 2 shows the electric field component E_z at observation point calculated by using the conventional FDTD, NWCS-FDTD-1 and NWCS-FDTD-2 methods. It can be seen from this figure that the result calculated by the NWCS-FDTD-2 method agrees well with the result calculated by the conventional FDTD method, but a large deviation of the NWCS-FDTD-1 method from the conventional FDTD method is observed. It is apparent that the NWCS-FDTD-2 method has higher accuracy than the NWCS-FDTD-1 method with same time step size, which is due to that in the NWCS-FDTD-2 method, the implementation of the PEC boundary condition for the E_x and E_z components is incorporated within the solving of the H_y component by using equation (4).

To complete this simulation, the computation times for the conventional FDTD method, NWCS-FDTD-1 method and NWCS-FDTD-2 method are 761.58, 30.08, and 31.12 seconds, respectively. Due to the large time step size applied, the CPU time for the NWCS-FDTD-2 and NWCS-FDTD-1 methods are almost 1/25 of that for the conventional FDTD method. The computation time of the NWCS-FDTD-2 method is a little more than that of the NWCS-FDTD-1 method, because in the NWCS-FDTD-2 method, the updating of the H_y component need to multiply the length factors, but the burden is trivial in comparison with the computation time of the conventional FDTD method.

It should be noted that the PEC modeling accuracy is inversely proportional to the CFLN

value which is defined as the ratio of the time step size of WCS-FDTD and FDTD methods. In [9], the CFLN value is only 16. The PEC modeling inaccuracy is not obvious. So in that reference, there was little evidence of PEC modeling inaccuracy. While, in this paper, CFLN=71, the PEC modeling inaccuracy of WCS-FDTD-1 method becomes significant. In such case, the component H_y must be updated by using equation (4).

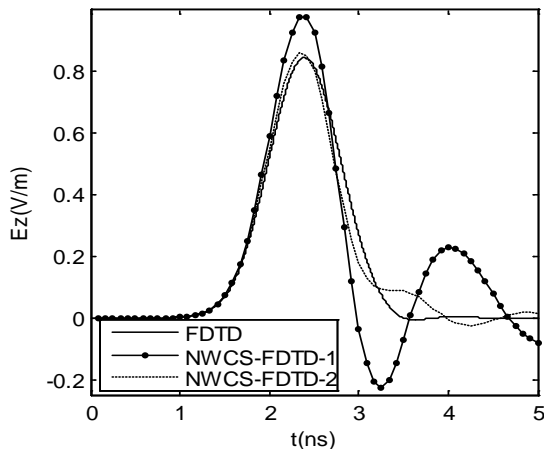


Fig. 2. The comparison of the results calculated by using the conventional FDTD, NWCS-FDTD-1, and NWCS-FDTD-2 methods.

IV. CONCLUSION

Two strategies for the PEC condition implementation for the NWCS-FDTD method are compared in this paper. It shows that only the method that the PEC condition is directly incorporated within the solution of the H_y component is accurate. The computational complexity of this method and the burden on the computation efficiency are trivial, which is validated by numerical example.

The NWCS-FDTD-2 method is useful for all problems where a very fine mesh is needed in one or two directions, regardless of whether the PEC condition exists. For the PMC condition, the implementation method is similar to the scheme described in reference [3].

ACKNOWLEDGMENT

This work was supported by National Natural Science Foundations of China (No. 61001039), and by the Research Fund for the Doctoral Program of Higher Education of China (No. 20090201120030).

REFERENCES

- [1] T. Namiki, "3-D ADI-FDTD Scheme-Unconditionally Stable Time-Domain Algorithm for Solving Full Vector Maxwell's Equations," *IEEE Trans. Microwave Theory Tech.*, vol. 48, pp. 1743–1748, Oct. 2000.
- [2] F. Zheng, Z. Chen, and J. Zhang, "A Finite-Difference Time-Domain Method without the Courant Stability Conditions," *IEEE Microwave Guided Wave Lett.*, vol. 9, pp. 441–443, Nov. 1999.
- [3] J. Chen and J. Wang, "PEC Condition Implementation for the ADI-FDTD Method," *Microw Opt. Tech. Lett.*, vol. 49, pp. 526–530, Mar. 2007.
- [4] J. Chen and J. Wang, "A Frequency-Dependent Weakly Conditionally Stable Finite-Difference Time-Domain Method for Dispersive Materials," *Applied Computational Electromagnetics Society (ACES) Journal*, vol. 25, pp. 665–671, Aug. 2010.
- [5] J. Chen and J. Wang, "An Unconditionally Stable Subcell Model for Thin Wires in the ADI-FDTD Method," *Applied Computational Electromagnetics Society (ACES) Journal*, vol. 25, pp. 659–664, Aug. 2010.
- [6] G. Sun and C. W. Trueman, "Accuracy of Three Unconditionally-Stable FDTD Schemes," *Applied Computational Electromagnetics Society (ACES) Journal*, vol. 18, pp. 41–47, Nov. 2003.
- [7] I. Ahmed and Z. Chen, "Error Reduced ADI-FDTD Methods," *IEEE Antennas Wireless Propag. Lett.*, vol. 4, pp. 323–325, Apr. 2005.
- [8] J. Chen and J. Wang, "Error between Unconditionally Stable FDTD Methods and Conventional FDTD Method," *Electron. Lett.*, vol. 42, pp. 1132–1133, Sept. 2006.
- [9] J. Chen and J. Wang, "Weakly Conditionally Stable Finite-Difference Time-Domain Method," *IET Microwaves, Antennas & Propagation*, vol. 4, pp. 1927–1936, Nov. 2010.
- [10] J. Chen and J. Wang, "A Novel WCS-FDTD Method with Weakly Conditional Stability," *IEEE Trans. Electromag. Compat.*, vol. 49, no. 2, pp. 419–426, 2007.
- [11] S. Niu, Y. Yang, R. S. Chen, and S. B. Liu, "Weakly Conditionally Stable Finite-Difference Time-Domain Method for Simulation of Resonant Cavity," *ICMMT 2010 Proceedings, Chendu*, pp. 801–804, 2010.
- [12] J. Chen and J. Wang, "Weakly Conditionally Stable and Unconditionally Stable FDTD Schemes for 3D Maxwell's Equations," *Progress in Electromagnetics Research B*, vol. 19, pp. 329–366, 2010.



Juan Chen was born in Chongqing, China, in 1981. She received the Ph.D. degree in Electromagnetic Field and Microwave Techniques at the Xi'an Jiaotong University, Xi'an, China, in 2008. She now serves as associate professor at Xi'an Jiaotong University. Her research interests are the numerical electromagnetic methods, antenna designs, and electromagnetic compatibility.



Jianguo Wang was born in Jiangsu Province, China, on December 21, 1965. He received the B.S. degree in Physics from Nanjing University, Nanjing, China in 1987 and the M.S. degree in Physics from the Northwest Institute of Nuclear Technology (NINT), Xi'an Shaanxi, China in 1990, and the Ph.D. degree in Electromagnetic Theory and Microwave Techniques from Xidian University, Xi'an, Shaanxi, in 1997. From 1998 to 2000, he conducted his postdoctoral research at the Department of Electrical and Computer Engineering, University of Illinois at Urbana-Champaign.

He now serves as a professor at NINT. He also works part-time as a Professor in the School of Electronic and Information Engineering, Xi'an Jiaotong University, Xi'an, China. His research interests mainly include transient electromagnetics, numerical electromagnetic methods, antenna designs, and plasma physics.



Chunming Tian received the Ph.D. degree in Radio Physics from Xidian University, Xi'an, China, in 2003. He now serves as a lecturer at Xi'an Jiaotong University. His research interests are Computational Electromagnetics, Transient electromagnetic Scattering, and antenna designs.

Analysis and Application of Inverse Detecting Method Based on Local Electric Field

Zhanlong Zhang¹, Zhenhai Zhu¹, Qin Xin^{2,3}, Xuemei Xie¹, Jian Lei¹, and Song Huang¹

¹ State Key Laboratory of Power Transmission Equipment & System Security and New Technology, Chongqing University, P.R. China, 400044
zhangzl@cqu.edu.cn, cqzhu-zhenhai@163.com

² Faculty of Science and Technology, University of the Faroe Islands, Torshavn, Faroe Islands

³ Department of Computer Science, University of Copenhagen, Copenhagen, Denmark

Abstract — This paper investigates the time-efficient fault detection problem with applications in electric fields. A novel inverse approach based on a non-trivial combination of the fast multipole scheme and traditional simulation charge method is proposed. The fundamental principle is to take several samples of the intensity in the given local electric field at properly selected known locations nearby. Electric accessories are then used to analyze the signals in the framework of the traditional simulation charge method. Moreover, a new genetic algorithm, combined with the Tikhonov regularization, is proposed to further speed up the inverse process of fault detection in electric fields. The performance of the proposed approach is evaluated by the simulation results for the computation of the distribution of voltages in 110 kV high-voltage insulator lines. The superiority of the new inverse approach, in terms of time efficiency and accuracy for fault detection, is demonstrated by the simulation results. The present work aims to stimulate future studies on fault detection in electric fields.

Index Terms - Electric fields, fast multipole method, genetic algorithms, inverse problems, Tikhonov regularization.

I. INTRODUCTION

Online fault detection and condition maintenance without switching off the system are the most challenging problems in electric fields.

These are very important factors that must be taken into account in the design of high-voltage electrical systems [1]. The safety and regular operation in power systems must always be ensured. The current research focused its attention on these factors and on measurements of insulation resistance, hyper frequency, acoustics and supersonics, as well as on the infrared imaging method. However, few relevant research materials have focused on the accuracy of fault detection in electric fields, which is one of the most important metrics for evaluating the performance of methodologies.

The present paper takes the electric-field intensity as the main metric for received signals. It is not only a very important factor to be monitored, it is also easily captured. From the analysis of the samples on the electric-field intensity of several properly preselected locations nearby, as well as the electric equipment combined with a new geometry model from a tuning version of the traditional simulation charge method, this paper compares the practical voltage distribution of the high voltage electrical equipment derived by the proposed inverse approach with standard voltage distribution. Consequently, the locations of the fault devices are detected.

II. CALCULATION PRINCIPLE

A. Model and the inverse approach for the simulation charge method

Establishing a proper calculating model is very crucial in deriving efficiency in

computations. According to high voltage power frequency electric properties and the superiority of the simulation charge method in the calculation of open domain problems, the calculation model is derived from the simulation charge method (SCM) [2,3]. The theoretical basis of SCM is the uniqueness principle of the electric fields based on imaging methods. Instead of unevenly and continuous distributed charges on the conductor surface, this work uses a set of simulation charges that meet the given boundary conditions to formulate a solution for the entire field. According to the simulation theory in literature, the shape of the simulation charge is random. The shape of the actual electric field source and the feature of the electric field usually serve as the reference when selecting the shape of the simulation charge to simplify the calculations. For instance, an infinitely long line of charge is simulated by the high voltage (HV) transmission line, whereas the ring simulated charge is used to substitute the chained charges on the surface of the insulators.

Detailed steps on establishing the relationship between the electric field and the source using SCM are as follows. The first step is to conduct a qualitative analysis of the feature of the electric field and set several simulation charges outside the corresponding calculation field. The second step is to configure the matching points with exactly the same number as the simulation charges. The third step is to establish the potential SCM expressions according to the superposition principle. In solving the corresponding SCM equations, several checkpoints on the surface of the electrode are selected to evaluate the precision of the calculations. The selection processes for the simulation charges, in terms of locations, are completed until the calculation precision meets the predefined requirement threshold. Finally, the potential or intensity of the electric field on the randomly selected points would be determined according to the final values of the selected simulation charges.

This work takes the seven-piece insulators of a 110 kV line as an example. The process of the calculation model is illustrated using the SCM as follows. Simulation uses the two-ring simulation charges. Each corresponding insulator has two matching points on the surface. Each matching point has the exact same Z-coordinates as the corresponding simulation charge. The employed

geometric model is shown in Fig. 1.

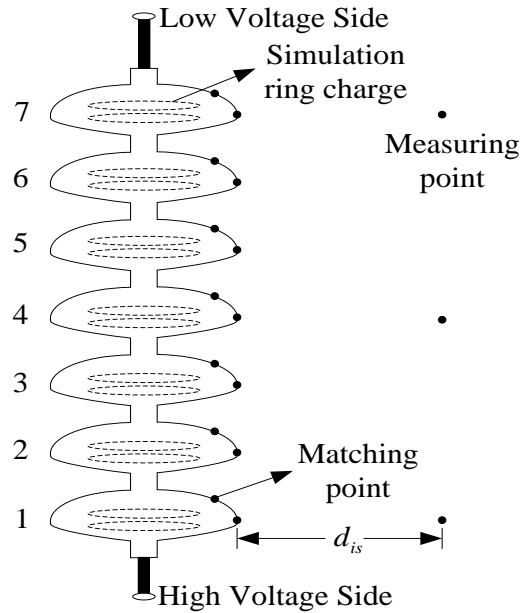


Fig. 1. Configuration of the simulation charges and matching points of the insulator of the 110 kV line.

Each corresponding piece of the insulator is numbered from 1 to 7, scaled from high voltage to low voltage. Assuming that the charges for the simulation ring are $Q_1, Q_2 \dots Q_{14}$ and the corresponding ring potentials of the matching points are $\varphi_1, \varphi_2 \dots \varphi_{14}$, respectively, \mathbf{P} denotes the potential coefficient matrix. Consequently, the potential expressions based on SCM are expressed as follows.

$$\mathbf{U} = \mathbf{P}\mathbf{q}, \tag{1}$$

$$\mathbf{f}_r \mathbf{q} = \mathbf{E}_r, \tag{2}$$

$$\mathbf{f}_z \mathbf{q} = \mathbf{E}_z, \tag{3}$$

where \mathbf{q} and \mathbf{U} are the charge single matrix and the voltage single matrix, respectively. \mathbf{E}_r and \mathbf{E}_z denote the r-axis and z-axis components of the electric-field intensity matrix in the cylindrical coordinate, respectively. \mathbf{f}_r and \mathbf{f}_z are the r-axis and z-axis components of the electric-field intensity coefficient matrix in the cylindrical coordinate, respectively.

By solving the quantity of the simulation charges (e.g., equation (1)), the potential distribution or electric-field distribution is determined. This process is an electric-field forward problem used to figure out the potential

distribution or electric-field distribution in the field through solving for the potential or electric-field intensity of matching points, whereas the electric-field inverse problem refers to the calculation of the potentials of the boundary points in the corresponding electric fields. In the insulator model described above, the inverse application of the SCM is aimed to estimate the electric-field intensity of several points near the insulator string and to calculate the potential distribution values on the surface of the insulator string using an optimization algorithm. The location of the fault insulators is identified by comparing the computed distribution with the standard distribution. Figure 1 illustrates the model, in which three measuring points are chosen with exactly the same level as the pieces of No. 1, No. 4, and No. 7 in the 110 kV insulator.

B. Fast multipole preprocessing

To reduce the workload for the measurements, fewer points are selected in building the calculation model of the HV electric accessory by the traditional simulation charge method. When the number of measuring points is less than the number of simulation charges, the calculation of the fundamental equation for the inverse problem is underdetermined by the system of equations [4], abstracted by the model for the problem with n source points and corresponding m field points ($n > m$). By solving the least squares solution with a certain constraint, the potential is obtained at every point. However, the traditional method needs an extremely high calculation complexity to calculate each corresponding field point and source point in the original electric field. To improve the efficiency of the matrix multiply vector and to reduce the dimension of the coefficient matrix, the fast multipole method is used to preprocess the traditional SCM model. This model simplifies the electric relationship between the field points and source points through the procedure of “polymerization-transition-disposition”. The main idea of the fast multipole method is to polymerize the effects of n source points to the center point O of the source points and to shift the effects of the center point O to the center point O' of the field, followed by the calculation of the electric-field intensity of each field point from center point O' [5].

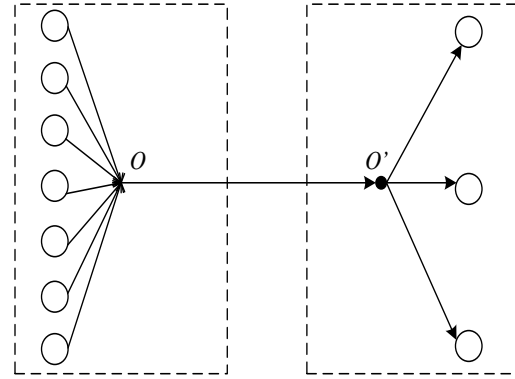


Fig. 2. Schematic diagram of the fast multipole method

According to the principle of superposition, the potentials of n simulation charges at the i th matching point is calculated as follows,

$$\varphi_i = \sum_{j=1}^n p_{ij} q_j, \quad (4)$$

where p_{ij} is the potential coefficient for the j th simulation charge with the corresponding i th matching point. For the accumulation problem, such as in equation (4), the calculation complexity is bounded by $O(m*n)$. The values of the potential coefficients have nothing to do with the quantity of charges. However, it is determined by the shapes and positions of simulation charges, the geometric positions of field points, and dielectric constants of the mediator. To improve the calculation complexity and solve equation (4), $p(r, z)$ is expanded as follows.

$$p(r, z) \approx \sum_{k=1}^N \phi_k(r - R_x) W_k(R_x - R_y) \psi_k(z - R_y), \quad (5)$$

$$|R_x - R_y| > |(r - R_x) - (z - R_y)|, \quad (6)$$

where ϕ_k , W_k , and ψ_k are the shape functions, independent of the potential, R_x and R_y , which are the points near r and z , respectively. To further improve the calculation speed, n source points are divided into M group, G_x , $x = 1, 2 \dots M$. For each corresponding group G_x , the close and far field groups are found first. Afterward, different calculation methods are used to handle the close and far field groups, which are computed directly by the methods of “polymerization-transition-disposition”.

However, in the insulator string model mentioned above, both the source points and field points are illustrated vertically. Consequently, the distance between the source points and field points

are relatively uniform. In this case, the calculation is simplified, e.g., all groups are considered as a far field group. That is, for point q of each group G_x , multi-stage expansion is used to calculate φ_i . The specific computation formula is shown in equation (7).

$$\varphi_i \Big|_{q \in I_x} = \sum_{k=1}^N A_{x,k} \phi_k (r - R_x), \quad (7)$$

$$x = 1, 2, \dots, M$$

where

$$A_{x,k} = \sum_{I_y} W_k (R_x - R_y) B_{y,k}, \quad (8)$$

$$x = 1, 2, \dots, M; k = 1, 2, \dots, N$$

$$B_{y,k} = \sum_{r \in I_y} q_j \psi_k (r - R_y), \quad (9)$$

$$y = 1, 2, \dots, M; k = 1, 2, \dots, N$$

where equations (7), (8), and (9) denote the field effects from the source of each group to the center. The field effects are due to the shifting from the field of the group center to the corresponding points of the group, as well as the assignments of the field effects of the group center to each of the field points in the corresponding group, respectively. The proposed approximation scheme above heavily reduces the complexity of the computation.

III. INVERSE DETECTING METHOD

Based on the analysis mentioned above, the implementation steps of the inverse detecting method based on electric field intensity are given as follows.

Step 1: Derive a qualitative analysis for the awaiting detection equipment and surrounding field. Simulate the awaiting detection equipment using the traditional simulation charge method. Determine the shape, quantity, and position of simulation charge. Set as few measuring points near the equipment as possible to reduce the measuring workload, in accordance with the principle of balance. Obtain the coordinates of each simulation charge, matching point, and measuring point. Build the calculation model, thus forming the SCM basic relation between the field and source, such as in equations (1), (2), and (3).

Step 2: Obtain the electric-field intensity distribution of the measuring point by measuring the apparatus online. Establish the set of

equations, such as in equation (4), according to the principle of superposition. Treat them according to equations (5) and (6). Serve all simulation charges as source points. Divide them into several groups and find the close field group as well as the far field group. Perform the preconditioning of the fast multipole, such as in equations (7), (8), and (9).

Step 3: Choose the optimization method. Establish the target function. Optimize and calculate the inverse problem on the basis of fast multipole preconditioning. Obtain the actual potential distribution on the surface of the equipment. The actual potential distribution curves are compared with the national standard reference data. Then, check for faults and fault positions, thus realizing inverse detection based on the signal of the electric field.

IV. OPTIMIZATION ALGORITHM

This section will show how to derive an optimal allocation with the application of the SCM elementary model by the fast multipole method. The main principle for such an approach is to reverse the calculation of the source parameter by measuring the electric field intensity of certain points near the insulators. This procedure aims to extrapolate “the reason” based on the measured “effect”. In real situations, proper solutions to these problems are normally difficult to obtain with the absence of special methods. Therefore, the key to the solution of the electric-field inverse problem is to seek a proper optimization algorithm as well as to solve the corresponding inverse problem. The solution should show the way to work out fault detection in electric fields. This paper employed genetic algorithm (GA) and the regularization technique [6, 8].

A. Analysis of GA

The operation of GA is based on the code of parameters instead of the parameter itself. This does not require functional continuity or differentiability. GA calculates the match value through the objective function and does not require other derivation and subsidiary information, thus having less dependency on the problem itself. The insulator inverse problem (Fig. 1) is taken as an example to analyze GA optimization procedure through real coding in the electric-field inverse problem. GA with the real

number coding avoids the coding and decoding procedures. Therefore, it improves the calculation efficiency.

In the process of the application of GA to solve the insulator inverse problem, the potential distribution \mathbf{U} is considered as an optimization variable, and the object function is defined as follows:

$$\min f = \frac{1}{n} \sum_{i=1}^n \left| \sqrt{E_{ir}^2 + E_{iz}^2} - E_{oi} \right|, \quad (10)$$

where E_{oi} is the measured value of the i^{th} point, E_{ir} and E_{iz} are the r -axis and z -axis components of the calculated values, respectively.

More precisely, the application of GA in the insulator inverse problem takes the following steps.

Step 1: Initialize the position of the simulation charges, matching points, and the intensity \mathbf{E}_0 of measuring points. Randomly generate 50 initial populations.

Step 2: Calculate the voltage distribution \mathbf{U}_0 of the matching points and potential coefficient matrix \mathbf{P} .

Step 3: Calculate the quantities of the simulation charges according to $\mathbf{q} = \mathbf{P}^{-1}\mathbf{U}_0$, and calculate the electric-field intensity coefficient matrix \mathbf{f}_r and \mathbf{f}_z of the measuring points and $\mathbf{E}_i = \sqrt{\mathbf{E}_{ir}^2 + \mathbf{E}_{iz}^2}$.

Step 4: calculate the adaptive value $\min f = \frac{1}{n} \sum_{i=1}^n |\mathbf{E}_i - \mathbf{E}_{oi}|$ of the object function of the current population, and examine whether it meets the convergence criteria. If yes, let \mathbf{U} be the actual voltage. Otherwise, it generates a new filial population from the selection. Crossover the variation calculations followed by Step 2 again.

B. Analysis of Tikhonov regularization

The condition of the inverse problem is contributed by the filtration function of the positive operator. The distinctness of the different solution is strained away after mapping by the positive operator. In addition, the data are obtained through discrete and finite observations after being polluted by noise, further intensifying the fault detection problem. To solve the fault detection problem, prior information binding into the regularization technique should be increased [7]. Coupling the prior information to the solving

process of the inverse problem approximates the inverse operator through a better operator, thereby enabling the recovery of lost information.

The exact solution to the inverse problem is normally difficult to solve in a time-efficient manner. Therefore, the least squares method is employed to seek the approximate solution for the linear system of equations $\mathbf{Ax} = \mathbf{y}$, which is the minimum norm $\|\mathbf{Ax} - \mathbf{y}\|^2$. This paper transfers the inverse problem into the problem to solve \mathbf{q}^* (e.g., a functional extreme problem) according to the least squares method:

$$\min_{\mathbf{q} \in Q} \|\mathbf{fq} - \mathbf{E}\|^2, \quad (11)$$

where \mathbf{E} is the measured value of the electric-field intensities from the measuring points. The charges on the surface of insulators are bounded. Equation (11) meets the boundary condition: $\sum_{i=0}^m q_i = 0$.

Moreover, proof is presented that equation (12) is equivalent with the above extreme value problem, named the normal equation of equation $\mathbf{E} = \mathbf{fq}$:

$$\mathbf{f}^* \mathbf{fq} = \mathbf{f}^* \mathbf{E}, \quad (12)$$

where \mathbf{f}^* is associated operator of \mathbf{f} . The normal equation (12) inherited and exacerbated the ill condition of the original equation, thus necessitating the increase of a penalty term $\alpha \|\mathbf{q}\|^2$ to punish \mathbf{q} , which is a norm that is too large to solve the fault detection of the above extreme value problem. To obtain better performance, equation (11) is rewritten as:

$$\min_{\mathbf{q} \in Q} \left(\|\mathbf{fq} - \mathbf{E}\|^2 + \alpha \|\mathbf{q}\|^2 \right). \quad (13)$$

Therefore, $\|\mathbf{fq} - \mathbf{E}\|^2 + \alpha \|\mathbf{q}\|^2$ is transformed into a Tikhonov function and the solution \mathbf{q}_α of the extreme value problem such as that in equation (13). The only solution of the normal equation is

$$\mathbf{f}^* \mathbf{fq}_\alpha + \alpha \mathbf{q}_\alpha = \mathbf{f}^* \mathbf{E}. \quad (14)$$

Further calculation for the corresponding components is done by the following equation:

$$\mathbf{q}_\alpha = \left(\mathbf{f}^* \mathbf{f} + \alpha \mathbf{I} \right)^{-1} \mathbf{f}^* \mathbf{E}. \quad (15)$$

The next step is to determine the iterative method after having the optimal target function such as in Equation (13). The Newton iteration algorithm is adopted to solve the insulator electrical inverse problem. The concrete calculation process is given as follows:

Step 1: Choose the initial solution q_0 and regularization parameter α . The selection method of the regularization parameter is given as a reference.

Step 2: Calculate the object function $J_\alpha(q) = \|fq - E\|^2 + \alpha\|q\|^2$.

Step 3: Examine the condition of the convergence. If the adaptive value satisfies the condition of convergence, it exits the procedure. Otherwise, it repeats Step 2.

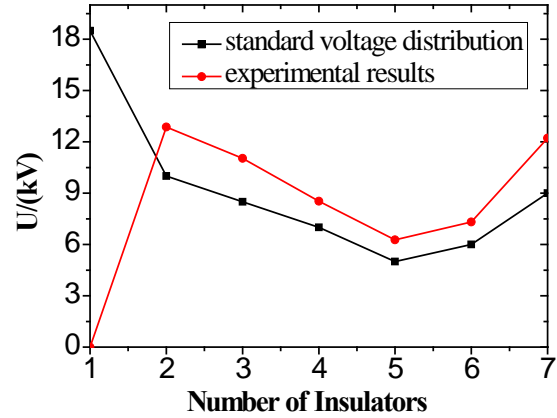
V. EXAMPLE CALCULATION AND ANALYSIS

Figure 1 shows one phase insulator string under 110 kV. Each insulator string has seven slices. The distribution of the charge is simulated by two ring simulation charges and two matching points chosen on the surface of each insulator. For the test, $r=0.127m$, $h=0.146m$, $h_0=15m$, $l=0.5m$, where r is the radius of each insulator; h is the actual height of each insulator; h_0 is the terrain clearance of the first insulator; l is the horizontal distance between the measuring point and insulator string. In addition, according to the principle of optimal radius, the radius of the ring simulation charge is 4 m.

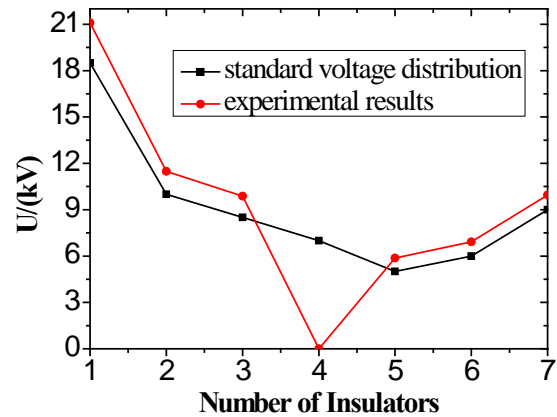
The normal voltage distributions of each insulator are in the order of 18.5, 10.0, 8.5, 7.0, 5.0, 6.0, and 9.0 kV (from number 1 to 7). Through the measurement of the insulation resistance, the fault insulator may be obtained from the power supply company. In this work, number 1, 4, and 7 insulators are separately replaced as fault insulators. Thus, in this case, the measured value of three groups of the electric field intensity in three measuring points would be obtained by the measuring apparatus. Table 1 illustrates the experimental results in the case with $l=0.5$ m.

Table 1: Electric-field intensity at 3 measuring points (kV/m)

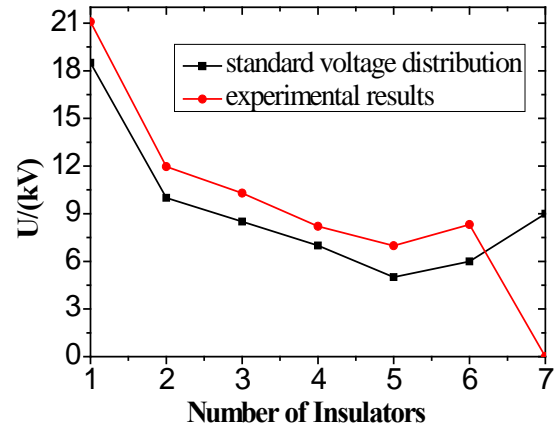
Number	Without faulty	No. 1 insulator is fault	No. 4 insulator is fault	No. 7 insulator is fault
1	9.0475	3.6718	8.9915	9.2796
2	5.0248	4.9232	3.3699	5.6537
3	4.3841	4.7398	4.2103	2.8172



(a) Scenario under a faulty No.1 insulator



(b) Scenario under a faulty No.4 insulator



(c) Scenario under a faulty No.7 insulator

Fig. 3. Comparison between actual and normal values.

After inducing the model parameters and electric field intensity of the measuring points in the calculation program, the voltage distribution curve of every insulator is obtained through either GA or Tikhonov regularization. The calculation

results show that the proposed method obtains the expected one. The trend of the curve is given as follows.

The experimental calculation results show that the relative errors are controlled within the allowed interval. The errors caused by the shift of the measuring points are indispensable. Therefore, this work aims to analyze the errors caused by the shift in the measuring points. The conclusions are given as follows.

(1) Voltage distribution changes significantly when the measuring points shift at the horizontal direction. The analysis shows that the corresponding error is less than 20% when the shift distance of the corresponding measuring points is approximately 0.5 m at the horizontal direction based on the GA. However, the voltage distribution changes very little when the measuring points shift at the vertical direction.

(2) By inducing more parameters into the calculation program of the Tikhonov regularization, the errors are reduced to 13%. Further, the intervention of the regularization technique is helpful to speed up the process.

VI. CONCLUSION

This paper proposed a novel inverse approach for the fault detection problem in electric fields. The approach is based on a non-trivial combination of the fast multipole scheme and traditional simulation charge method. Moreover, a new genetic algorithm combined with the Tikhonov regularization is proposed to speed up the inverse process for fault detection in electric fields further. The superiority of the proposed new inverse approach, in terms of time efficiency and accuracy for fault detection, was demonstrated by the simulation results. The present work hopes to stimulate future studies on fault detection tasks in electric fields.

ACKNOWLEDGMENT

This project was supported by the Fundamental Research Funds for the Central Universities (Grant No. CDJZR10150016) and the Visiting Scholarship of State Key Laboratory of Power Transmission Equipment and System Security and New Technology (Grant No. 2007DA10512710408).

REFERENCES

- [1] F. Yang, H. Wu, W. He, T. Chen and D. Ni, "Investigation on the Electric Field Inverse Problem of HV Transmission Lines and Discussion on its Application," *Applied Computational Electromagnetics Society (ACES) Journal*, vol. 25, no. 2, pp. 129-136, Feb. 2010.
- [2] A. Adil, "A Changing Range Genetic Algorithm," *Int. J. Numer. Meth. Engng*, vol. 61, no. 15, pp. 2660-2674, Oct. 2004.
- [3] H. Singer, H. Steinbigler, and P. Weiss, "A Charge Simulation Method for the Calculation of High-Voltage Fields," *IEEE Trans. Power Appar. Syst.*, vol. PAS-93, no. 5, pp. 1660-1668, Sept. 1974.
- [4] J. Schreiber, J. Haueisen, and J. Nenonen, "A New Method for Choosing the Regularization Parameter in Time-Dependent Inverse Problems and its Application to Magnetocardiography," *IEEE Trans. Magn.*, vol. 40, no. 2, pp. 1104-1107, March 2004.
- [5] Z. L. Zhang, J. Deng, D. W. Li, Z. H. Zhu, Q. Hu and W. He, "Fast Multi-Pole Boundary Element Method Analysis for Power Frequency Electric Field Distribution of Multi-Medium," *Electric Machines and Control*, vol. 14, no. 4, pp. 80-85, 2010.
- [6] F. Herrera and M. Lozano, "Two-Loop Real-Coded Genetic Algorithms with Adaptive Control of Mutation Step Sizes," *Applied Intelligence*, vol. 13, no. 3, pp. 187-204, Nov. 2000.
- [7] J. Colinas, Y. Goussard, and J. - J. Laurin, "Application of the Tikhonov Regularization Technique to the Equivalent Magnetic Currents Near-Field Technique," *IEEE Transactions on Antennas and Propagation*, vol. 52, no. 11, pp. 3122-3132, Nov. 2004.
- [8] W. He, F. Yang, J. G. Wang, H. Yang, C. Minyou, and D. G. Yao, "Inverse Application of Charge Simulation Method in Detecting Faulty Ceramic Insulators and Processing Influence from Tower," *IEEE Transactions on Magnetics*, vol. 42, no. 4, pp. 723-726, April 2006.



Zhanlong Zhang was born in China in 1971. He received his B.Eng., M.Eng. and Ph.D. degrees from Chongqing University, China, in 1993, 2000 and 2004. As a post doctorate, he completed research work at the College of Biomedical Engineering, Chongqing University, China, in 2007. Currently, he is an associate professor of Electrical Engineering in the College of Electrical Engineering, Chongqing University, China and a visiting scholar in the School of Information Technology and Electrical Engineering, University of

Queensland, Australia. He is a member of International COMPUMAG Society (ICS). His research interests include electromagnetic measurement and calculation, fault monitoring of power transmission equipment.



interests include calculation.

Zhenhai Zhu was born in 1986 in China. He received his B.Eng. (Electrical Engineering) degree from Chongqing University, Chongqing, China, in 2009. Currently, he is studying for his master's degree (Electrical Engineering) in Chongqing University, China. His research



professor. He is also holding an adjunct professorship at University of Copenhagen, Denmark (under evaluation of the level). Prior to joining UoFI, he had held variant research positions in world leading universities and research laboratory including Senior Research Fellowship at Université Catholique de Louvain, Belgium, Research Scientist/Postdoctoral Research Fellowship at Simula Research Laboratory, Norway and Postdoctoral Research Fellowship at University of Bergen, Norway. His main research focus is on design and analysis of sequential, parallel and distributed algorithms for various communication and optimization problems in wireless networks and information management systems. Moreover, he also investigates the combinatorial optimization problems with applications in Bioinformatics and Data Mining. Dr. Xin has produced more than 55 scientific papers. His works have been published in leading international conferences and journals, such as ICALP, PODC, SWAT, IEEE MASS, ISAAC, SIROCCO, IEEE ICC, Algorithmica, Theoretical Computer Science, IEEE Transactions on Computers, and Distributed Computing. He has been very actively involved in the services for the community in terms of acting on various positions (e.g., Session Chair, Member of Technical Program Committee, Symposium Organizer and Local Organization Co-chair) for numerous international leading conferences in the fields of distributed computing, wireless communications and ubiquitous intelligence and computing, including IEEE

Qin Xin was born in China in 1977. He graduated with his Ph.D. (Oct. 2002 – Nov. 2004) in Department of Computer Science at University of Liverpool, UK in December 2004. Currently, he is working in Faculty of Science and Technology at the University of Faroe Islands (UoFI), Faroe Islands as an associate

MASS, LCN, ACM SAC, IEEE ICC, IEEE Globecom, IEEE WCNC, IEEE VTC, IFIP NPC, MoMM, IEEE AINA, HPCC, HPC, IEEE Sarnoff, UIC, ICOIN, NTMS and so on. Currently, he also serves on the editorial boards for more than ten international journals. Meanwhile he is a member on Advisory Board of International Association for Computer Scientists and Engineers.



University, China. Her research interests include electromagnetic compatibility and electromagnetic field calculations.

Xuemei Xie was born in 1989 in China. She received her B.Eng. (Bio-Medical Engineering) degree from Chongqing University, China, in 2007. Currently, she is studying for her master's degree (Electrical Engineering) in Chongqing

monitoring of power transmission equipment and application of wireless equipment.

Jian Lei was born in China in 1988. She received her B.Eng. (Automation) degree from Chongqing Business and Technology University in 2007. Currently, she is studying for her master's degree (Electrical Engineering) in Chongqing University, China. Her research interests include fault



and numerical calculation, electric machine design, control and analysis.

Song Huang was born in China in 1972. He received his B.Eng., M.Eng. and Ph.D. degrees from Chongqing University, China, in 1994, 2000, and 2005. Currently, he is a lecturer of Electrical Engineering in the College of Electrical Engineering, Chongqing University. His research interests include electromagnetic field theory

Low RCS Antenna Design Using Genetic Algorithm Combined with Tabu List

Xinyue Zhu, Wei Shao, and Jia-Lin Li

School of Physical Electronics
University of Electronic Science and Technology of China, Chengdu 610054, P. R. China
zhuxinyue888@163.com, weishao@uestc.edu.cn, jialinuestc@yahoo.com.cn

Abstract — In this paper, a simple and efficient approach is presented to reduce the radar cross section (RCS) of patch antennas with defected ground structures (DGSs). This approach consists of an optimization algorithm, which combines a genetic algorithm (GA) with tabu list, and electromagnetic field solver. A tabu list, embedded into the GA frame, defines the acceptable neighborhood region of parameters and screens out the bad individuals. Thus, the repeats of search are avoided and the amount of electromagnetic simulation is largely reduced. Moreover, the whole design procedure is auto-controlled by programming the VBScript language. A patch antenna example is provided to verify the accuracy and efficiency of the proposed design method.

Index Terms — Genetic algorithm, patch antenna, RCS reduction, tabu list, VBScript.

I. INTRODUCTION

In order to avoid detection by radar, a low visibility platform is desired eagerly to a low radar cross section (RCS) for applications. An antenna that is a special scatterer has become an important contributor to the RCS [1]. The shaping method, including the slot structure [2], fractal geometry [3], frequency selective surface (FSS) [4] and defected ground structure (DGS) [5], is one of the most effective methods for antenna RCS reduction. Due to the tradeoff between antenna radiation and scattering requirements, it is very complex and time-consuming to design antenna with good radiation performance and low RCS. Therefore, a combination of the numerical algorithm and optimization method is needed to

complete this design.

The genetic algorithm (GA), a global search method modeled on the natural processes of genetic recombination and evolution, has been widely used for solving complex electromagnetic (EM) problems [6]. Using GAs, [7] optimizes the backscattering RCS patterns of a resistively loaded antenna. In [8], radar absorbing materials (RAMs) for RCS reduction in a wide-band frequency range is designed to obtain the best optimal composite coating with a GA optimization technique. To reduce the RCS of the cone and cylinder composite structure, a GA is adopted to optimize the anisotropic impedance object in a desired angle range [9]. However, all of these efforts focus on the scattering of objects, and it is not effective for the simultaneous consideration of antenna radiation and scattering performance.

In [10], a low RCS antenna design using the differential evolution algorithm (DEA) in conjunction with the method of moments (MoM) is presented. However, the final fitness calculations for each generation involve both of the radiation and scattering factors, which maybe lead to an inefficient solution. Later, lower RCS patch antennas are optimized by combining the GA with high frequency simulation software (HFSS) [11]. Although this approach saves the calculation time, some known individuals with bad radiation performance are still sent to be simulated in HFSS. In [12], a hybrid GA with the tabu list concept is proposed to increase the search efficiency of the algorithm. The algorithm is applied to reconstruct the shape of a metallic cavity based on the measurement data.

Instead of possessing quicker convergency in the traditional tabu search algorithm (TSA), the

tabu list in this paper is to define the information and features of individuals of bad radiation performance and avoid unnecessary scattering simulations for them. The new tabu list embedded into GA is introduced to design low RCS antennas. The GA is applied as the main frame because of its global ability of general search. All the individuals of a new generation produced by the GA will be sent to the proposed tabu list for comparison before they are simulated in HFSS. If the geometry parameters of an individual happen to not be in the acceptable neighborhood region, which is defined according to the individuals with acceptable radiation performances, the time-consuming simulation will not be conducted in HFSS for it. Thus, the amount of individuals which need to be simulated is reduced and it leads to an efficient low RCS antenna design. Moreover, an auto-controlled calculation is programmed based on the VBScript language in HFSS.

A DGS antenna with two rectangular slots on the patch is adopted as the prototype. For the low RCS antenna design, the geometry parameters of slots and DGS are optimized to obtain satisfying radiation and scattering performances. This example validates the feasibility and efficiency of the proposed approach.

II. HYBRID OPTIMIZATION ALGORITHM

A. Tabu list

The most important feature of the traditional tabu list is to prevent the revisiting of local minima in the parameter space. The tabu list in this paper is adopted to depict the features of individuals and decide the candidates to be simulated or not for the next step. The parameter information of individuals, which have important effect on the radiation performance of antennas, is evaluated by the tabu list. Each individual gets a score determined by a criterion to judge its quality. If the score is low, which means that the individual is not similar to the feature of bad individuals, it will be sent to HFSS simulation. If the score is high, parameters of the individual incorporate more bad features and it will not take time in conducting the simulation in HFSS for it.

The tabu list with the effect of parameters is established by pre-determination from HFSS. The score for each individual is given by

$$Score = \sum_i a_i |x_i - T_i|, i = 1, 2, 3, \dots \quad (1)$$

where a_i is the scale factor, x_i is the optimized parameter, and T_i is the corresponding threshold value that judges the parameter.

The bad property of population is defined by a reference score. If the reference score is set too low, the procedure will take more individuals as bad ones, which not only skips some better individuals but also runs easily into local optimum. If the reference score is set too high, fewer individuals are considered as bad ones, which means the tabu list does not work. So the reference score is necessary to be set appropriately.

B. Optimization for low RCS antennas

Figure 1 depicts the flowchart of the whole optimization and calculation process for a low RCS antenna. The process consists of the optimization module and HFSS simulation module which includes the radiation and scattering parts. The initialized population in this approach in Fig. 1 is the randomly created chromosomes. Each chromosome coded by a binary number represents an individual prototype of an antenna structure.

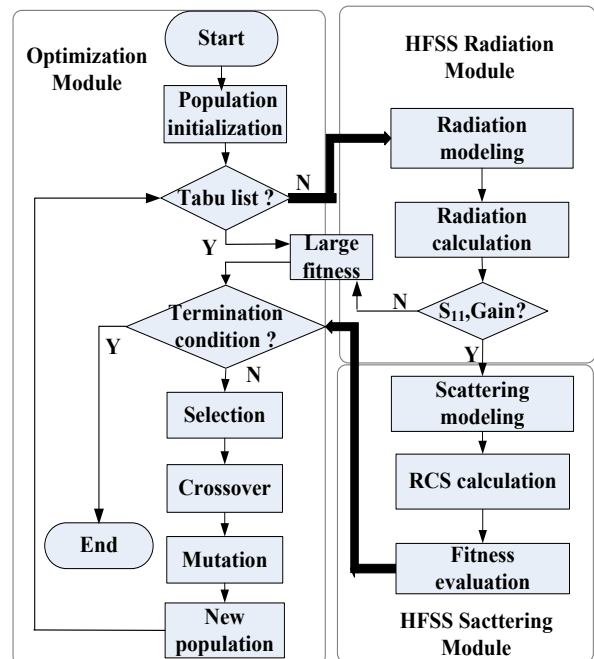


Fig. 1. Flowchart of the calculation for low RCS antenna design.

Firstly, parameters of each individual are evaluated by the tabu list. If the score is higher

than a given value, which means the individual satisfies the features of bad ones, its fitness value is set to a large number and it will not be sent to HFSS with simulation. The good individuals with small scores will be sent to be simulated in HFSS through the VBScript. Secondly, according to these parameters of good individuals, the antenna radiation models are established and calculated in HFSS. Thirdly, if the individuals meet the radiation requirements, such as S_{11} and gain conditions, their corresponding scattering models are established and fitness values are calculated. Otherwise, the fitness value is set to a large number and the scattering simulation is skipped. Thus, a waste of time to simulate scattering models of the worse individuals is avoided. Last, the fitness of each individual of the current generation is transferred to the GA and the parameters of individuals are optimized. The fitness function is defined as follows:

$$fitness = \sum_{j=1}^N \left(\frac{1}{n} \sum_{i=1}^n A_{RCS(i)} \right). \quad (2)$$

where n is the number of the RCS sample point versus frequencies, A_{RCS} is the RCS value of an individual antenna, and N represents for the different incident angles.

According to the results of the fitness evaluation, individuals are selected by the proportionate selection strategy. The selected individuals act as parents for a two-point crossover to rearrange the genes for producing better combinations of genes. Therefore, a new generation will have more fit individuals than the former one. In order to speed up the convergence of GA and reduce the time consuming of EM simulations, a certain amount of best individuals are saved and inserted into the new generation directly in the elitist strategy. Moreover, the tabu list reduces the time consuming of EM simulations, too. In order to avoid sticking at local optima, the mutation occurs with a low probability, of a value of 0.01 in this paper. After the GA produces a new generation, the individuals in the new population are evaluated by the tabu list and sent to HFSS for simulation again. The simulation and optimization are run alternatively until the termination condition is satisfied.

III. LOW RCS ANTENNA EXAMPLE

Various literatures have reported the antenna

design with DGSs. The effects of DGSs on antennas include the reduction of higher order harmonics [13], suppression of cross-polarized radiation [14], broaden impedance bandwidth [15], elimination of scan blindness [16] and mutual coupling suppression [17]. However, few literatures introduced the DGSs to the RCS reduction of antennas. In [5], a rectangular DGS is adopted to reduce the RCS at the expense of a 2.3dB gain decrease.

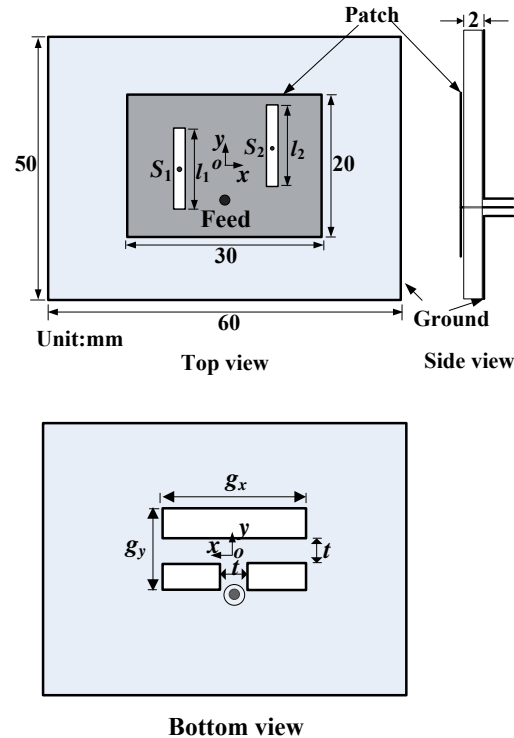


Fig. 2. Geometric structure of the optimized antenna.

In this paper, a patch antenna with a simple rectangular DGS is studied, as shown in Fig. 2. The substrate is 2mm thick RT5880 whose relative permittivity is 2.2. The distance between the coaxial probe and center of the antenna is 6.5mm along y -axis. The width of each rectangular slot on the patch is 2mm. The parameters to be optimized are the size (g_x , g_y and t) of the DGS on the ground and the slot location S_i ($i=1, 2$) and length l_i ($i=1, 2$) on the patch. A rectangular patch antenna without slots is used as a reference antenna, with a patch of $38.4 \times 24.4 \text{ mm}^2$ and a ground of $75 \times 65 \text{ mm}^2$.

Before the whole optimization process, sweeping each optimized parameter while

maintaining the other parameter constant in HFSS is needed to determine a_i and T_i in (1). As mentioned above, the tabu list is obtained with the radiation requirement, and the antenna operating frequency of 3.7GHz is considered in this example. The impact of different parameters on the operating frequency is shown in Fig. 3. So, a_i is appropriately determined by the slope of each curve, and T_i is appropriately the value corresponding to 3.7GHz for each curve, respectively. It is obvious that the slopes of g_x and g_y are the same and larger than those of l_1 and l_2 . Therefore, a_i corresponding to g_x, g_y, l_1 and l_2 are set to 3, 3, 2 and 2, respectively. T_i can be determined as 17.5, 12.5, 12.5 and 12.5 by the intersection points of the dotted line ($f=3.7\text{GHz}$) and curves, respectively. An appropriate tabu list is shown in Table 1 through the pre-determination from HFSS.

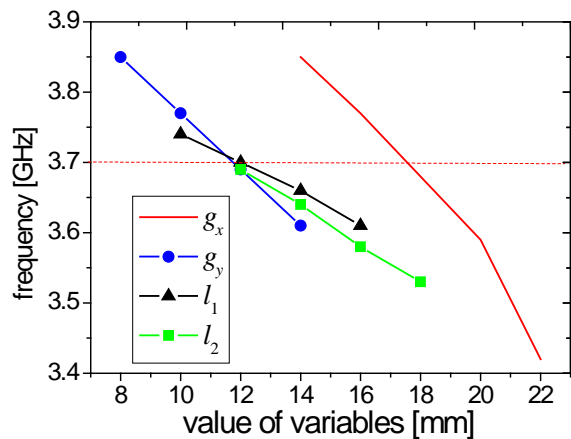


Fig. 3. Effect of the key parameters.

Table 1. Information of the tabu list

	g_x	g_y	l_1	l_2
a	3	3	2	2
$T(\text{mm})$	17.5	12.5	12.5	12.5

A population incorporates 40 individuals and the maximal iteration of generation is 10. The acceptable radiation performance in Fig. 1 is set as $S_{11} < -15\text{dB}$ and gain > 7 dB, respectively. Besides, the best 10% individuals of population have been considered as the elitists. In this numerical example, the reference score is set to 83. Due to the reference score, about 20% individuals in the population for each generation have been considered as the bad ones and they are

unnecessary to be simulated in HFSS. Thus, the tabu list reduces the amount of 20% calls of the time-consuming EM solver to improve the optimization efficiency. Figure 4 shows the convergence for RCS reduction of the GA program, which consists of the average and minimum values of average RCS of different incident angles for each generation. The optimization results are listed in Table 2.

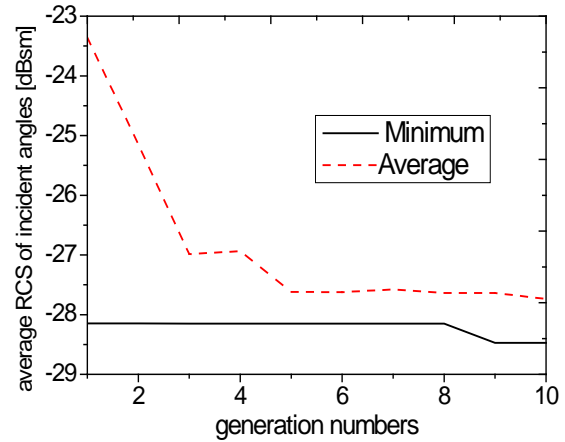


Fig. 4. Convergence for RCS reduction of the GA.

Table 2. Geometry of the optimized antenna (unit: mm)

Patch	Location(x, y)		l
	S_1	S_2	
Ground	g_x	g_y	t
	15	8	2

Figure 5 depicts the return loss of the optimized antenna and reference antenna. Both their resonant frequencies are 3.7GHz. Compared with the reference antenna, the impedance bandwidth ($S_{11} < -10$) of the optimized antenna doesn't decrease. Both the xoz -plane and the $yo z$ -plane radiation patterns of the antennas at the resonant frequency are shown in Fig. 6. It can be observed that the gains of the optimized antenna decreases from 8.4 to 7.3dB when $\theta = 0^\circ$. The reduction of 1.1dB is mainly because the DGS loses some radiation energy in the backward direction.

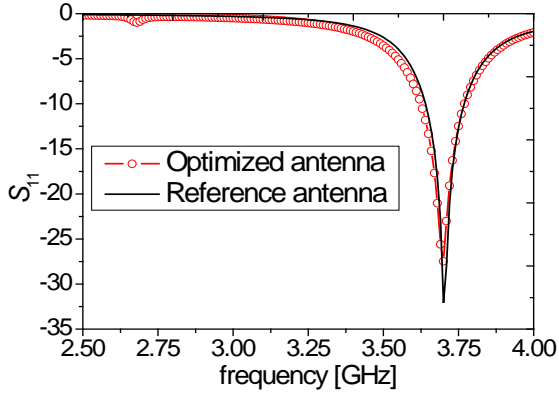
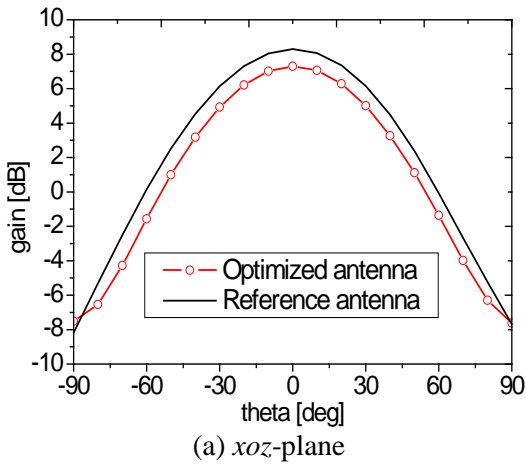
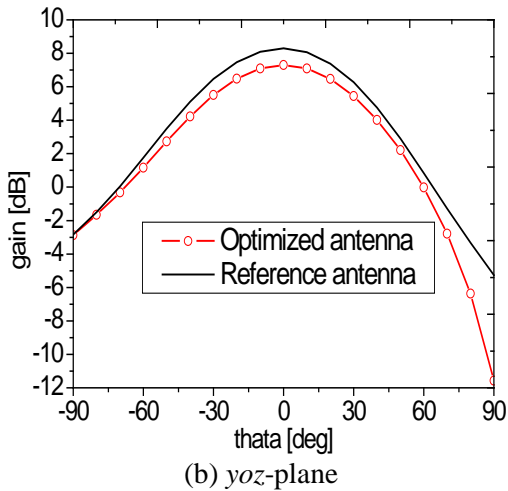


Fig. 5. S_{11} of the reference and optimized antennas.



(a) xoz -plane

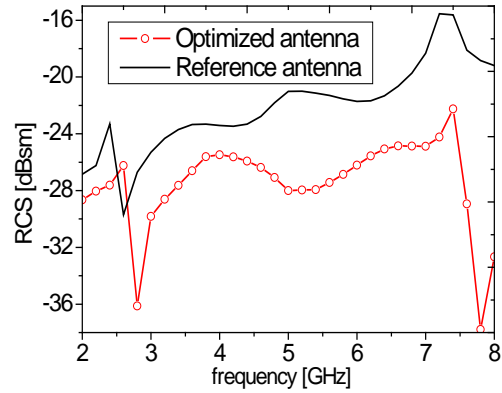


(b) yo z -plane

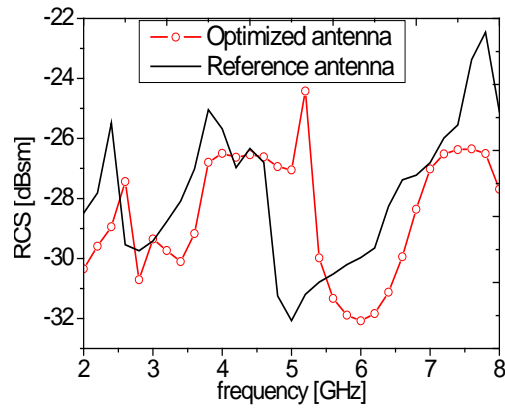
Fig. 6. Simulated radiation patterns of the reference and optimized antennas at 3.7 GHz.

The comparisons of RCS versus frequency between the optimized antenna and reference antenna for different incident angles are shown in Fig. 7. The incident plane wave is with the θ polarization. As shown in Fig. 7, the monostatic

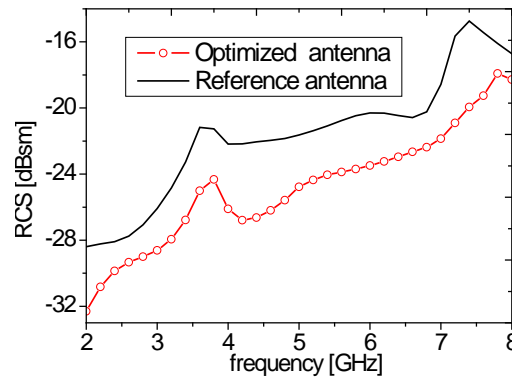
RCS of the optimized antenna is reduced in the frequency range of 2-8 GHz.



(a) Incident angle ($\theta = 60^\circ, \varphi = 0^\circ$)



(b) Incident angle ($\theta = 60^\circ, \varphi = 45^\circ$)



(c) Incident angle ($\theta = 60^\circ, \varphi = 90^\circ$)

Fig. 7. Simulated RCS of the reference and optimized antennas.

In [5], the proposed antenna with DGS does not obtain the marked RCS reduction compared to a reference patch antenna. The proposed DGS antenna in this paper gets a remarkable RCS

reduction compared to its reference patch antenna from Fig. 7.

IV. CONCLUSION

This paper proposes a simple and efficient approach that combines the GA/tabu list optimizer with HFSS to design low RCS patch antennas. The tabu list eliminates some bad individuals of the population and reduces time consuming. In addition, the proportionate selection together with the elitist model for the selection strategy and the two-point crossover accelerate the convergence of the GA. The data exchange between the optimization module and simulation module is realized automatically by VBScript language. The results show that the convergence of the program is fast and the optimized antenna achieves the obvious RCS reduction in a broad frequency range from 2 to 8 GHz at different incident angles, while it maintains good radiation performances.

ACKNOWLEDGMENT

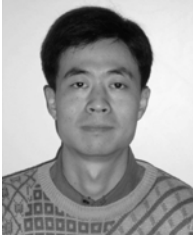
This work was supported in part by the NCET Foundation (11-0065), the Natural Science Foundation of China (60901023), and the Fundamental Research Funds for the Central Universities (ZYGX2010J043).

REFERENCES

- [1] E. F. Knot, J. F. Sbaeffer and M. T. Tuley, *Radar Cross Section*, 2nd ed. Artech House, London, 1993.
- [2] W. Jiang, Y. Liu, S. X. Gong, and T. Hong, "Application of Bionics in Antenna Radar Cross Section Reduction," *IEEE Antennas Wireless Propag. Lett.*, vol. 8, pp. 1275-1278, 2009.
- [3] R. Kumar and P. Malathi, "Design of CPW-Fed Ultra Wideband Fractal Antenna and Backscattering Reduction," *Journal of Microw., Optoelectronics Electromag. Applications*, vol. 9, no. 1, pp. 10-19, 2010.
- [4] L.-S. Ren, Y.-C. Jiao, J.-J. Zhao, and F. Li, "RCS Reduction for a FSS-Backed Reflectarray using a Ring Element," *Progress In Electromagnetics Research*, vol. 26, pp. 115-123, 2011.
- [5] S.-C. Zhao, B.-Z. Wang and Q.-Q. He, "Broadband Cross Section Reduction of a Rectangular Patch Antenna," *Progress In Electromagnetics Research*, vol. 79, pp. 263-275, 2008.
- [6] Y. R.-Samii and E. Michielssen. *Electromagnetic Optimization by Genetic Algorithms*, John Wiley & Sons, New York, 1999.
- [7] R. L. Haupt, "An Introduction to Genetic Algorithms for Electromagnetics," *IEEE Antennas and Propagation Magazine*, vol. 37, no. 2, pp. 7-13, 1995.
- [8] H. Mosallaei and Y. R. Samii, "RCS Reduction of Canonical Targets using Genetic Algorithm Synthesized RAM," *IEEE Trans. Antennas Propag.*, vol. AP-48, no. 10, pp. 1594-1606, 2000.
- [9] H.-T. Chen, G.-Q. Zhu, and S.-Y. He, "Using Genetic Algorithm to Reduce the Radar Cross Section of Three-Dimensional Anisotropic Impedance Object," *Progress In Electromagnetics Research B*, vol. 9, pp. 231-248, 2008.
- [10] W. Wang, S. Gong, X. Wang, Y. Guan and W. Jiang, "Differential Evolution Algorithm and Method of Moments for the Design of Low-RCS Antenna," *IEEE Antennas Wireless Propag. Lett.*, vol. 9, pp. 295-298, 2010.
- [11] X. Zhu, W. Shao, J.-L. Li, and Y. Dong, "Design and Optimization Low RCS Patch Antenna Based on GA," *Progress In Electromagnetics Research*, vol. 122, pp. 327-339, 2012.
- [12] Y. Zhou, J. Li, and H. Ling, "Shape Inversion of Metallic Cavities using Hybrid Genetic Algorithm Combined with Tabu List," *Electronics Letters*, vol. 39, no. 3, pp. 280-281, 2003.
- [13] Y. J. Sung, M. Kim, and Y. S. Kim, "Harmonics Reduction with Defected Ground Structure for a Microstrip Patch Antenna," *IEEE Antennas Wireless Propag. Lett.*, vol. 2, pp. 111-113, 2003.
- [14] D. Guha, C. Kumar, and S. Pal, "Improved Cross-Polarization Characteristics of Circular Microstrip Antenna Employing Arc-Shaped Defected Ground Structure (DGS)," *IEEE Antennas Wireless Propag. Lett.*, vol. 8, pp. 1367-1369, 2009.
- [15] K. H. Chiang and K. W. Tam, "Microstrip Monopole Antenna with Enhanced Bandwidth using Defected Ground Structure," *IEEE Antennas Wireless Propag. Lett.*, vol. 7, pp. 532-535, 2008.
- [16] D. B. Hou and S. Xiao, "Elimination of Scan Blindness with Compact Defected Ground Structures in Microstrip Phased Array," *IET Microw. Antennas Propag.*, vol. 3, pp. 269-275, 2009.
- [17] S. Xiao and M. C. Tang, "Mutual Coupling Suppression in Microstrip Array using Defected Ground Structure," *IET Microw. Antennas Propag.*, vol. 5, pp. 1488-1494, 2011.



Xinyue Zhu received the B. E. degree in Henan Polytechnic University, Jiaozuo, China, in 2009. From 2009 to now, he is pursuing the M. Sc. degree in the Institute of Applied Physics at the University of Electronic Science and Technology of China (UESTC), Chengdu, China. His current research interests include the antenna design and optimization method.



Wei Shao received the M. Sc. and Ph. D. degrees in Radio Physics from UESTC, Chengdu, China, in 2004 and 2006, respectively. He joined the UESTC and is now an associate professor. He has been a Visiting Scholar in the Electromagnetic Communication Laboratory, Pennsylvania State University in 2010. His research interests include the computational electromagnetics and antenna technique.



Jia-Lin Li received the M. Sc. degree from UESTC, Chengdu, China, in 2004, and the Ph. D. degree from the City University of Hong Kong, Hong Kong, in 2009, both in Electronic Engineering. Since Sept. 2009, he has been with the Institute of Applied Physics, School of Physical Electronics, UESTC, where he is currently a Professor. His research interests include the high performance antennas, circuits and systems.

A Novel Dual Narrow Band-Notched CPW-Fed UWB Slot Antenna with Parasitic Strips

Xiao-Liang Ma, Wei Shao, and Guo-Qiang He

Institute of Applied Physics
University of Electronic Science and Technology of China, Chengdu, 610054, China
maxiaol2003@sohu.com, weishao@uestc.edu.cn, guoqianghe22@gmail.com

Abstract — A novel and compact 5.2/5.8GHz dual narrow band-notched ultra wideband (UWB) slot antenna with inverted U-shaped parasitic strips is presented. The band notches of this antenna fed by a coplanar waveguide (CPW) are realized by two pairs of inverted U-shaped parasitic strips. Each pair consists of two separate strips which are similar and close to each other. And dual narrow rejected properties in the lower WLAN band (5.15-5.35GHz) and upper WLAN band (5.725-5.825GHz) are obtained. The size of the proposed antenna is $24 \times 24 \times 1 \text{ mm}^3$. The simulated and measured results show that the antenna design exhibits an operating bandwidth (VSWR < 2) from 2.8 to 12 GHz excluding the rejected bands.

Index Terms — Coplanar waveguide fed, dual band notches, microstrip slot antenna, ultra wideband.

I. INTRODUCTION

Since the Federal Communications Commission (FCC) approved the frequency band from 3.1 to 10.6 GHz for the commercial use of ultra wideband (UWB) systems, much attention has been paid to the UWB technology [1-3]. It is reported that there are many practical applications in UWB communication, UWB pulse radar [4], UWB imaging [5], UWB electromagnetic pulse weapon and so on.

However, there are some other existing narrow band services in the UWB band, such as the WiMAX band (3.3-3.7GHz) and WLAN band (5.15-5.35GHz and 5.725-5.825GHz). Most band-notched designs only use a rejected band to notch the whole WLAN band [6]. Therefore, the resource of the band (5.35-5.725GHz) is wasted,

and the useful information contained in the band is also lost.

In recent years, some UWB antennas with 5.2/5.8GHz narrow band notches are proposed. In [7], the authors embed a slot in the ground and etch another slot in the radiation patch to get 5.2/5.8GHz notched bands. In [8], by adding a pair of open-circuit stubs at the edge of the slot and etching one complementary split-ring resonator (CSRR) inside a circular exciting stub on the front side, dual notched band characteristic is realized. In [9-10], by embedding two split ring resonators (SRRs) close to each other, dual narrow band notches are obtained. However, it is often difficult to carry out the antenna design works.

In this paper, a new and simple method is proposed to get two adjacent narrow stopbands. With two pairs of parasitic strips on the backside of the antenna, two narrow band notches can be obtained. Because of the mutual coupling of the two notched structures, the reject characteristic between the two stopbands becomes weakened, and a passband between the two stop bands is realized. A novel and compact CPW-fed UWB slot antenna with 5.2/5.8GHz dual band notches obtained by adding two pairs of inverted U-shaped parasitic strips is designed.

The proposed antenna has a symmetrical structure which improves the antenna radiation pattern characteristics. Because of the simple reject structure, it is easy to tune for the notched antenna. And the simulated and measured results verify the proposed method.

II. ANTENNA DESIGN

Figures 1 and 2 show the geometry and the fabrication of the proposed antenna, respectively.

The antenna, which occupies a compact area of $W \times L$, is built on an FR4 substrate with a relative permittivity of 4.4, a thickness of h and a loss tangent of 0.02, and is fed by a 50Ω CPW transmission line with a strip width of W_1 and gap width of d_1 . An SMA connector is connected to the port of the feeding line. The original antenna structure without band-notched structures consists of a circle-like exciting stub and a slotted CPW ground.

In order to obtain two narrow stopbands and not to take up too much space, two similar pairs of inverted U-shaped parasitic strips are introduced on the backside of the antenna. The total length of each parasitic strip is the corresponding half wavelength to the center frequency of each notched band.

The required notched bands are 5.15-5.35GHz and 5.725-5.825GHz, therefore, the designed resonant frequencies are set to be about 5.25 and 5.8GHz. The wavelengths can be calculated by [11]

$$\lambda = \frac{c}{f \sqrt{\epsilon_{\text{eff}}}} \quad (1)$$

$$\epsilon_{\text{eff}} = \frac{1 + \epsilon_r}{2} \quad (2)$$

where c is the speed of the light, ϵ_{eff} is the effective dielectric constant, ϵ_r is the relative permittivity of the antenna substrate, and f is the designed resonant frequency. The corresponding length of the parasitic strips can be obtained by

$$L_{\text{strip_outer}} = 2 \times L_6 + W_3 \approx \frac{\lambda_{\text{low}}}{2} \quad (3)$$

$$L_{\text{strip_inner}} = 2 \times L_5 + W_2 \approx \frac{\lambda_{\text{high}}}{2} \quad (4)$$

where $L_{\text{strip_outer}}$ and $L_{\text{strip_inner}}$ are the total length of the outer and inner inverted U-shaped parasitic strips, respectively. And λ_{low} and λ_{high} are the wavelengths corresponding to the center frequency of the low and high notched band, respectively.

Through electromagnetic simulations, it can be found that the edge of slot is related to broadband impedance matching. Thus, the rejecting structures are away from the edge of the slot, and the dual narrow band-notched properties are obtained. The optimized parameters are listed as follows: $R_1 = 11.4$ mm, $R_2 = 6.8$ mm, $L = 24$ mm, $L_1 = 4$ mm,

$L_2 = 3.5$ mm, $L_3 = 1.5$ mm, $L_4 = 4$ mm, $L_5 = 7$ mm, $L_6 = 7.4$ mm, $L_7 = 7.4$ mm, $L_8 = 7.6$ mm, $W = 24$ mm, $W_1 = 3.6$ mm, $W_2 = 1.9$ mm, $W_3 = 3.3$ mm, $W_4 = 7.55$ mm, $d = 1$ mm, $d_1 = 0.4$ mm, $d_2 = 0.2$ mm, and $h = 1$ mm.

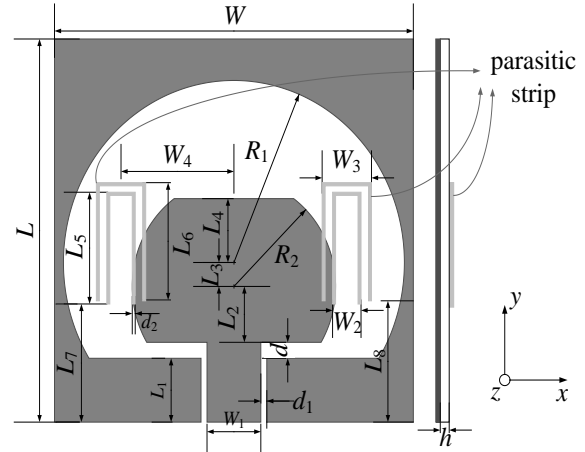


Fig. 1. Geometry of the proposed antenna.

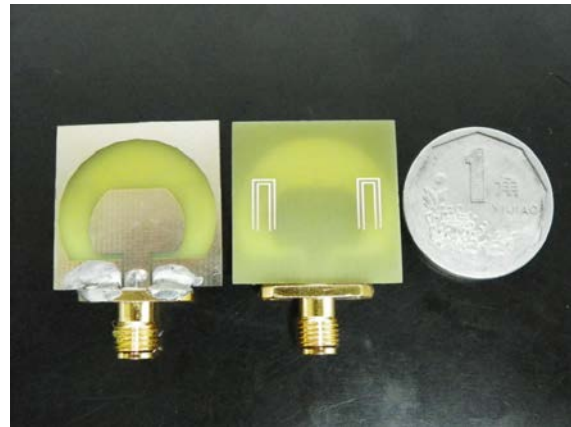


Fig. 2. Photograph of the proposed antenna.

III. RESULTS AND DISCUSSION

The VSWR results of the proposed antenna are simulated with HFSS software and measured with an Agilent E8363 network analyzer, respectively, as shown in Fig. 3. For comparison, the simulation VSWR result of the original UWB antenna without parasitic strips is also provided in Fig. 3.

The proposed antenna exhibits a bandwidth (VSWR < 2) from 2.8 to 12GHz, rejecting the 4.8-5.36GHz and 5.68-6.2GHz bands. The measured result of the proposed antenna is almost in accord with the simulated one except a little frequency offset. The difference between simulation and

measurement is mostly due to the influences of manufactured precision and feeding cable. Obviously, it can be found that a wider passband between the two notched bands is obtained both in the simulated and measured results, which verify the proposed theory that a passband between two adjacent stopbands can be obtained because of the mutual coupling of the two notched structures.

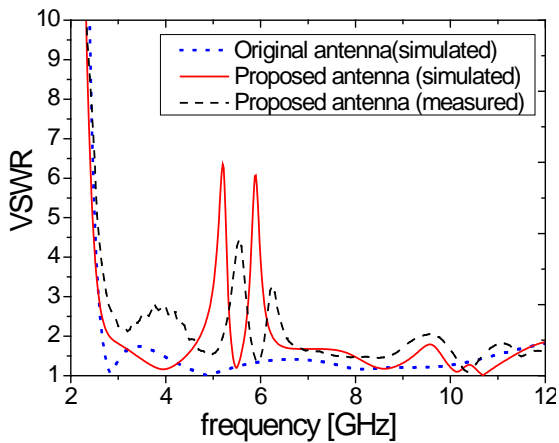


Fig. 3. Simulated and measured VSWR of the two antennas.

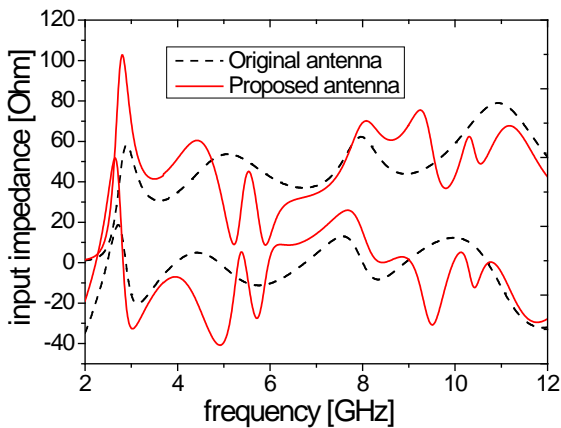


Fig. 4. Simulated input impedance of the two antennas.

Figure 4 shows the simulated input impedance of the two antennas. We can see that when the reject structures are added in the original antenna, the input impedance of the proposed antenna mismatches in the designed reject bands, but it matches in the other bands, especially the band between the two reject bands. Therefore, the proposed antenna cannot work well in the reject bands, and it does not disturb the reject band communication.

It is known that the frequency of the notched band is determined by the length of the notched structure. With the change of the parameters L_5 and L_6 , the total lengths of the two notched structures are also changed. Therefore, the frequency responses with the various parameters L_5 and L_6 are simulated, respectively, shown in Figs. 5 and 6.

In Figs. 5 and 6, we can see that L_5 and L_6 mainly affect the central frequency of the higher band notch at 5.8GHz and the lower band notch at 5.2GHz, respectively. It is seen that the larger L_5 or L_6 becomes, the smaller the corresponding central frequency of the band notch becomes. Besides, it is also suggested that the two band notches should be independent of each other.

Surely, the range in which the notched frequencies are adjusted cannot exceed the working band of the original antenna.

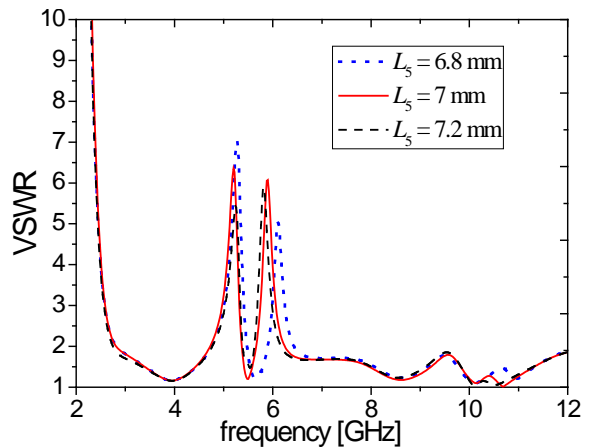


Fig. 5. Simulated VSWR with various L_5 .

The parasitic strips can also change the surface current distributions. The current direction on the reject structures is opposite to that on the nearby antenna structure, so the far fields produced by the currents on the reject structures and nearby antenna structure cancel out each other in the reject band. Fig. 7 shows the simulated current distributions at 5.2, 5.8 and 5.6GHz on the antenna backside. In Fig. 7(a), the current mainly flows around the outer inverted U-shaped strips, which destructs the radiation of the original antenna at this band and results in the lower stopband. On the contrary, the current mainly flows around the inner inverted U-shaped strips in Fig. 7(b). In Fig.7(c), the current distribution at 5.6GHz is even on the outer and inner inverted U-shaped strips, but the

current direction on the inner strips is opposite to that on the outer ones. It is suggested that two band notches should be mutually interfered with and the notched property does not have any influence on the antenna radiation at 5.6GHz. Then, a passband between two adjacent stopbands can be obtained because of the mutual interference of the two notched structures.

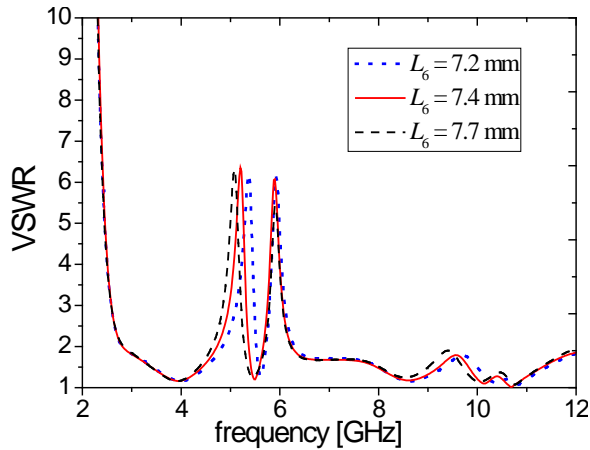


Fig. 6. Simulated VSWR with various L_6 .

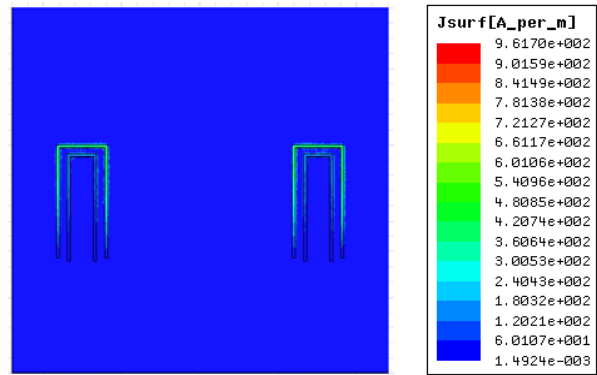
Figure 8 depicts simulated radiation patterns at 2.8, 3.5, 7, 9 and 12GHz on yoz -plane and xoz -plane. A nearly omnidirectional radiation pattern can be observed on xoz -plane over the whole UWB frequency range, especially at the low frequencies. The radiation patterns on the yoz -plane are like a small electric dipole leading to bidirectional patterns in a very wide frequency band. With the increase of frequency, the radiation patterns become worse because of the increasing effects of the cross polarization.

Simulated peak gain and radiation efficiency of antennas with strips and without strips are shown in Figs. 9 and 10, respectively. The sharp decreases of the gain and radiation efficiency of the proposed antenna occur in the lower and upper WLAN bands. It is suggested from the two figures that the radiation of the proposed antenna be bad at the reject bands. At the same time, the high radiation efficiency in the band between the two reject bands leads to a passband.

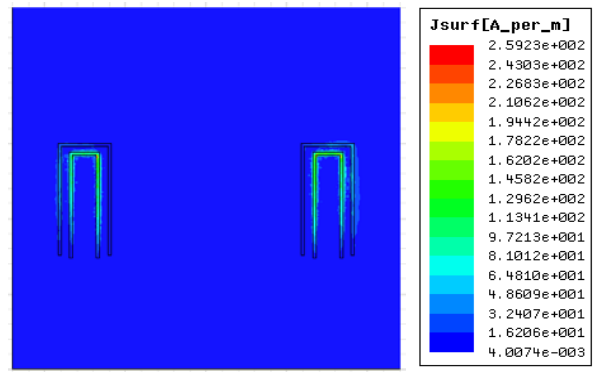
IV. CONCLUSION

A novel and compact CPW-fed UWB slot antenna with 5.2/5.8GHz dual band notches obtained by adding inverted U-shaped parasitic

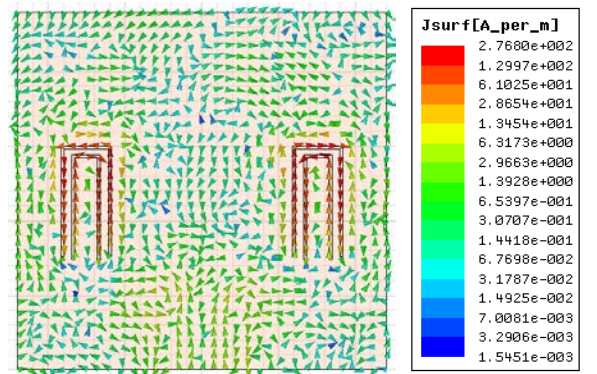
strips is proposed and discussed in detail in this paper. A good dual narrow band-notched characteristic is obtained with two pairs of similar inverted U-shaped parasitic strips in the symmetric position of the antenna. The proposed antenna has stable gain and good omnidirectional radiation patterns in the H-plane over the whole frequency band of interest.



(a) 5.2 GHz



(b) 5.8 GHz



(c) 5.6 GHz

Fig. 7. Simulated current distributions.

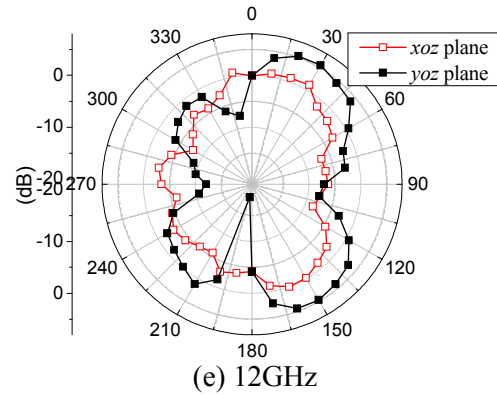
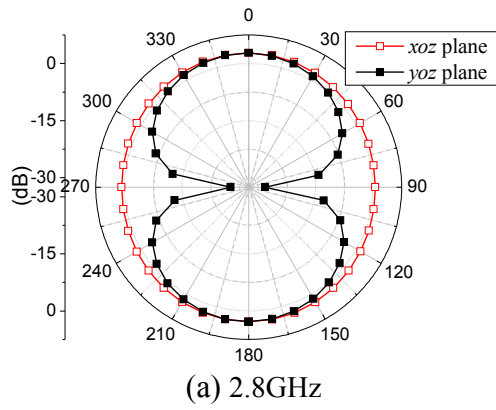


Fig. 8. Simulated radiation patterns on yoz -plane and xoz -plane for the proposed antenna.

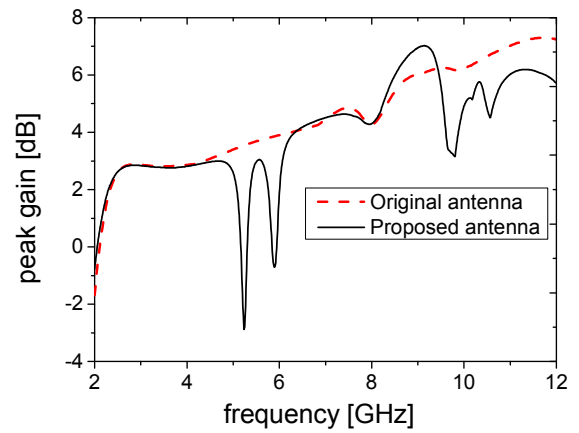
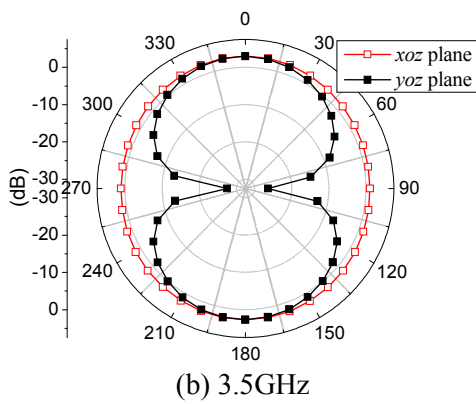


Fig. 9. Simulated peak gain of the two antennas.

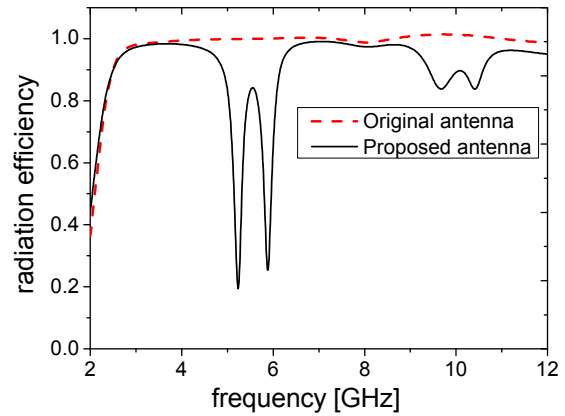
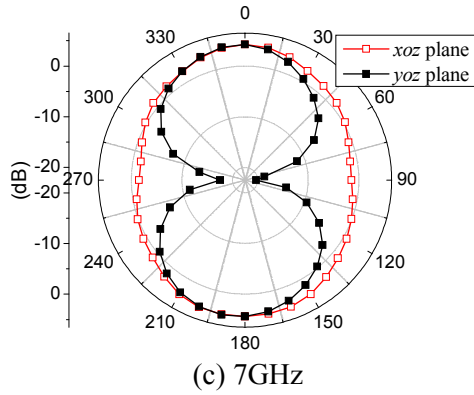
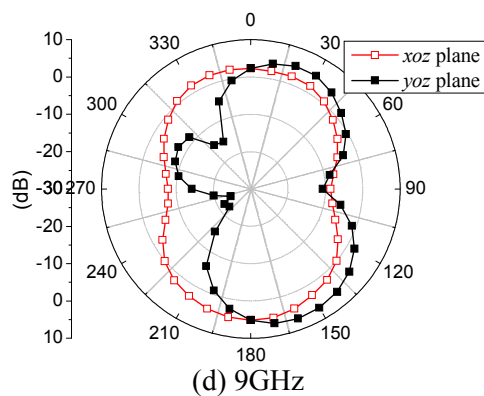


Fig. 10. Simulated radiation efficiency of the two antennas.

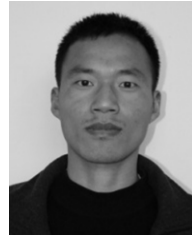


ACKNOWLEDGMENT

This work is supported by the National Natural Science Foundation of China (60901023), the NCET Foundation (11-0065) and the Fundamental Research Funds for the Central Universities (ZYGX2010J043).

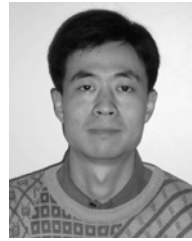
REFERENCES

- [1] M. N.-Jahromi, and N. K.-Barchloui, "Analysis of the Behavior of Sierpinski Carpet Monopole Antenna," *Applied Computational Electromagnetics Society (ACES) Journal*, vol. 24, no. 1, pp. 32-36, Feb. 2009.
- [2] D. S. Javan, and O. H. Ghouchani, "Cross Slot Antenna with U-shaped Tuning Stub for Ultra Wideband Applications," *Applied Computational Electromagnetics Society (ACES) Journal*, vol. 24, no. 4, pp. 427-432, Aug. 2009.
- [3] R. Azim, M. T. Islam, and N. Misran, "Design of a Planar UWB Antenna with New Band Enhancement Technique," *Applied Computational Electromagnetics Society (ACES) Journal*, vol. 26, no. 10, pp. 856-862, Oct. 2011.
- [4] R. Xu, Y. L. Jin, and C. Nguyen, "Power-Efficient Switching-Based CMOS UWB Transmitters for UWB Communications and Radar Systems," *IEEE Trans. Microwave Theory Tech.*, vol. 54, no. 8, pp. 3271-3277, Aug. 2006.
- [5] T. Sakamoto and T. Sato, "Code-Division Multiple Transmission for High-Speed UWB Radar Imaging with an Antenna Array," *IEEE Trans. Geosci. Remote Sens.*, vol. 47, no. 4, pp. 1179-1186, Apr. 2009.
- [6] J. William and R. Nakkeeran, "A New UWB Slot Antenna with Rejection of WiMAX and WLAN Bands," *Applied Computational Electromagnetics Society (ACES) Journal*, vol. 25, no. 9, pp. 787-793, Sep. 2010.
- [7] X. J. Liao, H. C. Yang, N. Han, and Y. Li, "UWB Antenna with Dual Narrow Band Notches for Lower and Upper WLAN Bands," *Electron. Lett.*, vol. 46, no. 24, pp. 1593-1594, Nov. 2010.
- [8] X. J. Liao, H. C. Yang, N. Han, and Y. Li, "Aperture UWB Antenna with Triple Band-Notched Characteristics," *Electron. Lett.*, vol. 47, no. 2, pp. 77-79, Jan. 2011.
- [9] L. Li, Z. L. Zhou, J. S. Hong, and B. Z. Wang, "Compact Dual-Band-Notched UWB Planar Monopole Antenna with Modified SRR," *Electron. Lett.*, vol. 47, no. 17, pp. 950-951, Aug. 2011.
- [10] M. C. Tang, S. Q. Xiao, T. W. Deng, D. Wang, J. Guan, B. Z. Wang, and G. D. Ge, "Compact UWB Antenna with Multiple Band-Notches for WiMAX and WLAN," *IEEE Trans. Antennas Propag.*, vol. 59, no. 4, pp. 1372-1376, April 2011.
- [11] Z. A. Zheng, Q. X. Chu, and Z. H. Tu, "Compact Band-Rejected Ultrawideband Slot Antennas Inserting with $\lambda/2$ and $\lambda/4$ Resonators," *IEEE Trans. Antennas Propag.*, vol. 59, no. 2, pp. 390-397, Feb. 2011.



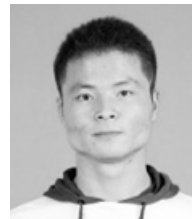
interest is the antenna theory and design.

Xiao-Liang Ma received the B. E. degree in Electrical Engineering from the University of Electronic Science and Technology of China (UESTC), Chengdu, China, in 2010. From 2010 to now, he is pursuing the M. Sc. degree at UESTC. His current research



Electromagnetic Communication Laboratory, Pennsylvania State University in 2010. His research interests include the computational electromagnetics, EMC design and antenna technique.

Wei Shao received the M. Sc. degree and Ph. D. degrees in Radio Physics from UESTC, Chengdu, China, in 2004 and 2006, respectively. He joined the UESTC in 2007 and is now an associate professor there. He has been a Visiting Scholar in the



electromagnetics, optimization techniques and antenna design.

Guo-Qiang He received the B. E. degree in Electrical Engineering from UESTC, Cheng du, China, in 2010. From 2010 to now, he is pursuing the M. Sc. degree in the Institute of Applied Physics at UESTC. His current research interests include computational

Application of Inductive Loadings for the Dual and Broad Banding of CPW-Fed Ring Antennas

H. Oraizi¹ and B. Rezaei²

¹Department of Electrical Engineering
Iran University of Science and Technology, Tehran, State Code Zip Code, Iran
h_oraizi@iust.ac.ir

²Department of Electrical Engineering
Iran University of Science and Technology, Tehran, State Code Zip Code, Iran
b.rezaei.iust@gmail.com

Abstract — The broad banding of a printed ring antenna is achieved through inductive loadings by open-circuited radial line sections distributed around its periphery. The bandwidth of the stub loaded ring antenna is significantly enhanced without minor degradation of its radiation patterns, which may be realized by the appropriate design of widths, lengths, and angular spacings of open circuited radial lines. Dual-band performance can also be obtained by the application of the proposed method. The proposed antenna configuration is verified by computer simulation together with fabrication and measurement.

Index Terms — CPW-fed ring antenna, dual-band antenna, ring antenna, stub loadings, wideband antenna.

I. INTRODUCTION

Printed antennas having low profiles and high compatibility of integration with other circuit elements usually find applications in wireless communication systems. However, they suffer from the disadvantages of low gain and narrow bandwidths, which limit their applications [1]. In this paper, a technique is presented to transform a single-band antenna into dual-band and wideband antennas. In this technique, the radiating edges of antennas are loaded by some stubs, which produce parallel inductances. Open- and short-circuited stubs may be used for the generation of inductive loadings. However, such a device requires a

ground plane under the patch. The ground plane here does not extend under the proposed ring antenna. Consequently, we use such inductive in our antenna loadings. Now, we may make the radiating structure wideband by making it first to operate in a dual-band condition and then by controlling its second resonance frequency through taking it closer to the first one. The proposed structure for producing dual- and wide band operations has the advantages of being planar and compact as compared with other configurations, such as slot loaded [2-6] and stacked patch antennas [7].

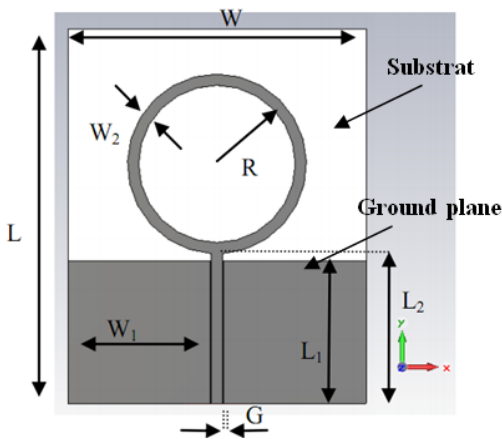
In Section 2, the analysis and design of a simple resonant ring antenna is described. In Section 3, the ring antenna is loaded by radial stubs, which is designed for dual-band operation. It is shown that it operates at integral multiples of its fundamental frequency. A parametric study and variation of its geometrical dimensions, may lead to its dual-band operation and eventual wideband performance. The return loss bandwidth of 80% has been achieved in the S band (2~4GHz) and higher frequencies. Two prototype models of the proposed antennas have been fabricated and measured, which verify their effectiveness.

II. ANALYSIS OF THE PRINTED RING ANTENNA

The proposed antenna design technique is illustrated by a CPW-fed ring antenna, which may be excited by a resonant or non-resonant mode. We adopt the resonant mode. The circumference

of the ring should be equal to the effective wavelength at the resonance frequency [8-10]. In this case, the current distributions on the antenna consist of two equiphase components, which generate its broadside radiation. The antenna feed may be in the form of microstrip line, coplanar waveguide (CPW) or a coaxial probe-feed. The CPW feed is selected, which may provide capability for assembly of components and integration with other components. As shown in Fig. 1, the characteristic impedance is 50 ohms, the width of the ring strip and feed line are taken equal. The substrate FR4 is selected, with $\epsilon_r=4.9$, thickness $h=7.87\text{mm}$ and loss tangent of 0.025.

The antenna behavior is analyzed by the CST simulation software. Its response as the reflection coefficient versus frequency is drawn in Fig. 2 and its radiation patterns are drawn in Fig. 3. Since there is no ground plane, the patterns of the antenna are identical on its both sides. The bandwidth is defined as the frequency interval where the reflection coefficient is less than -10dB. The return loss bandwidth at the center frequency of 2.55GHz is about 35%, where its simulated gain is about 1.1 dBi at 3GHz. Observe that the antenna has almost omnidirectional radiation pattern in the X-Z plane, as shown in Fig. 3. The optimum length of the CPW line (L_1) should be selected for the best input impedance matching.



W	W ₁	W ₂	L	L ₁	L ₂	G	R
32	15.4	0.63	40	14.2	15	0.18	10

Fig. 1. CPW ring antenna (dimensions are in millimeters).

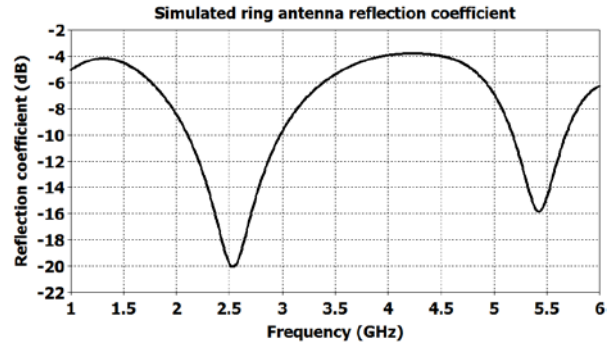


Fig. 2. CPW ring antenna reflection coefficient.

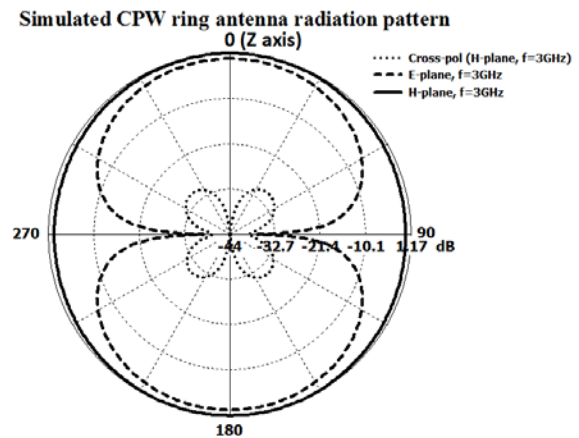


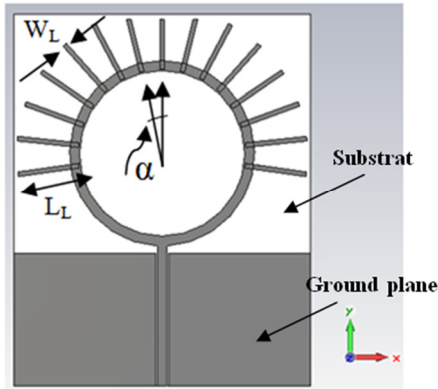
Fig. 3. CPW ring antenna radiation pattern at 3GHz. (dashed) E-plane (y-z plane); (solid) H-plane (x-z plane); (dotted) cross-polar (H-plane).

III. ANALYSIS OF THE INDUCTIVELY LOADED RING ANTENNA

The radial stubs are placed on the periphery of the ring, which produce an inductive loading. The number of stubs, their lengths, widths and angular spacings may be considered as parameters, which provide as many degrees of freedom for the antenna design. The implementation of the proposed technique on the ring antenna is shown in Fig. 4. The dimensions of the main structure are the same as in Fig. 1.

The reflection coefficient of the ring with inductive loading is drawn in Fig. 5, which shows that the radial stubs make the antenna resonate at two frequency bands. The return loss bandwidth at the center frequency 2.55GHz is about 60% and that at 4.75GHz is about 12%. Also, its performance in the first band has improved. Figures 2 and 5 show that the two ring antennas (with and without radial stubs) are both dual-band. However, observe that the second band of

antenna1 (shown in Fig. 2) is due to its resonance nature, whereas the second band in antenna2 are somewhat displaced from its natural resonance frequency.



W	W ₁	W ₂	L	L ₁	L ₂
32	15.4	0.63	40	14.2	15
G	R	W _L	L _L	α	N
0.18	10	0.5	6	14°	15

Fig. 4. Loaded CPW ring antenna2 (dimensions are in millimeters).

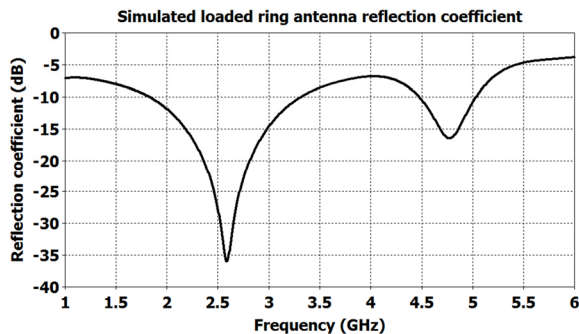


Fig. 5. Loaded CPW ring antenna2 reflection coefficient.

A parametric study and simulation of the antenna design parameters (namely the lengths, widths, angular spacings, and number of stubs) are performed and its results are indicated in Fig. 6. The stub widths are selected as narrow as possible (to provide higher inductive effects), which are restricted by our available photolithography technology and achievement of reasonable strength. The computer simulation results show that as the stub widths increase, the second band gradually approaches the first band, as shown in Fig. 6 (a). Therefore, the variation of this

parameter may lead to the broad banding of the antenna. The second resonance frequency may be highly changed by varying the lengths of the stubs, but the first resonance frequency remains relatively constant by their variations. This phenomenon is shown in Fig. 6 (b). The number of stubs and their angular spacings affect the improvement of the antenna return loss and its wideband performance. Therefore, it may be inferred that by the proposed method, the second resonance frequency may be controlled to design a dual-band or a wideband antenna.

The current distribution may reveal the effect of antenna design parameters on its performance. The current distributions on the simple and loaded ring antenna are shown in Fig. 7 at two frequency bands. Observe that the stubs have practically no effect on the first band, but generate a new current distribution in the second band. Four different current distributions appear on the four quadrants of the ring, in such a way that the current distribution on the upper half semicircle is in phase with that on the lower one. They effectively give rise to broadside radiation. The opposite stubs with anti-phase current distributions cancel the effect of each other. Minor current distributions appear on the stubs at the lower frequency band, because their lengths are relatively short and their inductive effect is negligible. In the second upper frequency band, as shown in Fig. 7 (c, d), the current distributions are quite intensive on the stubs. They enforce each other, because they are codirectional. This is a useful property, because shorter stubs may be used for antenna miniaturization. Furthermore, such current distributions on stubs produce relatively strong magnetic fields and energy around the stubs, leading to high inductive loadings of antenna. However, the stubs have negligible capacitive effect, due to the absence of a ground plane under them and their thin thicknesses and relatively wide spacings.

Symmetrical placement of stubs on the ring antenna edges to effective cancellation of cross-polarized radiation fields, as shown in Fig. 7 (d). The x-directed current component on combine stubs on the two sides of ring antenna are in opposite directions, and consequently cancel the effects of each other, which is the cause of cross-polarized radiation. For the verification of this effect, refer to the co-polar and cross-polar

radiation patterns of the stub loaded ring antenna. Consequently, we may conclude from the above results that the proposed stub loading of the ring antenna is quite effective in making a dual-band antenna from a single-band one and also the second resonance frequency may be readily adjusted. Such an antenna may be used for WLAN systems.

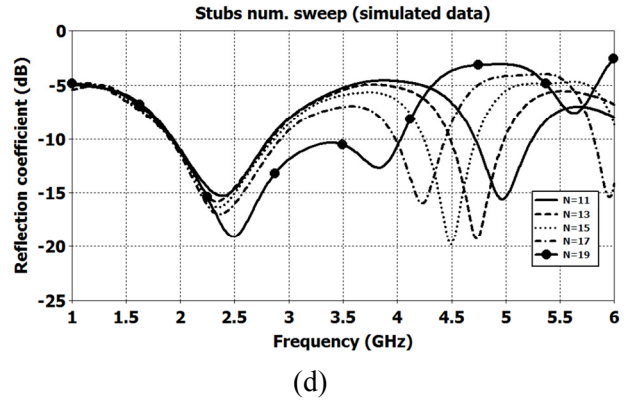
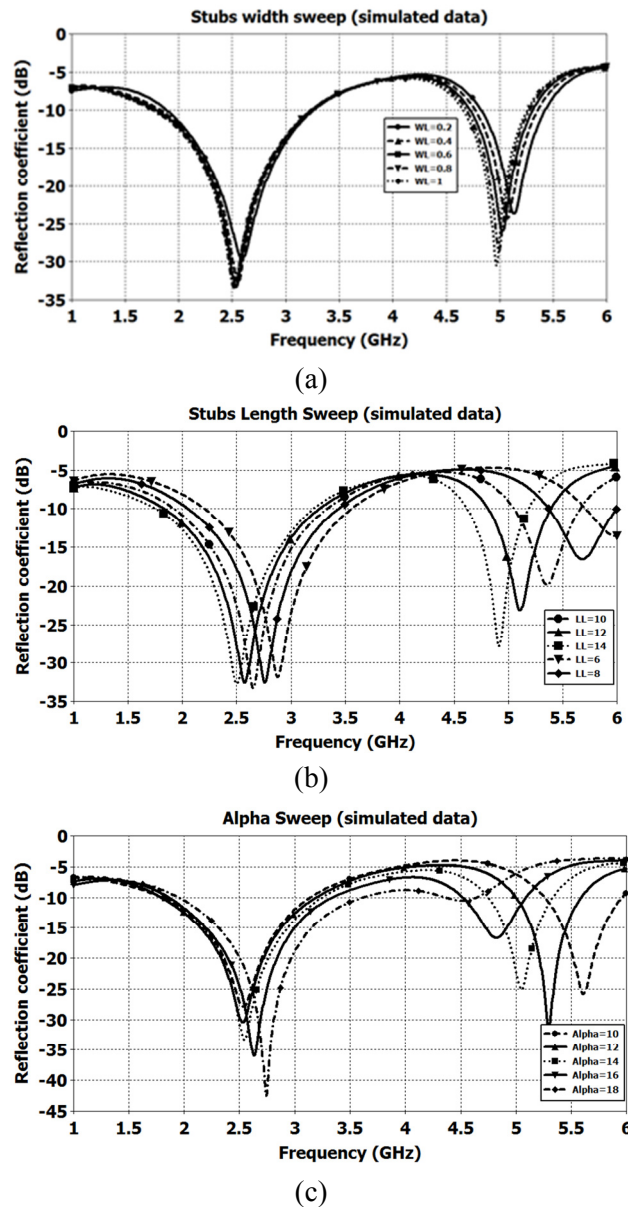
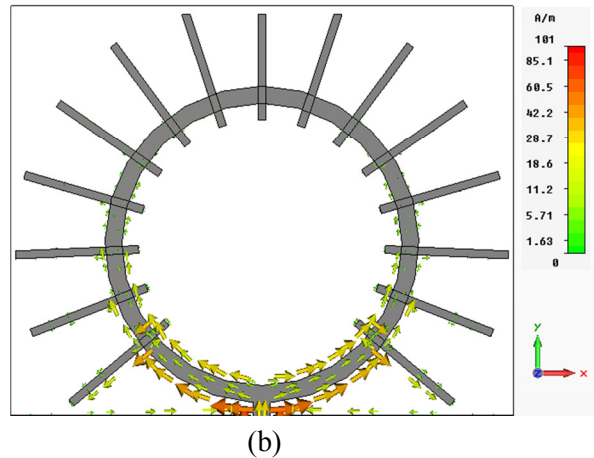
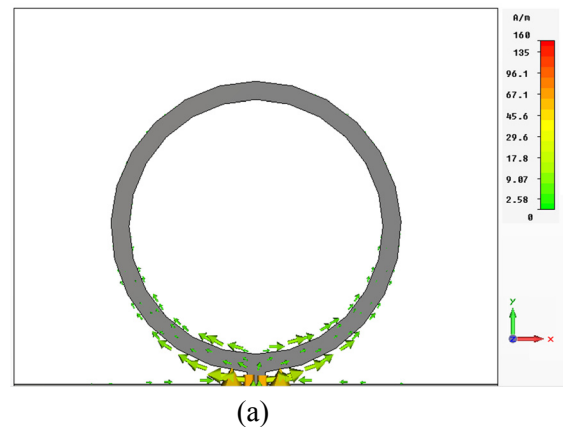
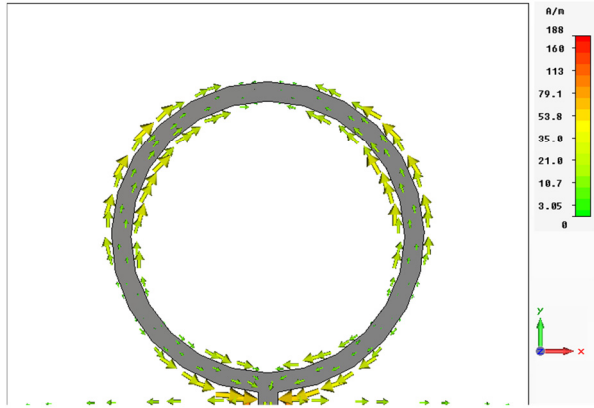
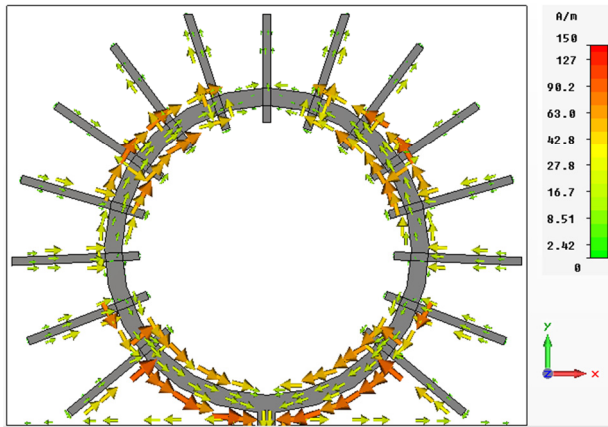


Fig. 6. Parametric study of loaded ring antenna. (a) stub width; (b) stub length; (c) stub displacement; (d) number of stubs.





(c)



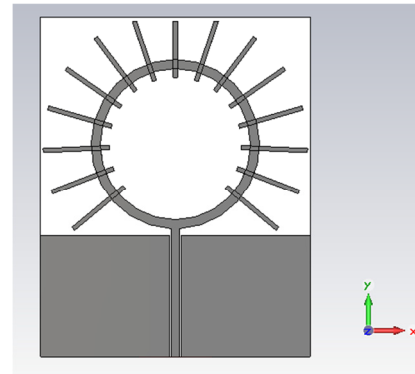
(d)

Fig. 7. Simple and loaded ring antenna current distributions. (a, b) at 2.5GHz (first band); (c, d) at 5.25GHz (second band).

IV. BANDWIDTH ENHANCEMENT VIA INDUCTIVE LOADING

Observe that the dual-band application can be achieved by stub loadings. We may utilize these dual-band characteristics of the antenna to make it wideband, based on the same principles used for increasing the bandwidths of filters [11]. Consequently, we try to bring the two resonance frequencies closer together, in order to make the antenna radiation performance wideband. The optimizer using the genetic algorithm in the CST simulation software is used for the parametric analysis of the antenna to obtain dual-band and wideband performances. Then, the number, size and angular spacing of branch lines are optimized to obtain a wide frequency response as much as realizable. The first and second resonance

frequencies may be drawn together by varying the stub lengths and obtain a relatively wideband performance for the antenna. Of course, the number and angular spacing of stubs should be optimized to achieve the best return loss, as may be observed from Fig. 6(c, d). The geometrical configuration of the designed wideband ring antenna with stub loadings is drawn in Fig. 8. Its reflection coefficient versus frequency and radiation patterns are drawn in Figs. 9 and 10, respectively. Observe that its return loss bandwidth is 80% at the center frequency of 3.15GHz. The computer simulation may actually be carried out for different resonance frequencies, but the curves are given for a single frequency to avoid crowding the figures. Also the radiation patterns are not adversely affected by the addition of stubs.



W	W ₁	W ₂	L	L ₁	L ₂
32	15.4	0.63	40	14.2	15
G	R	W _L	L _L	α	N
0.18	10	0.5	7	18.5°	15

Fig. 8. Optimum loaded ring antenna reflection coefficient. Dimensions are in millimeters.

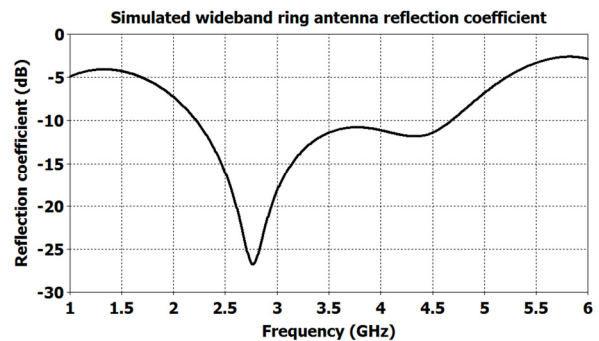


Fig. 9. Optimum loaded ring antenna reflection coefficient.

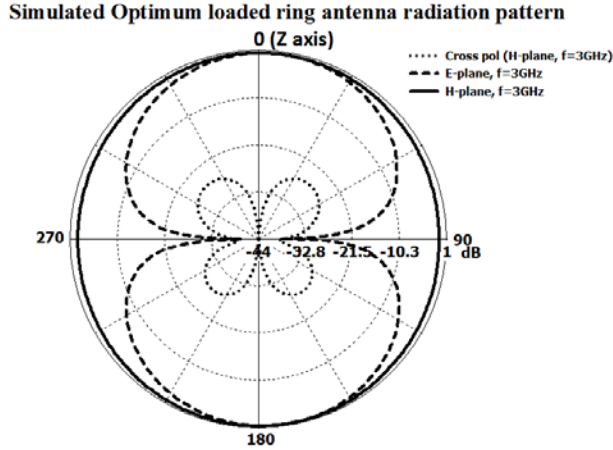
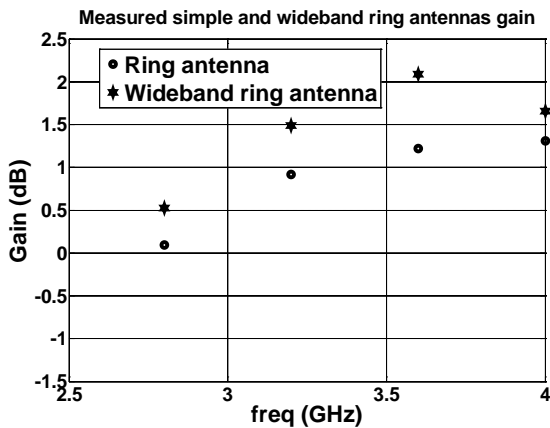
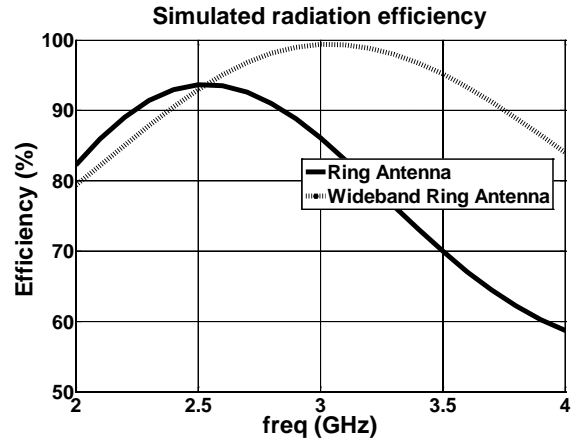


Fig. 10. Optimum loaded ring antenna radiation pattern at 3GHz. (dashed) E-plane (y-z plane); (solid) H-plane (x-z plane); (dotted) cross-polar (H-plane).

The results of simulation for the radiation efficiency of antennas and the measurement of antenna gain are given in Fig. 11. The gain of loaded antenna is a somewhat greater than the simple ring antenna. The reason may be due to the increase of current path length, as is evident from Fig. 7(d), which has led to the effective enlargement of antenna. As reducing antenna size leads to reduction of antenna's gain and efficiency [12, 13], increase in the radiation efficiency of loaded antenna may be due to current path increase.



(a)



(b)

Fig. 11. Ring antenna and wideband ring antennas (a) radiation efficiencies; and (b) gains versus frequency.

V. EXPERIMENTAL RESULTS AND COMPARISON

A simple and a stub loaded ring antenna are fabricated and measured, as shown in Figs. 1 and 8, respectively. Their photographs are shown in Fig. 12. Their reflection coefficients as obtained by simulation results and measurement data are shown in Figs. 13 and 14, respectively. Observe that the relative bandwidth of the stub loaded ring antenna has increased by about 230% relative to the simple ring antenna. The variation between the simulation results and measurement data may be due to the fabrication tolerance and approximations made in the computer simulation.

The far field pattern of the fabricated ring antenna is measured at the frequency of 3GHz and compared with the simulation results in Fig. 15. The patterns of the fabricated loaded ring antenna is measured at two frequencies (3, 4 GHz) and drawn in Fig. 16, together with computer simulation results for comparison. Observe that the stub loading of the ring antenna has little effect on the radiation pattern of the original ring antenna in the wide frequency band from 1.8 to 4GHz.

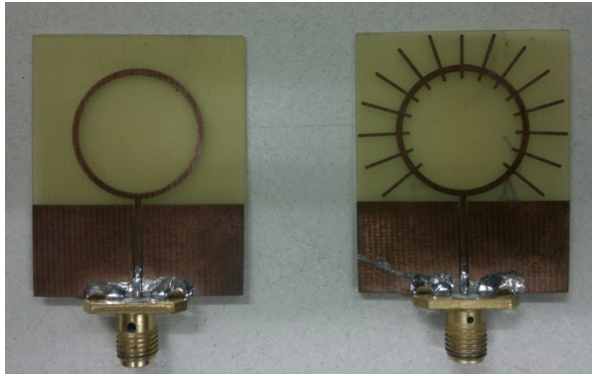


Fig. 12. Photographs of the ring and optimum loaded ring antennas.

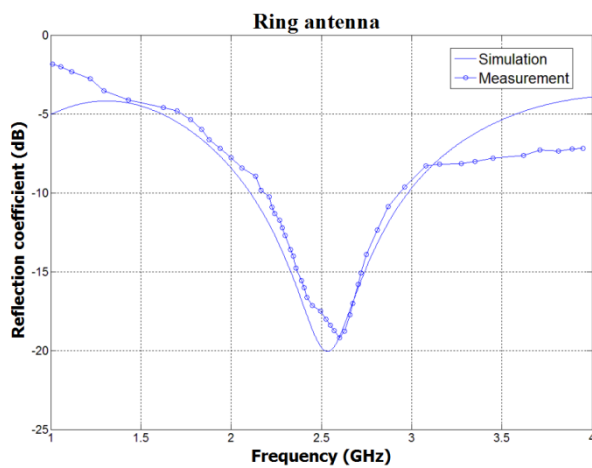


Fig. 13. Simulated and measured reflection coefficients of the simple ring antenna.

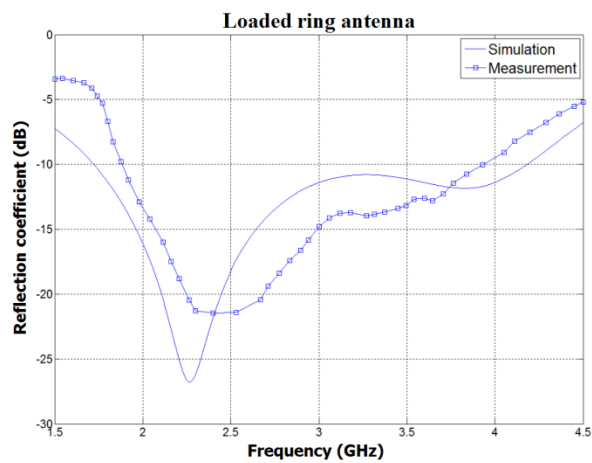


Fig. 14. Simulated and measured reflection coefficients of the optimum loaded ring antenna.

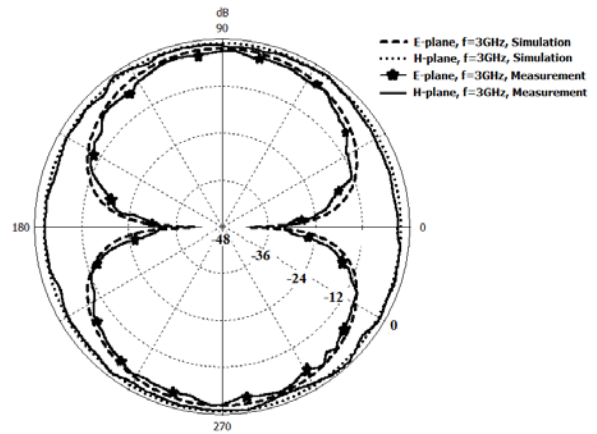
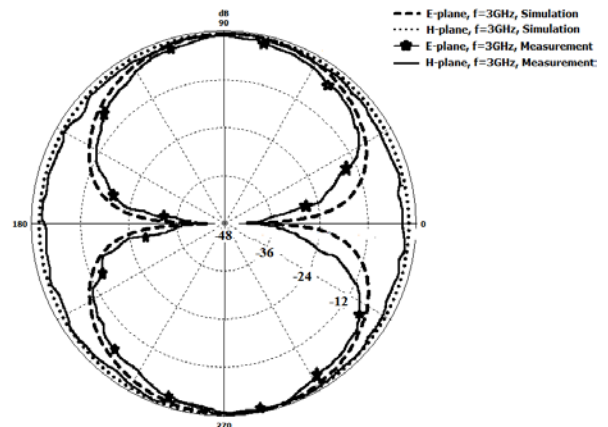
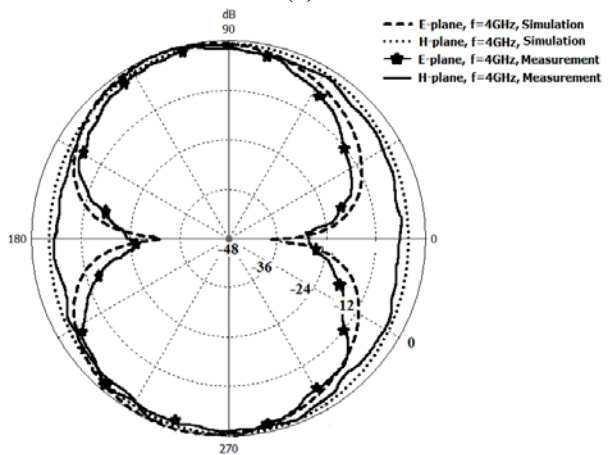


Fig. 15. Simple ring antenna normalized radiation patterns at 3GHz (E-plane (yoz)).



(a)



(b)

Fig. 16. Optimum loaded ring antenna normalized radiation patterns. at: (a) 3GHz; (b) 4GHz.

VI. CONCLUSION

It is demonstrated that the inductive loading of a CPW ring antenna by open-circuited radial line sections spaced around its periphery is a potential and an effective method for its dual-banding and broad banding performance, without any degradation of its radiation pattern. The proper design of the loaded ring antenna (in terms of the determination of lengths and widths of line sections and their spacings,) has actually achieved a 230% increases in antenna relative frequency bandwidth with excellent stability of the radiation pattern. Consequently, the stub loadings of an antenna by open-circuited line sections may be introduced as an effective method for enhancing frequency bandwidths and dual banding of antennas.

REFERENCES

- [1] K. F. Lee and K. M. Luk, *Microstrip Patch Antennas*. Imperial College Press, 2011.
- [2] K. F. Lee, S. L. S. Yang, and A. A. Kishk, "Dual and Multi-Band U-Slot Antenna," *IEEE Transactions on Antennas and Propagation Lett.*, vol. 7, pp. 645-647, 2008.
- [3] D. S. Javan and O. H. Ghouchani, "Cross Slot Antenna with U-Shaped Tuning Stub for Ultra Wideband Applications," *Applied Computational Electromagnetics Society (ACES) Journal*, vol. 24, no. 4, pp. 427-432, August 2009.
- [4] J. William and R. Nakkeeran, "A New UWB Slot Antenna with Rejection of WiMax and WLAN Bands," *Applied Computational Electromagnetics Society (ACES) Journal*, vol. 25, no. 9, pp. 787-793, September 2010.
- [5] M. N.-Jahromi and N. K.-Barchloui, "Analysis of the Behavior of Sierpinski Carpet Monopole Antenna," *Applied Computational Electromagnetics Society (ACES) Journal*, vol. 24, no. 1, pp. 32-36, February 2009.
- [6] A. T. Mobashsher, M. T. Islam, and N. Misran, "Wideband Compact Antenna with Partially Radiating Coplanar Ground Plane," *Applied Computational Electromagnetics Society (ACES) Journal*, vol. 26, no. 1, pp. 73-81, January 2011.
- [7] K. F. Lee, K. M. Luk, T. Mak, and S. S. L. Yang, "Dual and Triple Band Stacked Patch Antennas with U-Slots," *Proceedings of the 2010 EuCap Conference*, April 2010.
- [8] J. Liang, C. C. Chiau, X. Chen, and C. G. Parini, "Printed Circular Disc Monopole Antenna for Ultra Wideband Applications," *Electronics Letters*, vol. 40, no. 20, pp. 1246-1248, 30th September 2004.
- [9] W. Wang, S. S. Zhong, and S.-B. Chen, "A Novel Wideband Coplanar-Fed Monopole Antenna," *Microwave and Optical Technology Letters*, vol. 43, no. 1, pp. 50-52, October 5 2004.
- [10] S.-Y. Suh, W. Shutzman, W. Davis, A. Waltho, and J. Schiffer, "A Novel CPW-Fed Disc Antenna," *IEEE Antennas and Propagation Society Symposium*, vol. 3, pp. 2919 - 2922, June 20-25, 2004.
- [11] G. Bianchi and R. Sorrentino, *Electronic Filter Simulation & Design*. McGrawHill, 2007.
- [12] H. A. Wheeler, "Fundamental Limits of Small Antennas," in *Proc. IRE*, vol. 35, pp. 1479-1484, Dec. 1947.
- [13] R. F. Harrington, "Effect of Antenna Size on Gain, Bandwidth, and Efficiency," *Journal of Research of the National Bureau of Standards-D. Radio Propagation*, vol. 64D, pp. 1-12, Jan-Feb 1960.



Homayoon Oraizi (SM'98)

received the B.E.E. degree from the American University of Beirut, Beirut, Lebanon, in 1967, and the M.Sc. and Ph.D. degrees in Electrical Engineering from Syracuse University, Syracuse, NY, in 1969 and 1973, respectively.

From 1973 to 1974, he was a Teacher with the K. N. Tousi University of Technology, Tehran, Iran. From 1974 to 1985, he was with the Communications Division, Iran Electronics Industries, Shiraz, Iran, where he was engaged in various aspects of technology transfer mainly in the field of HF/VHF/UHF communication systems. In 1985, he joined the Department of Electrical Engineering, Iran University of Science and Technology, Tehran, Iran, where he is currently a Full Professor of electrical engineering. He teaches various courses in electromagnetic engineering and supervises theses and dissertations.

He has conducted and completed numerous projects in both industry and with universities. From July 2003 to August 2003, he spent a two-month term with Tsukuba University, Ibaraki, Japan. From August 2004 to February 2005, he spent a six-month sabbatical leave at Tsukuba University. He has authored or coauthored over 200 papers in international journals and conferences. He has authored and translated several textbooks in Farsi. His translation into Farsi of *Antenna Analysis and Design*, 4th ed. (Iran Univ. Sci. Technol., 2006) was recognized as the 1996 Book of the Year in Iran. In 2006, he was elected an exemplary nation-wide university professor in Iran. He is an Invited Professor of the Electrical Engineering Group, Academy of Sciences of Iran, Tehran, Iran. He is listed as an elite engineer by the Iranology Foundation. He was listed in the 1999 Who's Who in the World. His research

interests are in the area of numerical methods for antennas, microwave devices, and radio wave propagation.



Bahram Rezaei received the B. S. degree from the Semnan University, Semnan, Iran in 2005 and M. S. degree from K. N. Toosi University of Technology, Tehran, in 2007. Currently, he is working towards the Ph.D. degree at Iran University of Science and

Technology.

For several years, he served as an RF research engineer. He has designed, modified and fabricated various types of synthesizers, up-converters and down-converters.

Accurate Modeling of a Patterned Ground and its Application to Microwave Filters

Wei Shao¹ and Jia-Lin Li^{1,2}

Institute of Applied Physics

¹ University of Electronic Science and Technology of China, Chengdu 610054, P. R. China

² State Key Laboratory of Millimeter Waves, Southeast University, Nanjing 210096, P. R. China

weishao@uestc.edu.cn, jialinuestc@yahoo.com.cn

Abstract — A patterned ground and its exactly equivalent lumped circuit model are analyzed in depth in this paper. Characteristics of the introduced patterned ground include providing the finite attenuation pole and reflection pole near the cutoff frequency, thus effectively improving the frequency-response selectivity. The basic unit cell and its performance are first studied. A circuit theory-based lumped model is then introduced. To verify the developed equivalent model, a prototype low-pass filter using three cascaded cells is designed. Results of the prototype filter show a good consistency between the experiment and theory.

Index Terms — Attenuation pole, lumped element model, patterned ground, reflection pole.

I. INTRODUCTION

In general, the patterned ground is obtained by etching some shapes/structures on a ground plane of a microwave planar circuit. It is also called defected ground structures (DGSs) or in some cases split ring resonators (SRRs). It can exhibit a bandgap, slow/fast-wave or negative index refraction characteristics. In recent decades, many researchers have been devoted to studying such kinds of structures, and many characteristics/performances are exploited. These properties have been imposed to many applications in microwave engineering such as balun [1], directional coupler [2], antenna [3] and so on, while the most common application is for microwave filters including lowpass type [4-11], bandpass type [10-18], bandstop type [19], UWB

type [20,21] and multi-band filters [22,23]. Basic advantages in introducing these structures in the microwave circuits are extending operation bandwidth [1], reducing circuit area [2,4,6-8], achieving wide stopband [7,11-13], generating required multi-band responses [22,23], implementing reconfigurable function [24], etc.

On the other hand, the patterned ground is a special structure that cannot be found in classic microwave engineering. Thus, studying and designing such a structure generally involves full-wave electromagnetic (EM) simulations with try and error. In this process, an equivalent circuit model that is either circuit theory-based or physical structure-based or a combination between them is important in studying and designing, especially, when many etched patterns are cascaded. The cascaded patterns are necessary and important to further improve the circuit performance in applications. To date, many equivalent circuit models are presented [1,4-9,12,23,24], but no general models are found to be suitable for all patterns due to the complexity and variety of the patterned shape. Moreover, many models developed are only applicable to only one unit cell. Their accuracy may be greatly degraded, or even failed, when they are applied to the cascaded cells.

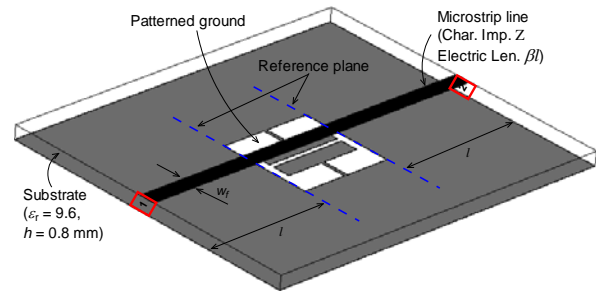
In this article, we study a patterned ground and its equivalent lumped circuit model. EM characteristics of the studied structure are first investigated. Results indicate that the presented pattern can provide attenuation and reflection poles near the cutoff frequency, thus greatly improving the frequency selectivity for filter applications. To model this pattern, a circuit

theory-based lumped element model is proposed. The developed model is simple and accurate. Moreover, it is suitable not only for the unit cell but also for the cascaded patterns. To verify the study, a five-order filter is investigated and confirmed. Demonstration on the prototype filter is also performed, theoretically and experimentally, with a good consistency.

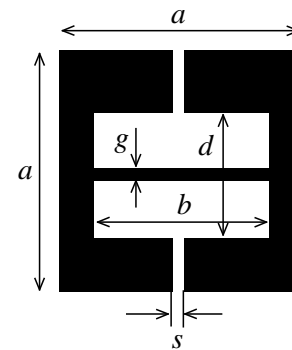
II. PATTERNED GROUND AND ITS UNIT EQUIVALENT CIRCUIT MODEL

Figure 1(a) shows the 3-D view of the introduced patterned ground, while its physical parameters are illustrated in Fig. 1(b). The pattern area is denoted by $a \times a$, so it is a square contour in shape. Within the etched region, a narrow strip with width s loads a capacitive patch. The capacitive patch is represented by length b and width $(d-g)/2$. Basic operation principle of this kind of structure, taking a hole on the ground as an example, is that due to the ground etching, the ground perfection is disturbed, and therefore, the etched ground creates current path surrounding to the contour of the hole, corresponding to lengthened current lines. The lengthened current lines can be equivalent to a lumped inductance. Moreover, the imperfect ground also creates the charge accumulation, and this phenomenon can be analyzed based on the capacitance effects. Consequently, a hole on the ground can be formulated as an LC network to generate resonance (notch response) at some frequencies. On the other hand, in view of transmission lines, it is known that a high impedance microstrip line exhibits inductance effect while a microstrip patch corresponds to an equivalent capacitance. Therefore, we introduce narrow strips loading capacitive patches within an etched hole, where the narrow strip functions as an enhanced distributed inductance and the capacitive patch corresponds to an enhanced equivalent capacitance. Thus, this improved structure can create the larger equivalent inductance and capacitance within a given area compared to a standard hole. It will be shown later that with this improvement, not only the resonance is lowered but also good responses including a sharp transition skirt are observed, making the studied structure be interesting for application to some kinds of microwave components. The pattern is etched beneath a microstrip line (line width w_f)

and the substrate utilized has a thickness $h = 0.8$ mm and relative permittivity $\epsilon_r = 9.6$ in this study.



(a) 3-D view.



(b) Detailed parameter formulation.

Fig. 1. Studied patterned ground.

To investigate the electric performance of the unit patterned ground, the reference plane should be placed at the two edges of the pattern as given in Fig. 1(a). However, if so, drastic discontinuity will be suffered from and the simulation results cannot be convincing for the utilized full-wave EM simulator (Ansoft Ensemble 8). Therefore, the excitation ports are selected as 5 mm ($l = 5$ mm in Fig. 1(a)) away from the reference planes when performing the EM simulations. Figure 2(a) describes the simulated responses where the physical parameters referring to Fig. 1(b) are $a = 7$ mm, $b = 5.8$ mm, $d = 3$ mm, $s = 0.2$ mm, $g = 0.2$ mm and the strip width $w_f = 1.2$ mm in Fig. 1(a). Based on the EM simulations, it is obvious to see that the studied pattern exhibits a reflection pole f_r that is close to the resonance f_0 , and above the f_r , a fast slew rate is observed. Near the resonance f_0 , the pattern has a sharp roll off at the lower transition skirt; while at the upper band, it has a relatively wide attenuation band. For the observed responses, it is interesting to note that this structure can provide a reflection pole f_r near the resonance f_0 compared to most patterned

grounds. It is believed that the generated reflection pole f_r primarily results from the narrow strip loading capacitive patch. This loading greatly compensates for the equivalent inductance because for an etched hole alone, its equivalent inductance is generally smaller than its equivalent capacitance and hence, it is difficult to be matched to the characteristic impedance of a transmission line based on $Z_0 = (L_0/C_0)^{0.5}$. But for the studied patterned ground, its equivalent inductance can be effectively enhanced. Thus, in this case, idea matching is possible at some frequencies. To confirm this analyses, current distribution from EM simulations is provided at the reflection pole frequency f_r . As shown in Fig. 2(b), the current near and within the patterned region is continues and provides a good circulation path, indicating that the matching condition is good at the frequency of f_r .

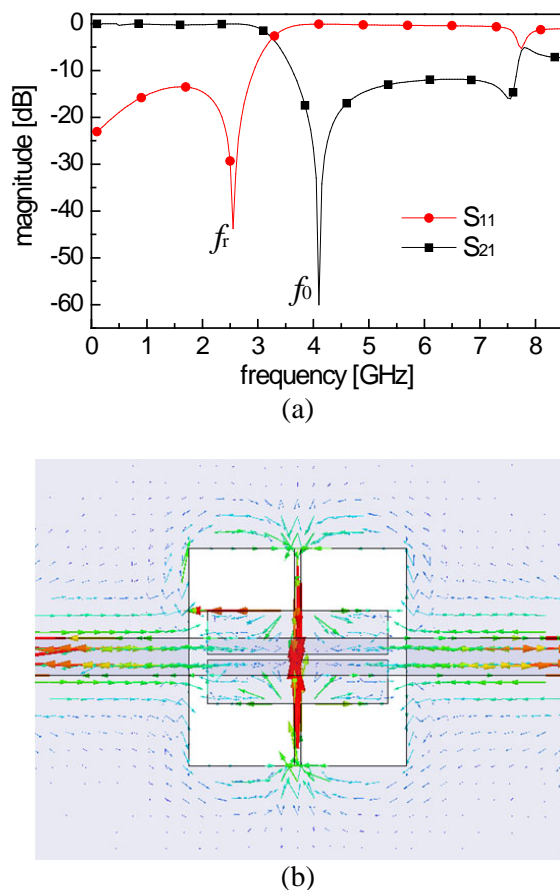


Fig. 2. (a) EM simulated results of the studied pattern. (b) Current distributions at the frequency of f_r .

From Fig. 2(a), it is also observed that the response exhibits another passband around the frequency of 8GHz. The phenomenon results from the periodicity of microwave transmission lines. And we will show below that this spurious passband is also modeled exactly for the cascaded patterns.

Therefore, the introduced pattern features an enhanced frequency selectivity and a widened attenuation compared to some other patterns [5,7-9]. From these responses, one can see that the studied structure is potentially useful to microwave filter applications with enhanced performance.

To give a further insight into this structure, here we sweep the physical parameter b to investigate its frequency responses. Intuitively, decreasing b corresponds to reducing the equivalent capacitance and therefore, its resonance f_0 will shift to higher frequencies. Figure 3 presents the EM simulations of the sweeping results. It is seen that the resonances do shift to the lower frequencies with a larger b , while the reflection poles are lowered. From the frequency responses for three different b values ($b = 5.0, 5.8$ and 6.6 mm respectively), it is seen that a greater b lowers both resonances f_0 and reflection poles f_r , while the attenuation band maintains a similar level. Moreover, a greater b results in a steeper transition skirt, however, the attenuation bandwidth under this case is reduced slightly. Therefore, these results give us useful insights that if the transition skirt is the first consideration in design specifications, one can choose a greater b to achieve the goal. Sweeping other physical parameters can provide different responses, but similar insights can be obtained and these investigations are not presented here for brevity.

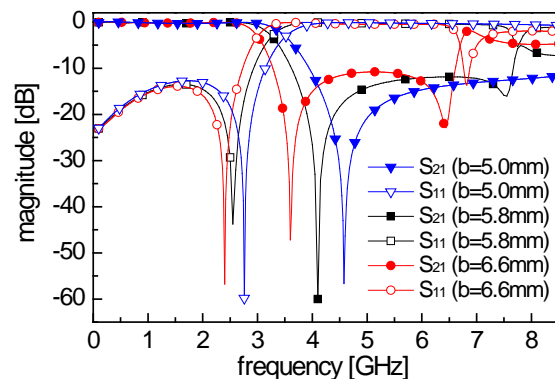


Fig. 3. Sweeping responses of parameter b .

Based on the above results, an equivalent lumped element model is proposed. Figure 4 describes this model, where its key part is represented by a parallel LC network (L_0 and C_0) that determines the basic resonance, f_0 . Notice that this model does not include any resistance element because the investigated pattern is assumed to be lossless in the study. In Fig. 4, transmission line models with characteristic impedance Z and electric length βl formulate the microstrip-line section from excitation port to the reference plane in Fig. 1(a). To extract the lumped LC-parameter values, S-parameters of the patterned ground with a unit cell are obtained from EM simulations. By using the relationship between S-parameter and ABCD-matrix, equivalent LC-element values can be extracted. Figure 5 compares the performance resulting from the EM simulation and the lumped circuit simulation. As can be found, the shunt L_0 and C_0 clearly predict the resonance f_0 when $L_0 = 1.2512\text{nH}$ and $C_0 = 1.2093\text{pF}$ under physical parameters of a unit cell presented before. To more accurately predict the reflection pole f_r , a shunt capacitor C_1 is introduced as shown in Fig. 4. With this improvement, the pole f_r between EM and circuit simulations reasonably matches when $C_1 = 0.5041\text{pF}$, as illustrated in Fig. 5(a). Finally, the wide attenuation is considered by introducing a T-network with inductors L_1 and L_2 in series and then a capacitor C_2 in shunt between them as shown in Fig. 5(b). And the T-network is in series to the above equivalent circuit. Therefore, the entire lumped LC model is proposed as described in Fig. 4. By extracting the lumped parameter values, well matched responses between the EM and circuit simulations are observed as illustrated in Fig. 5, where $L_0 = 1.2512\text{nH}$, $C_0 = 1.2093\text{pF}$, $C_1 = 0.5041\text{pF}$, $L_1 = 2.5422\text{nH}$, $L_2 = 1.1176\text{nH}$, and $C_2 = 1.6855\text{pF}$.

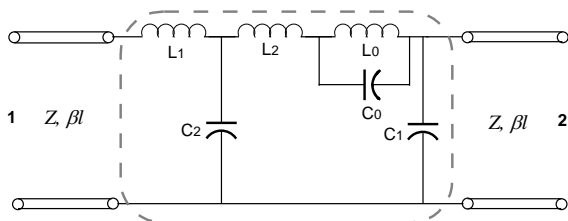
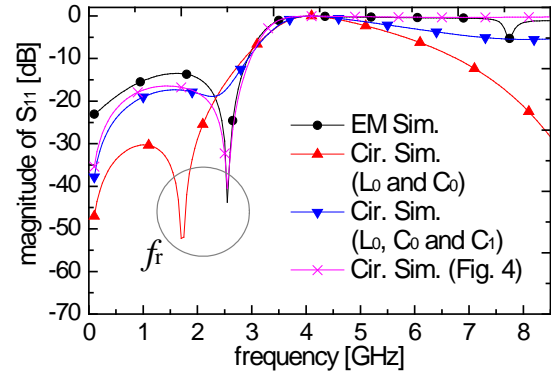
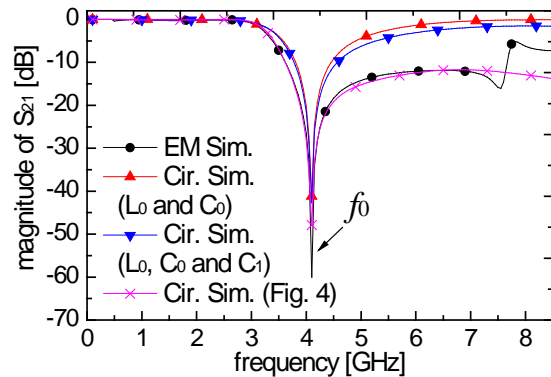


Fig. 4. Developed equivalent circuit model.



(a) Reflection responses



(b) Attenuation (or transmission) responses

Fig. 5. Influence of the equivalent circuit element on the performance.

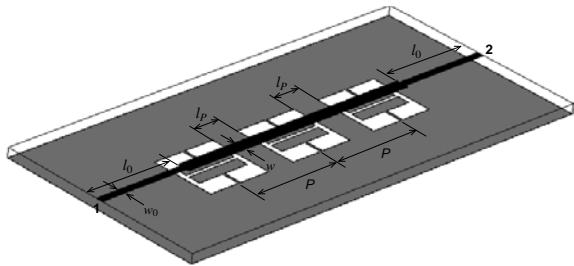
III. A FIVE-ORDER FILTER BASED ON THE STUDIED PATTERNED GROUND

To illustrate the introduced pattern for microwave filter applications and validate the effectiveness of its equivalent model, a five-order filter is demonstrated by cascading three unit cells of the studied pattern. In this case, the microstrip feed lines are set as width $w_0 = 0.8\text{mm}$ (corresponding to characteristic impedance $Z_0 = 50\Omega$) and length $l_0 = 10\text{mm}$ for the input and output. Block diagram of the filter is shown in Fig. 6(a), where the patterned ground is described by the equivalent model given in the dashed box in Fig. 4. The microstrip-line width of the coupling region is the same as w_f in Fig. 1(a), i.e., $w = 1.2\text{mm}$. Figure 6(b) depicts a 3-D view of the physical structure of the filter. It is designed based on the proposed equivalent model and the coupling separation between two unit cells is found as $l_p = 3\text{mm}$, corresponding to a periodicity P , a quarter guided-wavelength at the cutoff

frequency. The optimized LC parameters are: $L_0 = 1.3061\text{nH}$, $C_0 = 1.2295\text{pF}$, $C_1 = 0.2271\text{pF}$, $L_1 = 2.4429\text{nH}$, $L_2 = 1.1977\text{nH}$, and $C_2 = 1.3061\text{pF}$, which correspond to a resonance at 4 GHz approximately.



(a) Block diagram of the filter.



(b) 3-D view of the filter.

Fig. 6. Five-order filter based on the studied patterned ground.

Figure 7 presents the simulated frequency responses based on the equivalent circuit parameters and full-wave EM simulator. From the simulated responses, the circuit model not only predicts the reflection poles clearly, but also formulates the attenuation pole precisely. More importantly, the spurious resonance is predicted exactly. The results show a very good agreement between them. These results also indicate that the proposed lumped element model is efficient to model the studied patterned ground for cascaded cells.

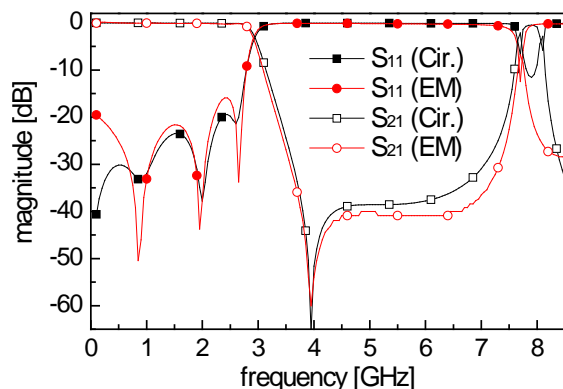


Fig. 7. Circuit design and EM results of the filter.

IV. EXPERIMENTAL VALIDATIONS AND RESULTS

Based on the above designs, the five-order prototype filter is fabricated on a substrate with a relative permittivity of 9.6 and a thickness of 0.8mm. Figure 8 shows the photograph of the built circuits, where the upper section denotes the front side of the circuit, and lower section represents the back side of the circuit. Experimental studies of the circuit are carried out on an Agilent E5071C ENA series network analyzer (frequency range 100kHz-8.5GHz). It is calibrated based on the through-reflection-line (TRL). Figure 9 describes the measured performance of this prototype filter. It is found from measurements that there are three reflection poles at 1.04, 2.11, and 2.60GHz with levels over 45, 30 and 40dB, respectively; an attenuation pole locates at 3.66GHz with an attenuation level over 60dB that is close to a reflection pole of 2.60GHz, thus resulting in a sharp transition skirt of $|S_{21}|$ curve. Measurements also indicate that the attenuation band is better than 35dB from 3.39 to 7.37GHz, and a spurious resonance at approximate 7.85GHz is found. Within the passband, the measured insertion loss is around 0.5 dB and group delay is about 0.8ns.

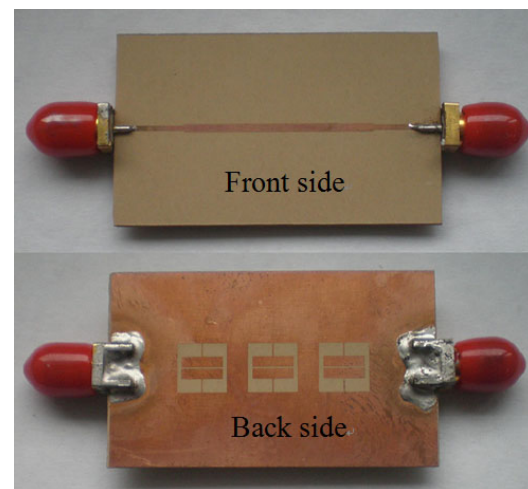


Fig.8. Photograph of the patterned ground filter.

From the measured and simulated results of the demonstrator, some discrepancies are also found. These discrepancies primarily exhibit a slight frequency shift, which can be attributed to the fabrication uncertainties. In general, the measurements match simulations well. These

results confirm that the studied patterned ground structure is capable of implementing microwave filters with high performance, and more importantly, the developed lumped LC network can accurately model the cascaded patterns.

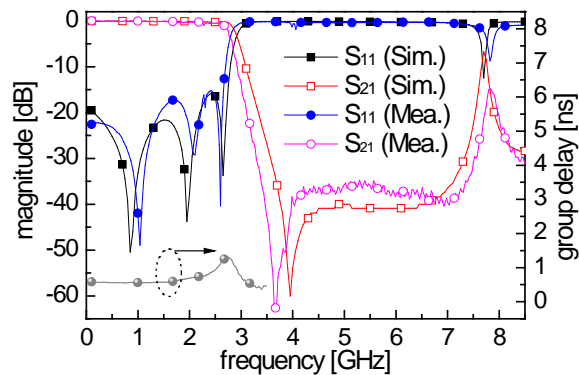


Fig. 9. Performance of the prototype filter.

VI. CONCLUSION

In this paper, we have studied a patterned ground and its accurately equivalent circuit model for microwave filter applications. The introduced structure exhibits both reflection pole and attenuation pole placed near the cutoff frequency and a wide attenuation band. A circuit model suitable not only for a unit cell but also for the cascaded cells is proposed. The model is simple and accurate. To verify the study, a demonstration circuit by cascading three patterned cells has been investigated. Results from the circuit model, EM simulations and experiments validate the studies with a good agreement. The introduced patterned ground and its equivalent model are interesting to be potentially applied to the modern microwave engineering.

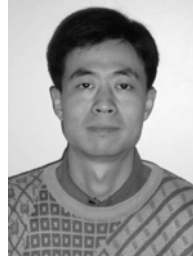
ACKNOWLEDGMENT

This work is supported by the Fundamental Research Funds for the Central Universities (ZYGX2011X009 and ZYGX2010J043), DPR Foundation (9140A21060211DZ0208) and Open Foundation of State Key Laboratory of Millimeter Waves (K201205).

REFERENCES

- [1] M.-A.-S. Eddin and A.-M.-E. Safwat, "Defected-Ground Coupled Microstrip Lines and its Application in Wideband Baluns," *IET Proceedings on Microwave, Antenna and Propagation*, vol. 1, no. 4, pp. 893-899, Aug. 2007.
- [2] A.-S. Mohra, M.-A. Alkanhal, and E.-A. Abdullah, "Size-Reduced Defected Ground Microstrip Directional Coupler," *Microwave and Optical Technology Letters*, vol. 52, no. 9, pp. 1933-1937, Sept. 2010.
- [3] J. Liu, W.-Y. Yin, and S. He, "A New Defected Ground Structure and its Application for Miniaturized Switchable Antenna," *Progress In Electromagnetics Research*, vol. 107, pp. 115-128, 2010.
- [4] J. Li, J.-X. Chen, Q. Xue, J. Wang, W. Shao and L. Xue, "Compact Microstrip Lowpass Filter Based on Defected Ground Structure and Compensated Microstrip Line," *IEEE MTT-S Dig.*, pp. 1483-1486, 2005.
- [5] J.-S. Lim, C.-S. Kim, D. Ahn, Y.-C. Jeong, and S. Nam, "Design of Low-Pass Filters using Defected Ground Structure," *IEEE Transactions on Microwave Theory and Techniques*, vol. MTT-53, no. 8, pp. 2539-2545, Aug. 2005.
- [6] J.-X. Chen, J.-L. Li, K.-C. Wan and Q. Xue, "Compact Quasi-Elliptic Function Filter Based on Defected Ground Structure," *IEE Proceedings on Microwave, Antenna and Propagation*, vol. 153, no. 4, pp. 320-324, Aug. 2006.
- [7] J. Yang and W. Wu, "Compact Elliptic-Function Low-Pass Filter using Defected Ground Structure," *IEEE Microwave and Wireless Components Letters*, vol. 18, no. 8, pp. 578-580, Sept. 2008.
- [8] H. A. Mohamed, H. Taher, E. A. Abdallah, and H. S. El-Henawy, "Design of Seven-Pole LPF with High Suppression of Harmonics using DGS," *Microwave and Optical Technology letters*, vol. 51, no. 3, pp. 759-762, Mar. 2009.
- [9] X.-Q. Chen, L.-X. Wang, and X.-S. Shi, "A Novel Compact Low-Pass Filter using Defected Ground Structure," *Microwave and Optical Technology Letters*, vol. 51, no. 3, pp. 792-795, Mar. 2009.
- [10] G.-E. Al-Omair, S.-F. Mahmoud, A.-S. Al-Zayed, "Lowpass and Bandpass Filter Designs Based on DGS with Complementary Split Ring Resonators," *Applied Computational Electromagnetics Society (ACES) Journal*, vol. 26, no. 11, pp. 907-914, November 2011.
- [11] M. Al Sharkawy, A. Boutejdar, F. Alhefnawi, O. Luxor, "Improvement of Compactness of Lowpass/Bandpass Filter using a New Electromagnetic Coupled Crescent Defected Ground Structure Resonators," *Applied Computational Electromagnetics Society (ACES) Journal*, vol. 25, no. 7, pp. 570-577, July 2010.
- [12] L.-Y. Ren and H. He, "Wide Stopband Bandpass Filter Based on Dual-Plane Microstrip/Interdigital

- DGS Slot Structure,” *Electronics Letters*, vol. 45, no. 25, pp. 1331-1332, Dec. 2009.
- [13] W. Shen, W.-Y. Yin, and X.-W. Sun, “Compact Substrate Integrated Waveguide (SIW) Filter with Defected Ground Structure,” *IEEE Microwave and Wireless Components Letters*, vol. 21, no. 2, pp. 83-85, Feb. 2011.
- [14] X. Luo, J.-G. Ma, and E. Li, “Bandpass Filter with Wide Stopband using Broadside-Coupled Microstrip T-Stub/DGS Cell,” *Microwave and Optical Technology Letters*, vol. 53, no. 8, pp. 1786-1789, Aug. 2011.
- [15] S.-U. Rehman, A.-F. A. Sheta, and M.-A. S. Alkanhal, “Compact Bandpass Filters with Bandwidth Control Using Defected Ground Structure (DGS),” *Applied Computational Electromagnetics Society (ACES) Journal*, vol. 26, no. 7, pp. 624-630, July 2011.
- [16] F. Karshenas, A.-R. Mallahzadeh, J. Rashed-Mohassel, “Size Reduction and Harmonic Suppression of Parallel Coupled-Line Bandpass Filters using Defected Ground Structure,” *Applied Computational Electromagnetics Society (ACES) Journal*, vol. 25, no. 2, pp. 149-155, February 2010.
- [17] N.-M. Garmjani, N. Komjani, “Improved Microstrip Folded Tri-Section Stepped Impedance Resonator Bandpass Filter using Defected Ground Structure,” *Applied Computational Electromagnetics Society (ACES) Journal*, vol. 25, no. 11, pp. 975-983, November 2010.
- [18] J.-P. Wang, Y.-X. Guo, and D.-G. Fang, “Defected Ground Structure Microstrip Bandpass Filter with Multiple Finite Transmission Zeros,” in *2008 ICMMT Proceedings*, pp. 135-138.
- [19] A. Boutejdar, M. Challal, and A. Azrar, “A Novel Band-Stop Filter using Octagonal-Shaped Patterned Ground Structures along with Interdigital and Compensated Capacitors,” *Applied Computational Electromagnetics Society (ACES) Journal*, vol. 26, no. 4, pp. 312-318, April 2011.
- [20] W.-J. Lin, J.-Y. Li, L.-S. Chen, D.-B. Lin, and M.-P. Houng, “Investigation in Open Circuited Metal Lines Embedded in Defected Ground Structure and its Applications to UWB Filters,” *IEEE Microwave and Wireless Components Letters*, vol. 20, no. 3, pp. 148-150, Mar. 2010.
- [21] J. Mou, W. Yu, and X. Lv, “Compact Ultra-Wideband Bandpass Filter Based on Novel Defected Ground Structure and Folded Coupled Lines,” *Microwave and Optical Technology Letters*, vol. 53, no. 7, pp. 1598-1601, Jul. 2011.
- [22] L.-Y. Ren, “Tri-Band Bandpass Filters Based on Dual-Plane Microstrip/DGS Slot Structure,” *IEEE Microwave and Wireless Components Letters*, vol. 20, no. 8, pp. 429-431, Aug. 2010.
- [23] L. Ren and H. Huang, “Dual-Band Bandpass Filter Based on Dual-Plane Microstrip/Interdigital DGS Slot Structure,” *Electronics Letters*, vol. 45, no. 21, pp. 1077-1079, Oct. 2009.
- [24] H.-B. El-Shaarawy, F. Coccetti, R. Plana, M. El-Said, and E.-A. Hashish, “Reconfigurable Defected Ground Structure Cell using PIN Diodes on Coplanar Waveguide Technology,” *Microwave and Optical Technology Letters*, vol. 52, no. 3, pp. 766-780, Mar. 2010.



Wei Shao received the M. Sc. degree and Ph. D. degrees in Radio Physics from the University of Electronic Science and Technology of China (UESTC), Chengdu, China, in 2004 and 2006, respectively.

He joined the UESTC and is now an associate professor there. He has been a Visiting Scholar in the Electromagnetic Communication Laboratory, Pennsylvania State University in 2010. His research interests include the computational electromagnetic, microwave passive component design, and antenna technique.



Jia-Lin Li received the M. Sc. degree from UESTC, Chengdu, China, in 2004, and the Ph. D. degree from the City University of Hong Kong, Hong Kong, in 2009, both in electronic engineering. Since Sept. 2009, he has been with the Institute of Applied Physics,

School of Physical Electronics, UESTC, where he is currently a Professor. His research interests include the high performance active/passive microwave/millimeter-wave antennas, circuits, and systems realized on PCB, multilayer PCB, LTCC, etc.

Scattering by Chiral Lossy Metamaterial Elliptic Cylinders

A.-K. Hamid

Department of Electrical and Computer Engineering, University of Sharjah
P. O. Box 27272, Sharjah, United Arab Emirates
akhamid@sharjah.ac.ae

Abstract — Electromagnetic fields are expressed in terms of appropriate complex angular and a rigorous solution to the problem of scattering of a plane wave from a chiral lossy metamaterial circular or elliptic cylinder is presented in this paper using the method of separation of variables. The incident scattered as well as the transmitted radial Mathieu functions with expansion coefficients. The incident field expansion coefficients are known, but the scattered and transmitted field expansion coefficients are to be determined. Imposing the boundary conditions at the surface of the chiral lossy metamaterial elliptic cylinder enables the determination of the unknown expansion coefficients. Results are presented as normalized scattering widths for circular and elliptic cylinders of different sizes and chiral lossy metamaterial materials, and for both TE and TM polarizations of the incident wave, to show the effects of these on scattering cross widths.

Index Terms - Chiral lossy, circular and elliptic cylinders, Mathieu functions, metamaterial.

I. INTRODUCTION

A chiral medium is a reciprocal and isotropic medium characterized by different phase velocities for both right and left circularly polarized waves. In a lossless chiral medium, a linearly polarized wave undergoes a rotation of its polarization as it propagates. For chiral cylinders, these properties result in a coupling of the TM and TE polarizations. Analytic and numerical solutions describing chiral media are given by [1, 19]. Recent work on the scattering and radiation by elliptical structures is given for lossy and lossless dielectric material [20-24].

In this paper, we present the analysis corresponding to the scattering of a plane wave of arbitrary polarization and angle of incidence from a

chiral lossy metamaterial elliptic cylinder of arbitrary axial ratio. Such a solution is valuable, since it can be used as a benchmark for validating solutions obtained using approximate or numerical methods. The analysis and the software used for obtaining the results have been validated, by calculating the normalized backscattering widths for an elliptic cylinder of axial ratio approximately 1, and showing that these results are in excellent agreement with the same obtained for a circular cylinder [12, 15].

II. FORMULATION

Consider a linearly polarized monochromatic uniform plane electromagnetic wave incident on an infinitely long chiral lossy metamaterial elliptic cylinder of major axis a and minor axis b , at an incident angle φ_i with respect to the positive x axis of a Cartesian co-ordinate system located at the centre of the cylinder as shown in Fig. 1. The axis of the cylinder is assumed to be along the z axis. Since the scatterer under consideration is bounded by elliptical surface, it is convenient to use Mathieu functions to satisfy the boundary conditions. Let's define the x and y coordinates of the Cartesian coordinate system in terms of u and v coordinates of an elliptical coordinate system also located at the centre of the cylinder in the form $x = F \cosh u \cos v$, $y = F \sinh u \sin v$, with F being the semi-focal length of the ellipse. A time dependence of $e^{j\omega t}$ is assumed throughout the analysis, but suppressed for convenience where ω is the angular velocity.

For a TE polarized plane wave of amplitude H_0 , the axial component of the incident magnetic field can be written as

$$H_z^i = H_0 e^{jk\rho \cos(\varphi - \varphi_i)}. \quad (1)$$

where $k = 2\pi / \lambda$, λ being the wavelength in the region exterior to the cylinder, and ρ , φ are the polar coordinates.

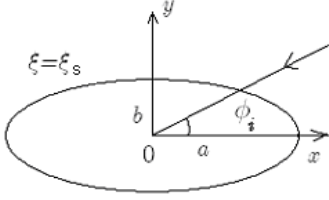


Fig. 1. Geometry of the problem.

Let the elliptic cylindrical vector wave functions \mathbf{N} and $\mathbf{M} = k^{-1}(\nabla \times \mathbf{N})$ be defined as [24]

$$\mathbf{N}_{qm}^{(i)}(c, \xi, \eta) = \hat{z} R_{qm}^{(i)}(c, \xi) S_{qm}(c, \eta). \quad (2)$$

$$\mathbf{M}_{qm}^{(i)}(c, \xi, \eta) = \frac{1}{kh} \begin{bmatrix} \hat{u} R_{qm}^{(i)}(c, \xi) S'_{qm}(c, \eta) \\ -\hat{v} R_{qm}^{(i)'}(c, \xi) S_{qm}(c, \eta) \end{bmatrix}. \quad (3)$$

where $q=e,o$, S_{qm} and $R_{qm}^{(i)}$ are the even and odd complex angular and radial Mathieu functions of the i^{th} kind, both of m order, respectively, $\xi = \cosh u$, $\eta = \cos v$, $c = kF$, \hat{k} denotes a unit vector in the positive k direction, the prime on S and R denotes their respective derivative with respect to v and u , while $h = F\sqrt{\xi^2 - \eta^2}$.

The incident magnetic field can be expanded in terms of angular and radial Mathieu functions as

$$\mathbf{H}^i = \sum_m A_{qm} \mathbf{N}_{qm}^{(1)}(k). \quad (4)$$

in which

$$A_{qm} = H_o j^m \frac{\sqrt{8\pi}}{N_{qm}(c)} S_{qm}(c, \cos \varphi_i). \quad (5)$$

$$N_{qm}(c) = \int_0^{2\pi} [S_{qm}(c, \eta)]^2 dv. \quad (6)$$

The summation over m starts from 0 for even Mathieu functions while 1 for odd Mathieu functions.

Using Maxwell's equations, the electric field can be expanded in terms of angular and radial Mathieu functions as

$$\mathbf{E}^i = jZ \sum_m A_{qm} \mathbf{M}_{qm}^{(1)}(k). \quad (7)$$

where Z is the wave impedance in the region exterior to the cylinder.

Since the elliptic cylinder is made up of chiral metamaterial, the scattered electromagnetic field will have a cross-polarized component in addition to the co-polarized component in contrast to that for a dielectric elliptic cylinder, which would only have a co-polarized component. These co- and cross polarized scattered field components can also be expressed in terms of Mathieu functions as

$$\mathbf{H}^s = \sum_m \left[B_{qm} \mathbf{N}_{qm}^{(4)}(k) + C_{qm} \mathbf{M}_{qm}^{(4)}(k) \right]. \quad (8)$$

$$\mathbf{E}^s = jZ \sum_m \left[B_{qm} \mathbf{M}_{qm}^{(4)}(k) + C_{qm} \mathbf{N}_{qm}^{(4)}(k) \right]. \quad (9)$$

where B_{qm} and C_{qm} are the unknown expansion coefficients of the co- and cross-polarized scattered field components, respectively, while $\mathbf{N}_{qm}^{(4)}$ and $\mathbf{M}_{qm}^{(4)}$ are the elliptic cylindrical vector wave functions of the fourth kind. The transmitted fields inside the chiral material may be written in terms of left and right circularly polarized waves as

$$\begin{aligned} \mathbf{H}^c &= D_{qm} \sum_m \left[\mathbf{N}_{qm}^{(1)}(k_R) + \mathbf{M}_{qm}^{(1)}(k_R) \right] \\ &+ F_{qm} \sum_m \left[\mathbf{N}_{qm}^{(1)}(k_L) + \mathbf{M}_{qm}^{(1)}(k_L) \right]. \end{aligned} \quad (10)$$

$$\mathbf{E}^c = jZ_c \begin{pmatrix} \sum_m D_{qm} \left[\mathbf{N}_{qm}^{(1)}(k_R) + \mathbf{M}_{qm}^{(1)}(k_R) \right] \\ -F_{qm} \sum_m \left[\mathbf{N}_{qm}^{(1)}(k_L) - \mathbf{M}_{qm}^{(1)}(k_L) \right] \end{pmatrix}. \quad (11)$$

where Z_c is the wave impedance of the chiral medium, D_{qm} and F_{qm} are the unknown transmitted expansion coefficients while the left and right circularly polarized wave numbers k_R and k_L are

$$k_R = \frac{\omega\sqrt{\mu_c \epsilon_c}}{1 + \gamma\omega\sqrt{\mu_c \epsilon_c}}, \quad k_L = \frac{\omega\sqrt{\mu_c \epsilon_c}}{1 - \gamma\omega\sqrt{\mu_c \epsilon_c}}. \quad (12)$$

μ_c is the permeability of the chiral medium, ε_c is the permittivity of the chiral medium, and γ is the chiral admittance of the chiral medium. The unknown expansion coefficients can be obtained by imposing the tangential boundary conditions at the surface $\xi = \xi_s$ of the chiral elliptic cylinder, which can be expressed mathematically as

$$H_z^i + H_z^s = H_z^c. \quad (13)$$

$$H_\eta^s = H_\eta^c. \quad (14)$$

$$E_z^i + E_z^s = E_z^c. \quad (15)$$

$$E_\eta^s = E_\eta^c. \quad (16)$$

Substituting the appropriate expressions in (13)-(16), and applying the orthogonal property of the angular Mathieu functions yields

$$\left[A_{qm} R_{qm}^{(1)}(c, \xi_s) - B_{qm} R_{qm}^{(4)}(c, \xi_s) \right] N_{qm}(c) \\ = \sum_m D_{qm} R_{qm}^{(1)}(c_R, \xi_s) M_{qm}(c, c_R) + \quad (17)$$

$$\sum_m F_{qm} R_{qm}^{(1)}(c_R, \xi_s) M_{qm}(c, c_R),$$

$$C_{qm} R_{qm}^{(4)'}(c, \xi_s) N_{qm}(c) = \frac{k}{k_R} \sum_m D_{qm} R_{qm}^{(1)'}(c_R, \xi_s) \quad (18)$$

$$M_{qm}(c, c_R) - \frac{k}{k_R} \sum_m F_{qm} R_{qm}^{(1)'}(c_R, \xi_s) M_{qm}(c, c_R),$$

$$C_{qm} R_{qm}^{(4)}(c, \xi_s) N_{qm}(c) = \frac{Z_c}{Z} \sum_m D_{qm} R_{qm}^{(1)'}(c_R, \xi_s) \quad (19)$$

$$M_{qm}(c, c_R) - \frac{Z_c}{Z} \sum_m F_{qm} R_{qm}^{(1)'}(c_R, \xi_s) M_{qm}(c, c_R),$$

$$\left[A_{qm} R_{qm}^{(1)'}(c, \xi_s) - B_{qm} R_{qm}^{(4)'}(c, \xi_s) \right] N_{qm}(c) = \\ \frac{Z_c k}{Z k_c} \sum_m D_{qm} R_{qm}^{(1)}(c_R, \xi_s) M_{qm}(c, c_R) + \quad (20)$$

$$\frac{Z_c k}{Z k_c} \sum_m F_{qm} R_{qm}^{(1)}(c_R, \xi_s) M_{qm}(c, c_R).$$

where $c_R = k_R F$ and $c_L = k_L F$. To solve for the unknown scattered field coefficients, the system of equations (17-20) may be written in matrix form and the unknown coefficients can be obtained by matrix inversion. The bistatic scattering width is defined as [24]

$$\sigma = \lim_{\rho \rightarrow \infty} 2\pi\rho \frac{\text{Re}[(\mathbf{E}^s \times \mathbf{H}^{s*}) \cdot \hat{\rho}]}{\text{Re}[(\mathbf{E}^i \times \mathbf{H}^{i*}) \cdot \hat{\rho}]} \quad (21)$$

with the asterisk denoting the complex conjugate $\hat{\rho}$ denoting the unit vector in the direction of increasing ρ and $\text{Re}[\]$ denoting the real part of a complex number.

For TE polarization we can write an expression for the normalized bistatic scattering width as

$$\frac{\sigma}{\lambda} = \frac{\sigma_{\text{co-polar}}}{\lambda} + \frac{\sigma_{\text{cross-polar}}}{\lambda}. \quad (22)$$

where

$$\sigma_{\text{co-polar}} = \lambda \left| \begin{array}{l} \sum_{m=0}^{\infty} j^m B_{em} S_{em}(c, \cos \phi) + \\ \sum_{m=1}^{\infty} j^m B_{om} S_{om}(c, \cos \phi) \end{array} \right|^2. \quad (23)$$

and

$$\sigma_{\text{cross-polar}} = \lambda \left| \begin{array}{l} \sum_{m=0}^{\infty} j^m C_{em} S_{em}(c, \cos \phi) + \\ \sum_{m=1}^{\infty} j^m C_{om} S_{om}(c, \cos \phi) \end{array} \right|^2. \quad (24)$$

The expressions for the incident, scattered and transmitted electromagnetic fields for TM case can be obtained using the duality principle of the TE case.

III. NUMERICAL RESULTS

The obtained numerical results are presented as normalized echo pattern widths for chiral lossy and lossless metamaterial circular and elliptic cylinders of different sizes, axial ratios, incident angles, permittivities and permeabilities for both TE and TM polarizations of the incident wave. We have selected $ka = 0.5$, $\varepsilon_{rc} = \pm 4.0$, $\mu_{rc} = \pm 2.0$, $k\gamma = 0.15$ and $\varphi_i = 180^\circ$ to compare the obtained data with published results. To validate the analysis and the software used for calculating the results, we have computed the normalized echo pattern widths for chiral circular cylinder of axial ratio 1.001, as shown in Fig. 2 and in the TM case. The results are in full agreement, verifying the accuracy of the analysis as well as the software used for obtaining the results [12, 15]. Also Fig. 2 shows the echo pattern for chiral lossy and lossless metamaterial circular cylinder with various values of ε_{rc} . The results show for this

particular parameters the co polarized echo pattern increases while the cross polarized decreases by varying the lossy metamaterial when compared with the conventional chiral case (solid lines). Figure 3 is similar to Fig. 2 except for the TE case. The TE case behaves similar to the TM case.

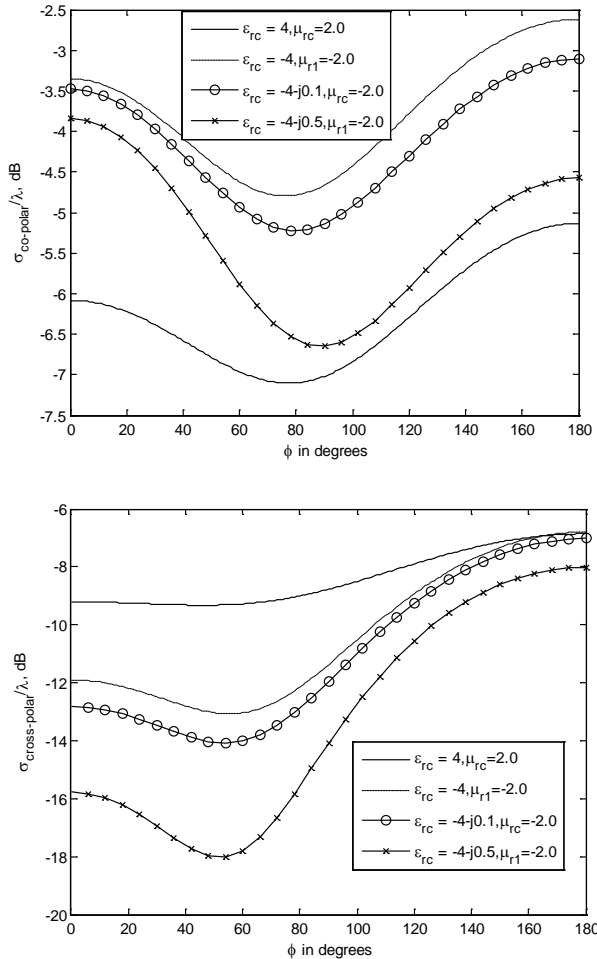


Fig. 2. Echo pattern width versus scattering angle for co and cross polarized chiral lossy metamaterial circular cylinder of $ka=0.5$, axial ratio 1.001, $k\gamma=0.15$ and $\varphi_i = 180^\circ$, TM case.

Figure 4 shows the echo pattern for conventional chiral, lossy and lossless metamaterial elliptic cylinder with $ka=0.5$, $kb=0.25$ and TM case. The numerical results show that the co polarized echo pattern decreases for the scattering angle less than 150° while the cross polarized decreases at all scattering angles when compared to the conventional chiral case (solid lines). Figure 5 is similar to Fig. 4 except for TE case where it behaves differently for the co polarized case.

Figure 6 shows the echo pattern width for chiral lossy metamaterial elliptic cylinder of different axial ratios, $\epsilon_{rc} = -4.0 - j0.5$ and $\varphi_i = 90^\circ$ and for TE case. It can be seen by increasing the axial ratio will decrease the echo pattern width for some particular co polarized cases. Figure 7 shows the echo pattern for different chiral materials and for the same parameters as in Fig. 6.

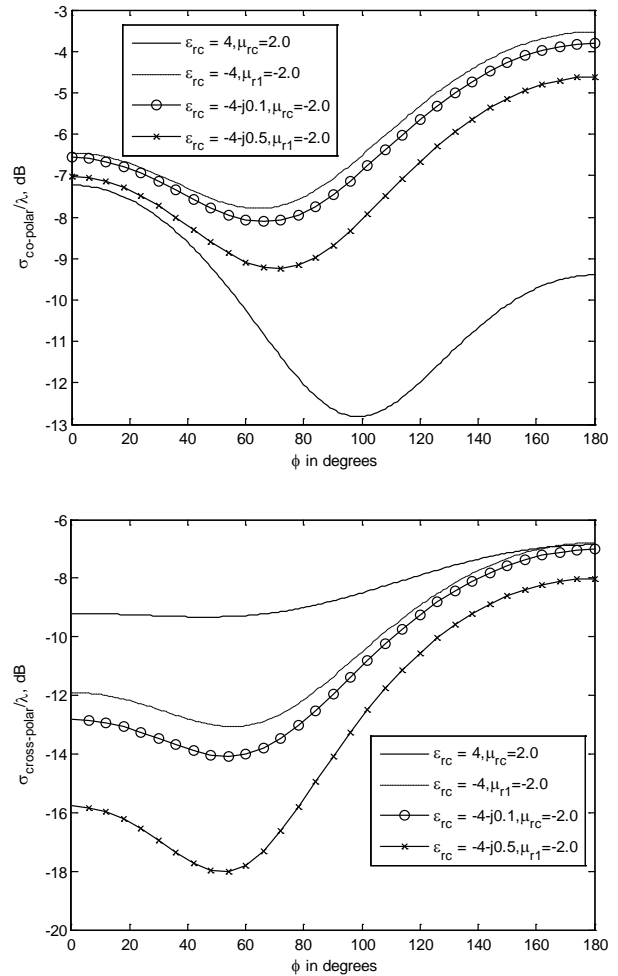


Fig. 3. Echo pattern width versus scattering angle for co and cross polarized chiral lossy metamaterial circular cylinder of $ka=0.5$, axial ratio 1.001, $k\gamma=0.15$ and $\varphi_i = 180^\circ$, TE case.

IV. CONCLUSION

A rigorous solution to the problem of scattering of a plane electromagnetic wave by a chiral lossy and lossless metamaterial circular and elliptic cylinder have been presented using the method of separation of variables. Results have been presented in the form of normalized echo pattern width for circular and elliptic

cylinders of different sizes, axial ratios and chiral and lossy metamaterials, for both TE and TM polarization of the incident wave, to show the effects of the above parameters on scattering from circular and elliptic cylinders. The results obtained in this paper are important, since they can be used as benchmarks to validate similar results obtained using other approximate or numerical methods [15] and also to get an insight into how the changing of various parameters associated with the chiral lossy metamaterial cylinder changes the scattering widths that could be obtained from it.

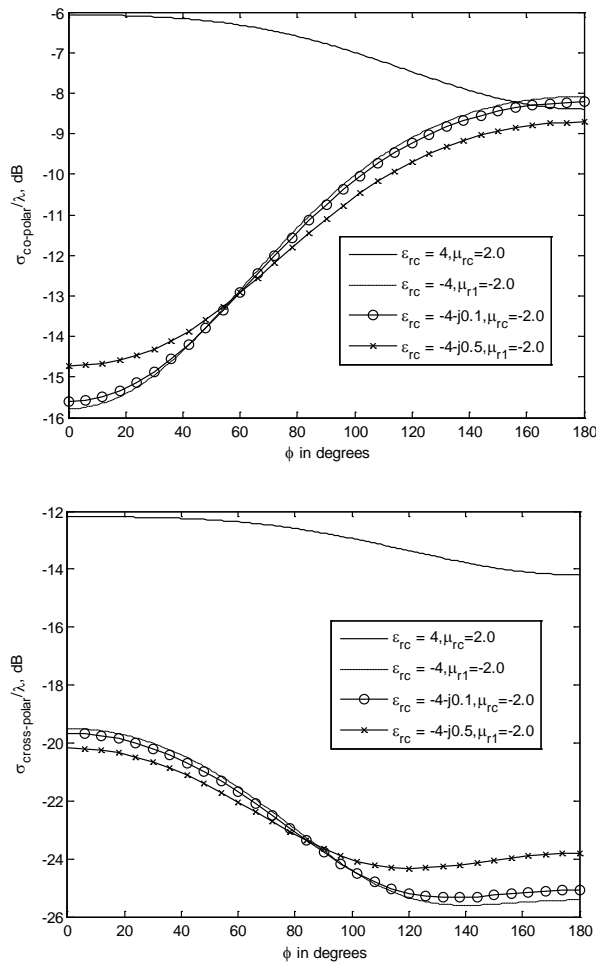


Fig. 4. Echo pattern width versus scattering angle for co and cross polarized chiral lossy metamaterial elliptic cylinder of $ka=0.5$, $kb=0.25$, $k\gamma = 0.15$ and $\varphi_i = 180^\circ$, TM case.

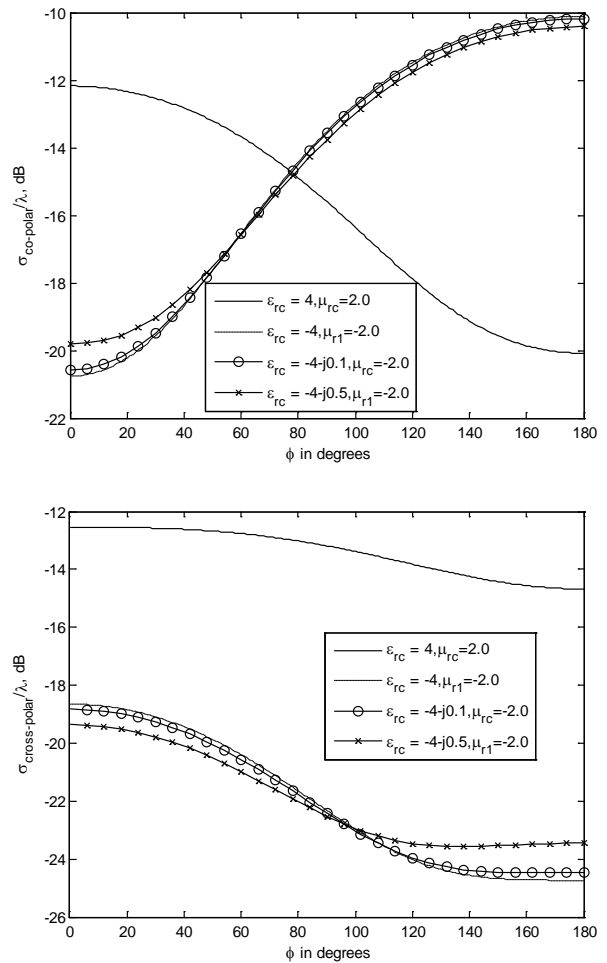


Fig. 5. Echo pattern width versus scattering angle for co and cross polarized chiral lossy metamaterial elliptic cylinder of $ka=0.5$, $kb=0.25$, $k\gamma = 0.15$ and $\varphi_i = 180^\circ$, TE case.

ACKNOWLEDGMENT

Professor A. -K. Hamid wishes to acknowledge the support provided by the University of Sharjah, U.A.E.

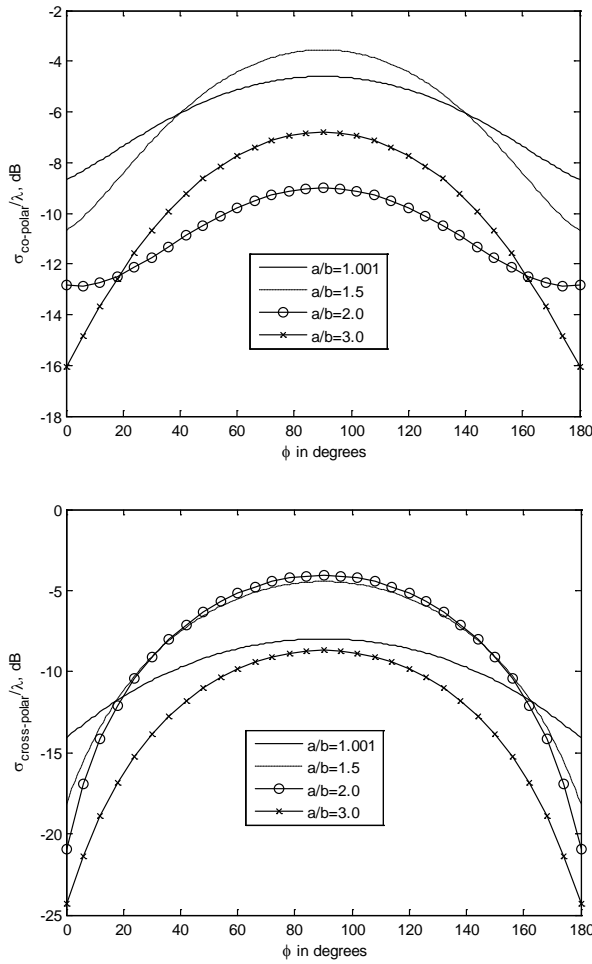


Fig. 6. Echo pattern width versus scattering angle for co and cross polarized chiral lossy metamaterial elliptic cylinder of different axial ratio, $ka=0.5$, $k\gamma=0.15$, $\mu_{rc}=-2.0$, $\epsilon_{rc}=-4.0-j0.5$ and $\varphi_i=90^\circ$, TE case.

REFERENCES

- [1] D. L. Jaggard, A. R. Mickelson, and C. H. Papas, "On Electromagnetic Waves in Chiral Media," *Appl. Phys.*, vol. 18, pp. 211-216, 1979.
- [2] P. L. E. Uslenghi, "Scattering by an Impedance Sphere Coated with a Chiral Layer," *Electromagn.*, vol. 10, pp. 201-211, Jan.-June 1990.
- [3] N. Engheta and P. Pelet, "Modes in Chiro-Waveguides," *Opt. Lett.*, vol. 14, pp. 593-595, June 1989.
- [4] C. Eftimiu and L. W. Pearson, "Guided Electromagnetic Waves in Chiral Media," *Radio Sci.*, vol. 24, pp. 351-359, May-June 1989.

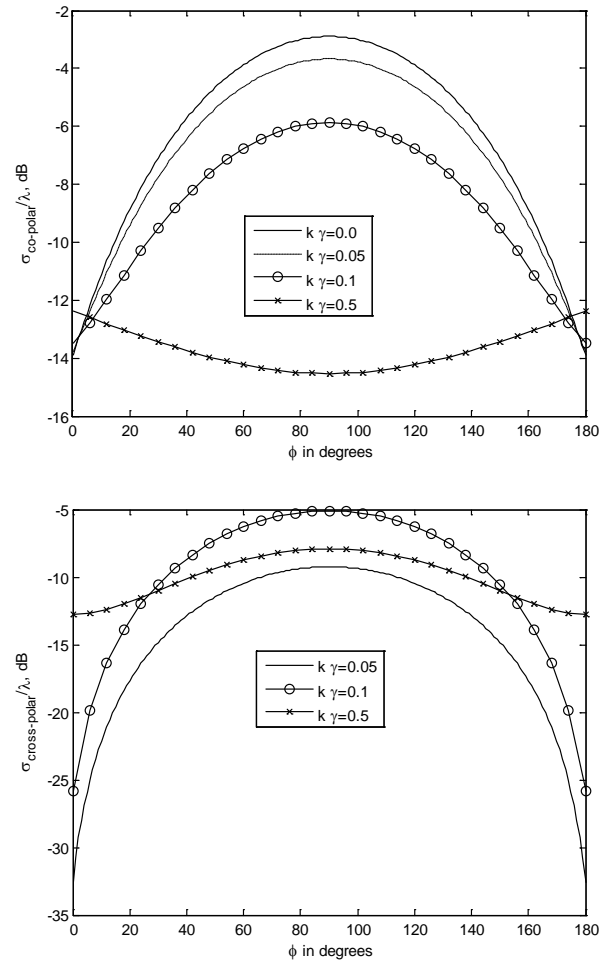


Fig. 7. Echo pattern width versus scattering angle for co and cross polarized chiral lossy metamaterial elliptic cylinder of different $k\gamma$, $ka=0.5$, $kb=0.25$, $\mu_{rc}=-2.0$, $\epsilon_{rc}=-4.0-j0.5$ and $\varphi_i=90^\circ$, TE case.

- [5] N. Engheta and S. Bassiri, "One- and Two-Dimensional Dyadic Green's Functions in Chiral Media," *IEEE Trans. Antennas Propagat.*, vol. 37, pp. 512-515, Apr. 1989.
- [6] W. S. Weiglhofer, "Isotropic Chiral Media and Scalar Hertz Potentials," *J. Phys. A*, vol. 21, pp. 2249-2251, 1988.
- [7] N. Engheta and D. L. Jaggard, "Electromagnetic Chirality and its Applications," *IEEE Antennas Propagat. Soc. Newsletter*, vol. 30, pp. 6-12, Oct. 1988.
- [8] S. Bassiri, C. H. Papas, and N. Engheta, "Electromagnetic Wave Propagation through a Dielectric-Chiral Interface and through a Chiral Slab," *J. Opt. Soc. Am. A*, vol. 5, pp. 1450-1459, Sept. 1988.

- [9] D. L. Jaggard, X. Sun, and N. Engheta, "Canonical Sources and Duality in Chiral Media," *IEEE Trans. Antennas Propagat.*, vol. 36, pp. 1007-1013, July 1988.
- [10] A. Lakhtakia, V. V. Varadan, and V. K. Varadan, "Field Equations, Huygens's Principle, Integral Equations, and Theorems for Radiation and Scattering of Electromagnetic Waves in Isotropic Chiral Media," *J. Opt. Soc. Am. A*, vol. 5, pp. 175-184, Feb. 1988.
- [11] A. Lakhtakia, V. V. Varadan, and V. K. Varadan, "Radiation by a Straight Thin-Wire Antenna Embedded in an Isotropic Chiral Media," *IEEE Trans. Electromagn. Compat.*, vol. 30, pp. 84-87, Feb. 1988.
- [12] M. S. Kluskens and E. H. Newman, "Scattering by a Multilayer Chiral Cylinder," *IEEE Trans. Antennas Propagat.*, vol. 39, pp. 91-96, 1991.
- [13] A. Z. Elsherbeni, M. H. Al Sharkawy, and S. F. Mahmoud, "Electromagnetic Scattering from a 2-D Chiral Strip Simulated by Circular Cylinders for Uniform and Nonuniform Chirality Distribution", *IEEE Trans. Antennas Propagat.*, vol. 52, no. 9, pp. 2244-2252, 2004.
- [14] S. Ahmed and Q. A. Naqvi, "Electromagnetic Scattering from a Chiral Coated Nihility Cylinder," *Progress In Electromagnetics Research Letters*, vol. 18, pp. 41-50, 2010.
- [15] R. Rojas, "Integral Equations for EM Scattering by Homogeneous /Inhomogeneous Two-Dimensional Chiral Bodies", *Inst. Elect. Eng. Microw., Antennas Propag.*, vol. 141, pp. 385-392, 1994.
- [16] M. A. Al-Kanhal and E. Arvas, "Electromagnetic Scattering from a Chiral Cylinder of Arbitrary Cross Section," *IEEE Trans. Antennas Propag.*, vol. 44, no. 7, pp. 1041-1049, Jul. 1996.
- [17] A. Semichaevsky, A. Akyurtlu, D. Kern, D. H. Werner, and M. G. Bray, "Novel BI-FDTD Approach for the Analysis of Chiral Cylinders and Spheres", *IEEE Trans. Antennas Propagat.*, vol. 54, no. 3, pp. 925-932, 2006.
- [18] A. M. Attiya, "Coupled Mode Analysis of Two-Dimensional Chiral Grating," *Applied Computational Electromagnetics Society (ACES) Journal*, vol. 26, no. 4, pp. 303-311, April 2011.
- [19] S. T. Imeci, F. Altunkilic, J. R. Mautz, and E. Arvas, "Transmission through an Arbitrarily Shaped Aperture in a Conducting Plane Separating Air and a Chiral Medium," *Applied Computational Electromagnetics Society (ACES) Journal*, vol. 25, no. 7, pp. 587-599, July 2010.
- [20] B. N. Khatir, M. Al-Kanhal, and A. Sebak, "Electromagnetic Wave Scattering by Elliptic Chiral Cylinder," *Journal of Electromagnetic Waves and Applications*, vol. 20, no. 10, pp. 1377-1390, 2006.
- [21] B. N. Khatir and A. R. Sebak, "Slot Antenna on a Conducting Elliptic Cylinder Coated by Chiral Media," *Electromagnetics*, vol. 29, no. 7, pp. 522-540, 2009.
- [22] B. N. Khatir and A. R. Sebak, "Slot Antenna on a Conducting Elliptic Cylinder Coated by Nonconfocal Chiral Media," *Progress in Electromagnetics Research*, vol. 93, pp. 125-143, 2009.
- [23] A. -K. Hamid, "EM Scattering by a Lossy Dielectric-Coated Nihility Elliptic Cylinder", *Applied Computational Electromagnetics Society (ACES) Journal*, vol. 25, pp. 444-449, 2010.
- [24] A. -K. Hamid and F. R. Cooray, "Scattering by a Perfect Electromagnetic Conducting Elliptic Cylinder", *Progress in Electromagnetic Research, PIER*, vol. 10, pp. 59-67, 2009.



A-K. Hamid was born in Tulkarm, on Sept. 9, 1963. He received the B.Sc. degree in Electrical Engineering from West Virginia Institute of Technology and university, West Virginia, U.S.A. in 1985. He received the M.Sc. and Ph.D. degrees from the University of Manitoba, Winnipeg, Manitoba, Canada in 1988 and 1991, respectively, both in Electrical Engineering. From 1991-1993, he was with Quantic Laboratories Inc., Winnipeg, Manitoba, Canada, developing two and three dimensional electromagnetic field solvers using boundary integral method. From 1994-2000, he was with the faculty of electrical engineering at King Fahd University of Petroleum and Minerals, Dhahran, Saudi Arabia. Since Sept. 2000, he is with the Electrical and Computer Engineering at the University of Sharjah, Sharjah, United Arab Emirates. His research interest includes EM wave scattering from two and three dimensional bodies, propagation along waveguides with discontinuities, FDTD simulation of cellular phones, and inverse scattering using neural networks.

Effects of Surface Roughness on Lossy Rectangular Waveguide

Juan Chen and Binke Huang

School of Electronic and Information Engineering, Xi'an Jiaotong
University, Xi'an 710049, China
chenjuan0306@yahoo.com.cn

Abstract — The integral equation method combined with the surface-impedance boundary condition is applied for the analysis of propagation characteristics of rough lossy metal waveguides. The surface roughness of waveguide is random, and the statistical properties associated to the wall roughness are consistent with a Gaussian random process. The effects of the waveguide parameters on the propagation constant and attenuation constant are discussed rigorously, including the frequency, the standard deviation of height and correlation length of the Gaussian roughness. The results show that, as the increases of correlation length and frequency, the propagation constant is increased and the attenuation constant is decreased; while as the increase of the standard deviation, the trends of the propagation constant and the attenuation constant are just opposite.

Index Terms — Gaussian random process, integral equation, rectangular waveguide, rough surface, surface-impedance boundary.

I. INTRODUCTION

The surface roughness of waveguide is a practical reality. It may occur due to various reasons, such as polishing of irregular waveguide structures, uneven surface coating or corrugation of surface while fabricating the waveguides. The problem of roughness may also arise due to exposure of waveguide to environment. The environmental corrosion increases with ageing which results in increasing roughness of waveguide walls. The surface roughness will affect the propagation constant and attenuation constant of the waveguide, and change the cutoff frequency of every waveguide mode [2], so, it becomes very important to study the effect of

surface roughness on electromagnetic wave propagation.

There have been many numerical techniques presented to study the effect of surface roughness on waveguide [1-9], including full-wave mode-matching method [1], finite element method [2], moments method [3-5], and finite-difference frequency-domain method [6,7]. In [2], the effect of surface roughness on TE₁₀, TE₂₀ mode cutoff frequencies and passbands is studied. In [3], the calculation for TM modes in waveguides with polygonal and fractal cross-sectional shapes is presented; in [4], the case for TE waves of waveguides with inner polygonal structure is considered. Based on the numerical techniques of [3, 4]. In [5], a scheme to generate an ensemble of realizations for wall Gaussian random rough profiles in circular waveguide is proposed, but without considering the attenuation of the lossy metal. The finite-difference frequency-domain method to compute the lossy metal waveguides is used in [6, 7]. In this method, the surface-impedance boundary condition (SIBC) is applied for lossy metal structures. By solving the Eigen equation, the phase constants and attenuation constants can be found for a given frequency. However, this method is confined to solve the regular surface roughness waveguide. In practice, most waveguide is made of imperfect conductor, and is with random surface roughness. Thus, a numerical method which can be applied to simulate the random rough lossy waveguide becomes important.

In this paper, a new integral equation method is presented for the analysis of propagation characteristics of rough lossy metal waveguides. The surface roughness of waveguide is random, and the statistical properties associated to the wall

roughness are consistent with a Gaussian random process. The attenuation of the imperfect conductor is considered by using the surface-impedance boundary condition. The validity of this numerical technique to simulate the case of rough waveguide is confirmed by a comparison with previous results.

The advantage of this integral equation method is that it can be used to analyze the random rough lossy waveguide and compared with the full wave methods, such as the FDTD method and MOM method, this method is easy to program. By using this integral equation method, the effects of the waveguide parameters on the propagation constant and attenuation constant are discussed rigorously, including the conductivity of the lossy metal, the standard deviation of height and correlation length of the Gaussian roughness. Some useful conclusions are reached.

This paper is organized as follows. The numerical technique applicable to calculations of rough lossy waveguides is presented first; then, the validity of the approach is tested by a comparison with previous results. After that, the effects of the parameters of the roughness on the propagation constant and attenuation constant are discussed; and some useful conclusions are reached.

II. NUMERICAL TECHNIQUE

A cylindrical surface S of general cross-sectional contour is shown in Fig. 1. The cross-sectional size and shape are assumed constant along the cylinder axis (z direction), and the intersection of the cylinder with the $x-y$ plane is the closed profile C . We have assumed that the inner space of the cylinder be vacuum.

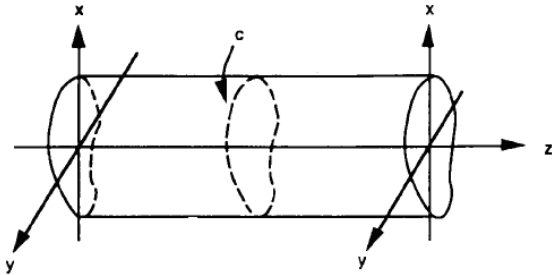


Fig. 1. Hollow cylindrical waveguide of arbitrary cross-sectional shape.

It is a well-known fact that if we assume a sinusoidal time dependence $e^{-i\omega t}$ for the fields

inside the cylindrical waveguide, the basic problem reduces to finding the eigen values γ and the corresponding eigen functions $\psi_\gamma(x, y)$, which represent modes of the electric field E_z (TM-waves) or of the magnetic field H_z (TE-waves). To find these modes, we need to solve the two-dimensional Helmholtz equation,

$$\left(\nabla_T^2 + \gamma^2\right)\psi_\gamma(x, y) = 0. \quad (1)$$

∇_T^2 is given by

$$\nabla_T^2 = \nabla^2 - \partial^2/\partial z^2. \quad (2)$$

The parameter γ can be expressed as,

$$\gamma^2 = \frac{\omega^2}{c^2} + k_z^2, \quad (3)$$

where c is light velocity, k_z is the wavevector component of the electromagnetic wave propagating along the axis of the waveguide.

We introduce a Green's function $G_\gamma(r, r')$, which is the solution of the two-dimensional inhomogeneous Helmholtz equation,

$$\left(\nabla_T^2 + \gamma^2\right)G_\gamma(r, r') = -4\pi\delta(r - r') \quad (4)$$

where $r = (x, y)$ and $r' = (x', y')$. The Green's function can be expressed in terms of a Hankel function as follows:

$$G_\gamma(r, r') = i\pi H_0^{(1)}(\gamma|r - r'|) \quad (5)$$

Applying Green's integral theorem to the functions $\psi_\gamma(r)$ and $G_\gamma(r, r')$, it obtains,

$$\psi_\gamma(r) = \frac{1}{4\pi} \oint_C \left[G_\gamma(r, r') \frac{\partial}{\partial n} \psi_\gamma(r') - \psi_\gamma(r') \nabla' G_\gamma(r, r') \cdot \vec{n} \right] ds \quad (6)$$

where, \vec{n} is the unitary vector normal to each point on C outward.

Considering the finite conductivity of the metal waveguide, we apply the surface-impedance boundary condition along the profile C .

$$E_{tan} = Z_s \vec{n} \times H_{tan} \quad (7)$$

For lossy metal waveguides, $Z_s = (1 + i)/\delta\sigma$, with δ the skin depth, σ the conductivity of metal, and index tan the tangential field components around profile C .

For the TE-waves, $\psi_\gamma = H_z, E_z = 0$. Applying equation (7), we have,

$$\psi_\gamma Z_s = \frac{i\omega\mu}{\gamma^2} \frac{\partial \psi_\gamma}{\partial n}. \quad (8)$$

Introducing equation (8) into equation (6), it obtains,

$$\psi_\gamma(r) = \frac{1}{4\pi} \oint_c \left[G_\gamma(r, r') Z_{TE} \right] \psi_\gamma(r') ds \quad (9)$$

where,

$$Z_{TE} = \frac{Z_s \gamma^2}{i\omega\mu} \quad (10)$$

with the same manipulation, the integral equation for the TM-waves is,

$$\psi_\gamma(r) = \frac{1}{4\pi} \oint_c \left[G_\gamma(r, r') Z_{TM} \right] \psi_\gamma(r') ds \quad (11)$$

with,

$$Z_{TM} = \frac{i\gamma^2}{Z_s \omega \epsilon} \quad (12)$$

To determine the Eigen values γ and the correspondence source functions $\psi_\gamma(r)$, we convert the integral equations (9) and (11) into a matrix equation by using a simple rectangular approximation to evaluate the integrals over small intervals. This matrix equation can then be solved numerically.

The matrix equation for the source function $\psi_\gamma(r)$, is given by,

$$0 = \sum_{n=1}^N L_{mn}^\gamma \psi_\gamma^n \quad m = 1, 2, \dots, N \quad (13)$$

where, $\psi_\gamma^n = \psi_\gamma(r)|_{r=r(c_n)}$ and $r(c_1), r(c_2), \dots, r(c_N)$ are N equally spaced points on the contour. The explicit expression for the matrix elements can be obtained [5],

$$L_{mn}^\gamma = \left[\begin{array}{c} \frac{i\Delta s}{4} H_0^{(1)}(\gamma d_{mn})(1 - \delta_{mn}) \\ -\frac{\Delta s}{4i} H_0^{(1)}\left(\gamma \frac{\Delta s}{2e}\right) \delta_{mn} \end{array} \right] Z$$

$$-\frac{i\Delta s}{4} \left\{ \gamma \frac{H_1^{(1)}(\gamma d_{mn})}{d_{mn}} \times \begin{pmatrix} X_n' [Y_m - Y_n] \\ -Y_n' [X_m - X_n] \end{pmatrix} \right\} (1 - \delta_{mn}) \\ + \left\{ \frac{1}{2} - \frac{\Delta s}{4\pi} (X_n' Y_n'' - X_n'' Y_n') \right\} \delta_{mn} \quad (14)$$

with

$$d_{mn} = \left\{ [X_m - X_n]^2 + [Y_m - Y_n]^2 \right\}^{1/2},$$

where Δs is the distance on curve C between $r(c_j)$ and $r(c_{j+1})$,

with $j = 1, 2, \dots, N - 1$; (X_m, Y_m) are the Cartesian components of the vector $r(c_m)$, and

$H_1^{(1)}(z)$ is a Hankel functions of first order; each prime symbol denotes a derivative. For the TE and TM-waves, $Z = Z_{TE}$ and Z_{TM} , respectively.

As can be observed from equation (13), the matrix equation is homogeneous; thus, the values of γ can be determined from the condition,

$$|L_{mn}^\gamma| = 0 \quad (15)$$

We define the function

$$D(\gamma) = \ln(|L_{mn}^\gamma|) \quad (16)$$

considering that the logarithm function is appropriately convenient. Because of numerical limitations, condition (15) is satisfied approximately for eigenvalues $\gamma_1, \gamma_2, \dots$, where $D(\gamma_1), D(\gamma_2), \dots$ are minima of the $D(\gamma)$ function.

The source function ψ_γ^n can be determined by using a singular-value-decomposition numerical technique [8], with use of equation (13), which represents a set of homogeneous equations, where the matrix L_{mn}^γ is numerically close to singular.

Once γ and the source function ψ_γ^n have been determined, the field amplitude in the cylinder can be calculated,

$$\psi_\gamma(x, y) = \frac{i\Delta s}{4} \sum_{n=1}^N \psi_\gamma^n \left(\begin{matrix} H_0^{(1)}(\gamma d_n) Z \\ -\gamma \frac{H_1^{(1)}(\gamma d_n)}{d_n} \times \begin{pmatrix} x_n [y - y_n] \\ -y_n [x - x_n] \end{pmatrix} \end{matrix} \right) \quad (17)$$

with $d_n = \left\{ [x - x_n]^2 + [y - y_n]^2 \right\}^{1/2}$.

III. VALIDATION

In this section, the numerical technique presented above is validated by a comparison with previous results.

A metal rectangular waveguide with width $a = 19.05$ mm, height $b = 9$ mm, and conductivity $\sigma = 5.8 \times 10^7$ S/m (the conductivity of copper) is considered [7]. Wavevector component $k_z = \alpha + j\beta$, with β the propagation constant, and α the attenuation constant. The numerical results of β and α with respect to frequency calculated by the integral equation method are presented in Fig. 2 and 3. For comparison, the results of [7] are also shown in these figures. It can be seen from these figures that, the numerical results calculated by using the integral equation method agree well with the results of [7].

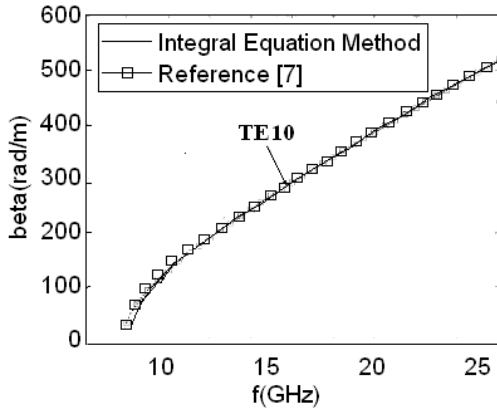


Fig. 2. Propagation constant β of a metal empty rectangular waveguide.

IV. DISCUSSION

By using the numerical technique presented above, we discuss the effects of the waveguide parameters on the propagation constant and

attenuation constant, including the conductivity σ of the lossy metal, the standard deviation of height D and correlation length l_{co} of the Gaussian roughness. The ensembles of profiles with these statistical properties are generated by using the method presented in [5]. Considering the randomness, we take into account one hundred realizations for a calculation; then, we get the statistical average value of these results.

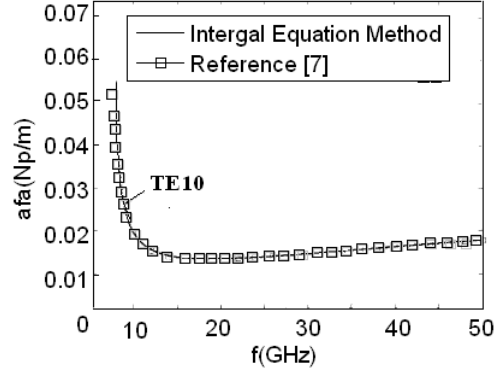


Fig. 3. Attenuation constant α of a metal empty rectangular waveguide.

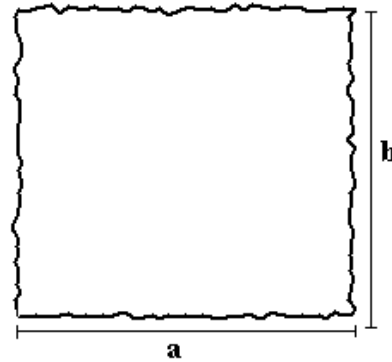


Fig. 4. Simplified model for rectangular waveguides with Gaussian rough surface

The dimension of the rough waveguide is $a = b = 8$ mm, as shown in Fig. 4. In this figure, both the standard deviation of height D and correlation length l_{co} are equal to 0.01mm.

A. Effect of the conductivity σ

Supposing the waveguide is regular ($D = 0$), and keeping the work frequency unchanged, by using the integral equation method, we can get the variations of the propagation constant β and attenuation constant α with respect to waveguide

conductivity σ , as shown in Figs. 5 and 6. Here, we consider the first four modes of the regular waveguide: TE₁₀, TE₁₁, TM₁₁, and TM₂₁ modes.

It can be seen from Fig. 5, that as the increase of the conductivity σ , the propagation constants β of the TE modes are increased, and the propagation constants β of the TM modes are decreased. The attenuation constants α , both for the TE modes and TM modes, are all decreased as the increase of conductivity σ , as shown in Fig. 6. Besides, it can be seen from these two figures that when the conductivity σ increase to 75dbS/m (about 5.8×10^7 s/m, the conductivity of copper), the variations of the propagation constant β and attenuation constant α with respect to conductivity σ are not obvious, which means that, when exceeding the conductivity of copper, the effect of σ on the propagation performance of the waveguide is not considerable.

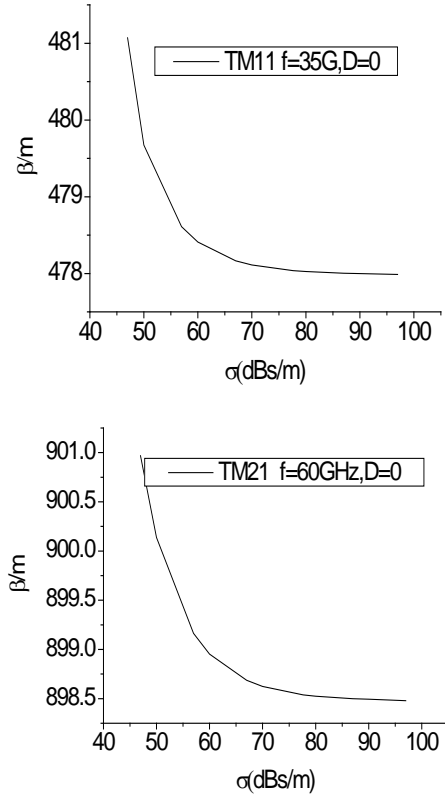
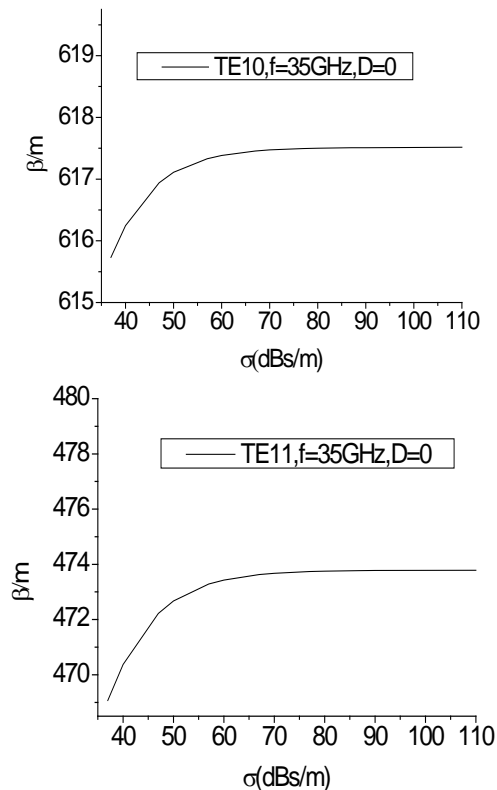


Fig. 5. The variations of the propagation constant β with respect to conductivity σ .

B. Effect of the standard deviation of height D

We let the conductivity of the waveguide $\sigma = 5.8 \times 10^7$ S/m, the correlation length $l_{co} = 0.05$, and keep the work frequency unchanged. In this section, we discuss the effects of the standard deviation of height D of the Gaussian rough waveguide on the propagation constant β and attenuation constant α .

By using the integral equation method, we can get the variations of propagation constant β and attenuation constant α with respect to standard deviation of height D , as shown in Figs. 7 and 8. It can be seen from these two figures that, as the increase of D , for both the TE and TM modes, the propagation constants β are decreased and the attenuation constants α are increased.

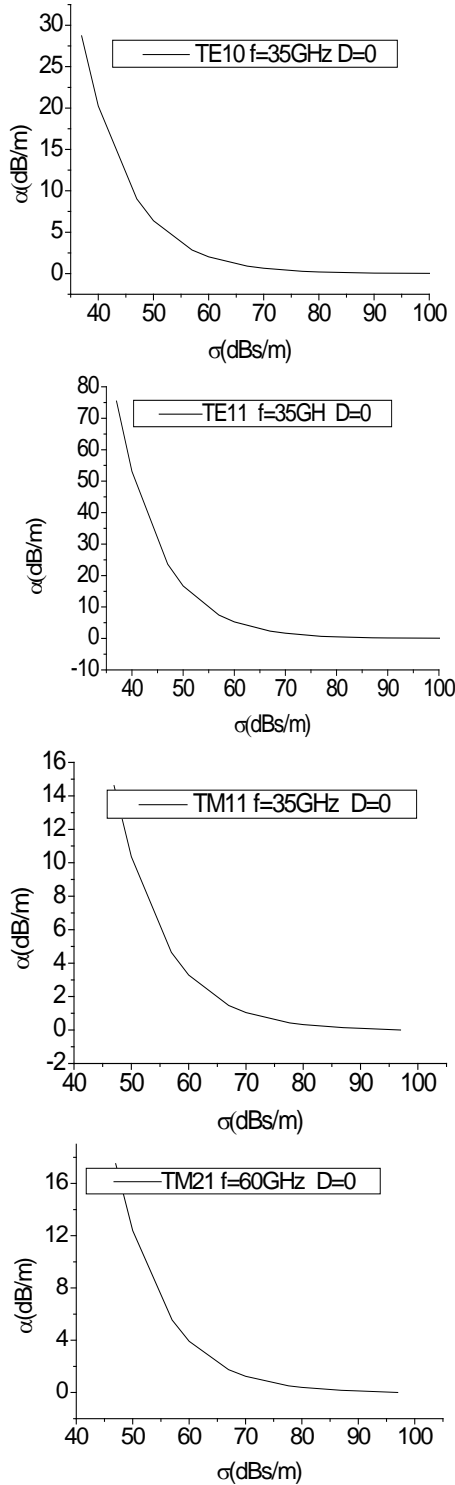
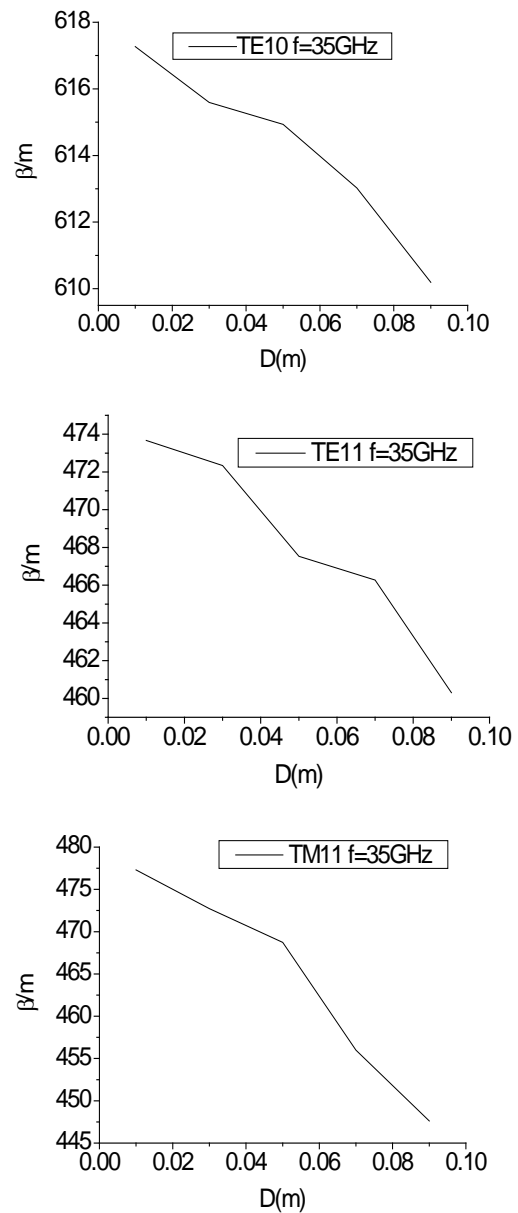


Fig. 6. The variations of attenuation constant α with respect to conductivity σ .

C. Effect of the correlation length l_{co}

Supposing the conductivity of the waveguide $\sigma = 5.8 \times 10^7$ S/m, standard deviation of

height $D=0.03$, and keeping the work frequency unchanged, by using the integral equation method, we can get the propagation constant β and attenuation constant α for different correlation length l_{co} , as shown in Figs. 9 and 10. It can be seen from these figures that, as the increase of l_{co} , for both the TE and TM modes, the propagation constants β are increased and the attenuation constants α are decreased.



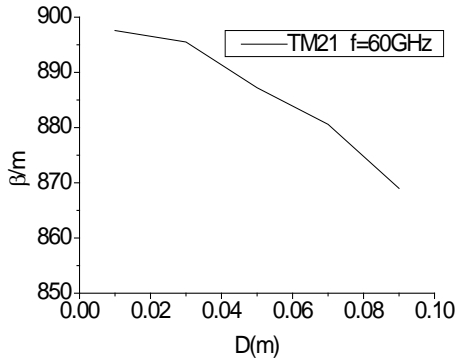


Fig. 7. The variations of the propagation constant β with respect to standard deviation of height D .

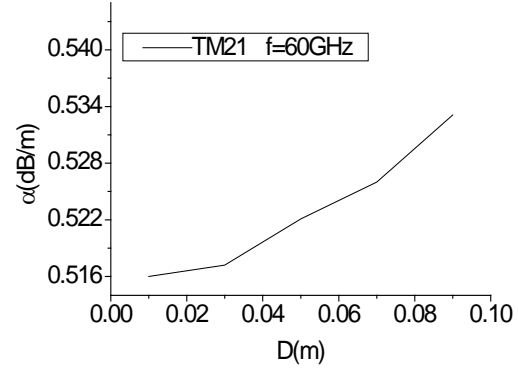
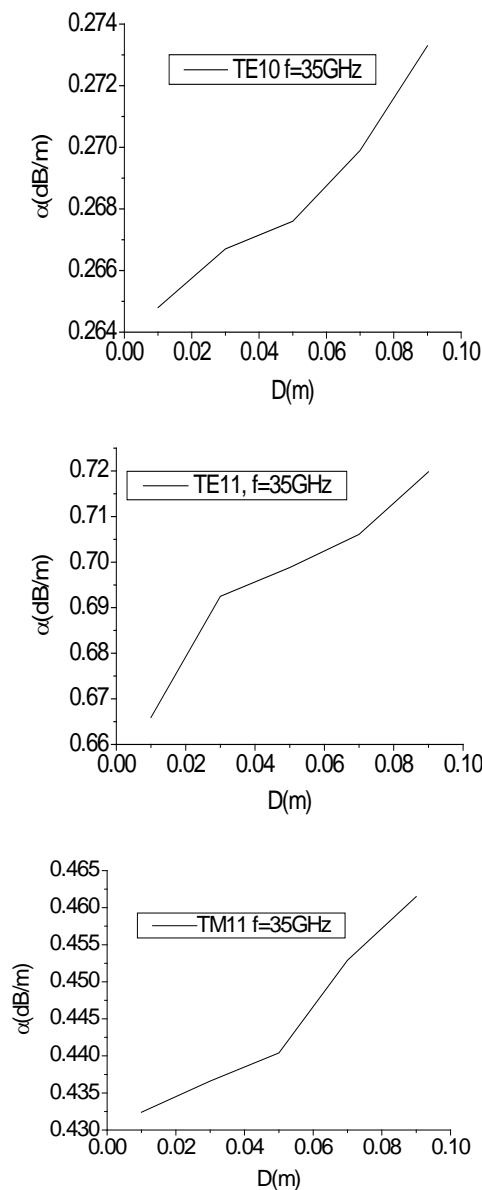


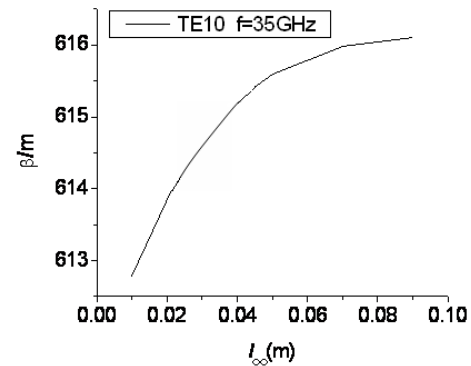
Fig. 8. The variations of attenuation constant α with respect to standard deviation of height.



D. Effect of work frequency f

To discuss the effect of the work frequency f on the propagation constant β and attenuation constant α , we suppose conductivity of the waveguide $\sigma = 5.8 \times 10^7$ S/m, standard deviation of height $D=0.03$, and correlation length $l_{co}=0.05$. The variations of propagation constant β and attenuation constant α with respect to frequency f are shown in Figs. 11 and 12. Obviously, as the increase of f , the propagation constants β are increased and the attenuation constants α are decreased.

The dotted lines in Fig. 12 represent the variations of attenuation constant α with respect to work frequency in a smooth waveguide for every mode. It can be seen from this figure that, the variations of attenuation constant with respect to work frequency f for the rough waveguide is the same as that for the smooth waveguide.



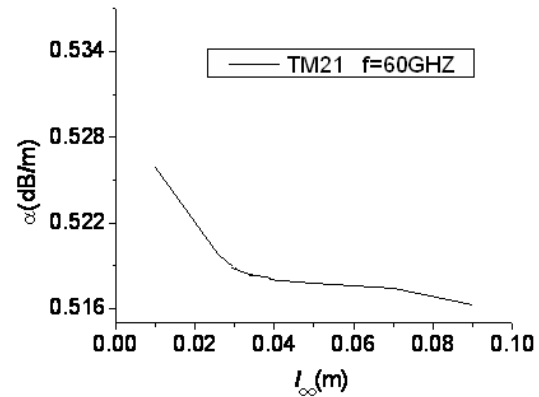
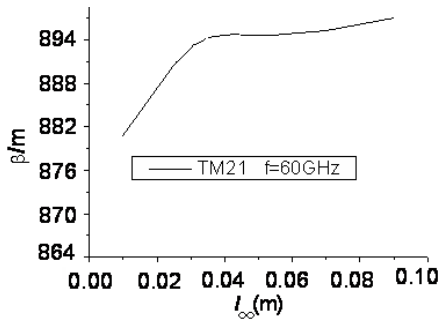
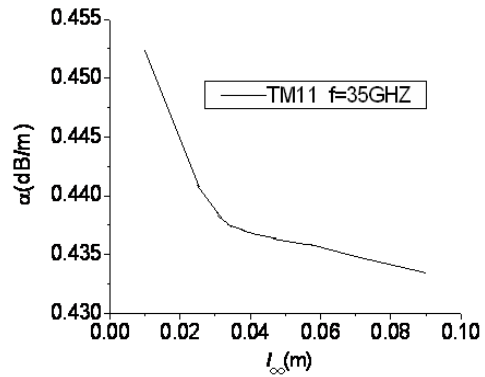
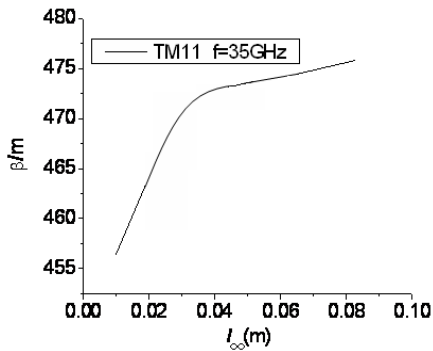
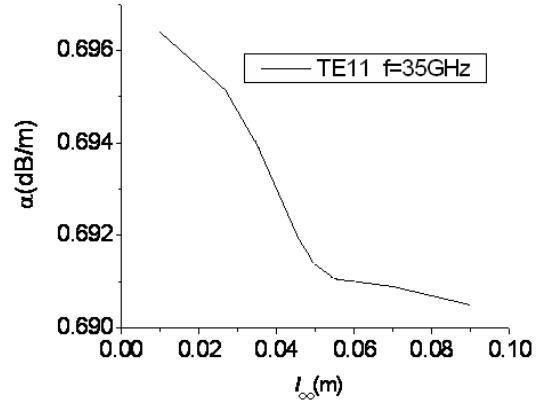
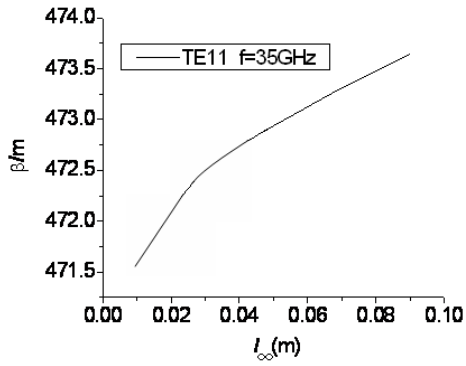
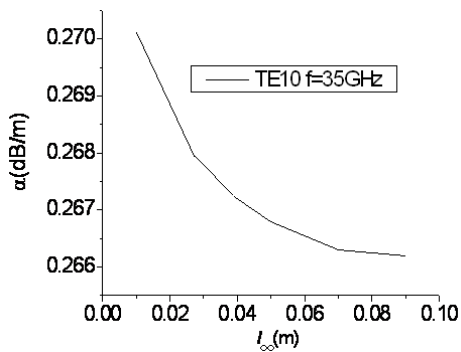


Fig. 9. The variations of the propagation constant β with respect to correlation length l_{co} .

Fig. 10. The variations of attenuation constant α with respect to correlation length l_{co} .



The discrepancy of the propagation constant β between perfect conductor waveguide and copper waveguide is defined as,

$$\beta_{er} = \frac{|\beta^p - \beta^c|}{\beta^p}, \quad (18)$$

where β^p, β^c is the propagation constant of perfect conductor waveguide and copper waveguide calculated by using integral equation method, respectively.

Similarly, the discrepancy of the attenuation constant α is defined as,

$$\alpha_{er} = \frac{|\alpha^p - \alpha^c|}{\alpha^p}, \quad (19)$$

For TE10, TE11, TM11, and TM21 modes, the β_{er} and α_{er} for different work frequency f are shown in Tables 1-4. It can be seen from these tables that, for all the modes, the discrepancies of β and α between perfect conductor waveguide and copper waveguide are decreased as the increase of the frequency f , which means that the effect of the loss metal on the propagation performance of the waveguide is decreased as the increase of frequency f .

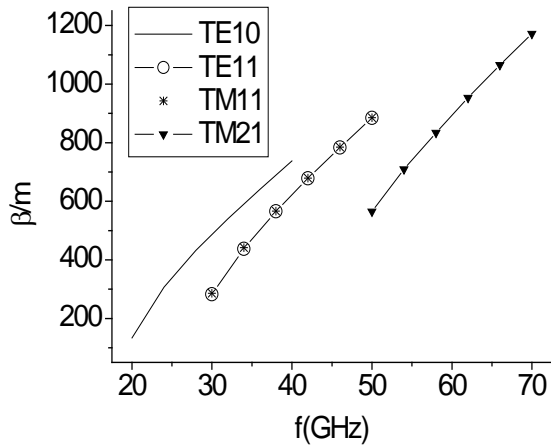


Fig. 11. The variations of the propagation constant β with respect to work frequency f

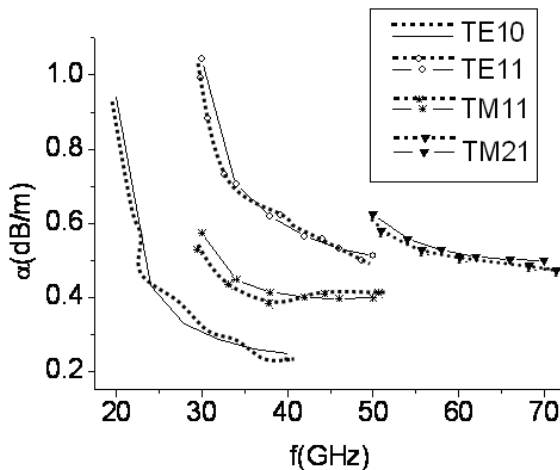


Fig. 12. The variations of attenuation constant α with respect to work frequency f

Table 1: The β_{er} and α_{er} of TE10 mode for different work frequency

f (GHz)	β_{er} (%)	α_{er} (%)
20	3.18	3.79
24	0.99	2.27
28	0.23	1.65
32	0.18	0.88
36	0.16	0.71
40	0.14	0.69

Table 2: The β_{er} and α_{er} of TE11 mode for different work frequency

f (GHz)	β_{er} (%)	α_{er} (%)
30	1.12	2.19
34	0.73	1.81
38	0.24	0.59
42	0.16	0.55
46	0.16	0.40
50	0.15	0.33

Table 3: The β_{er} and α_{er} of TM11 mode for different work frequency

f (GHz)	β_{er} (%)	α_{er} (%)
30	2.30	2.41
34	0.76	0.79
38	0.65	0.68
42	0.42	0.43
46	0.33	0.35
50	0.28	0.28

Table 4: The β_{er} and α_{er} of TM21 mode for different work frequency

f (GHz)	β_{er} (%)	α_{er} (%)
50	0.71	0.74
54	0.57	0.58
58	0.53	0.54
62	0.30	0.31
66	0.21	0.21
70	0.21	0.21

V. CONCLUSION

An integral equation method has been performed to evaluate the propagation characteristic of the random rough lossy waveguide. It has been shown that the propagation characteristic strongly depends on the frequency, the standard deviation of height and correlation length. As the correlation length and frequency increases, the propagation constant is increased and the attenuation constant is decreased; while as the increase of the standard deviation, the trends of the propagation constant and the attenuation constant are just opposite. Those results may have interesting applications for optical telecommunication and hollow dielectric film coated waveguide for THz radiation.

ACKNOWLEDGMENT

This work was supported by National Natural Science Foundations of China (No. 61001039), and also supported by the Research Fund for the Doctoral Program of Higher Education of China (20090201120030).

REFERENCES

- [1] C. D. Chen, C. K. C. Tzuang, and S. T. Peng, "Full-Wave Analysis of a Lossy Rectangular Waveguide Containing Rough Inner Surfaces," *IEEE Microwave Guided Wave Lett.*, vol. 2, pp. 0-181, 1999.
- [2] S. K. Popalghat, A. Chaudhari, and P. B. Patil, "Effect of Surface Roughness on Electromagnetic Propagation through Waveguides," *Indian Journal of pure & Applied Physics*, vol. 37, pp. 48-852, 1999.
- [3] A. M. Sua´rez, R. E. Luna, J. C. Mandujano, and J. E. Luna, "Numerical Technique to Calculate Modes in Waveguides of Arbitrarily Cross-Sectional Shape," *J. Opt. Soc. Am. A*, vol. 18, pp. 961-965, 2001.
- [4] G. A. Rubioa, A. M. Sua´rez, R.E. Lunaa, and E. T. Herna´ndezb, "Application of a New Numerical Method to Calculate TE Modes in Hollow-Conducting Waveguides," *Optical Communications*, vol. 221, pp. 301-306, 2003.
- [5] A. M. Sua´rez, U. R. Corona, and R. E. Luna, "Effects of Wall Random Roughness on TE and TM Modes in a Hollow Conducting Waveguide," *Optical Communications*, vol. 238, pp. 291-299, 2004.
- [6] Y. J. Zhao, K. L. Wu, and K. K. M. Cheng, "A Compact 2-D Full-Wave Finite-Difference Frequency-Domain Method for General Guided Wave Structures," *IEEE Trans. Microwave Theory Tech.*, vol. 50, pp. 1844-1848, 2002.
- [7] J. Li, L. X. Guo, and H. Zeng, "FDTD Investigation on Electromagnetic Scattering from Two-Dimensional Layered Rough Surfaces," *Applied Computational Electromagnetics Society (ACES) Journal*, vol. 25, pp. 450-457, May 2010.
- [8] L. D. Rienzo, N. Ida, and S. Yuferev, "Surface Impedance Boundary Conditions of High Order of Approximation for the Finite Integration Technique," *Applied Computational Electromagnetics Society (ACES) Journal*, vol. 22, pp. 53-59, Mar. 2007.
- [9] B. Z. Wang, X. HW, and W. Shao, "2D Full-Wave Finite-Difference Frequency-Domain Method for Lossy Metal Waveguide," *Microw. Opt. Tech.. lett.*, vol. 42, pp. 158-161, 2004.
- [10] W. H. Press, S. A. Teukolsky, W. T. Vetterling, and B. P. Flannery, *Numerical Recipes in FORTRAN*, Cambridge University Press, Cambridge, UK, 1992.

2012 INSTITUTIONAL MEMBERS

DTIC-OCP LIBRARY
8725 John J. Kingman Rd, Ste 0944
Fort Belvoir, VA 22060-6218

AUSTRALIAN DEFENCE LIBRARY
Northcott Drive
Canberra, A.C.T. 2600 Australia

BEIJING BOOK CO, INC
701 E Linden Avenue
Linden, NJ 07036-2495

DARTMOUTH COLLEGE
6025 Baker/Berry Library
Hanover, NH 03755-3560

DSTO EDINBURGH
AU/33851-AP, PO Box 830470
Birmingham, AL 35283

SIMEON J. EARL – BAE SYSTEMS
W432A, Warton Aerodome
Preston, Lancs., UK PR4 1AX

ENGINEERING INFORMATION, INC
PO Box 543
Amsterdam, Netherlands 1000 Am

ETSE TELECOMUNICACION
Biblioteca, Campus Lagoas
Vigo, 36200 Spain

GA INSTITUTE OF TECHNOLOGY
EBS-Lib Mail code 0900
74 Cherry Street
Atlanta, GA 30332

TIMOTHY HOLZHEIMER
Raytheon
PO Box 1044
Rockwall, TX 75087

HRL LABS, RESEARCH LIBRARY
3011 Malibu Canyon
Malibu, CA 90265

IEE INSPEC
Michael Faraday House
6 Hills Way
Stevenage, Herts UK SG1 2AY

INSTITUTE FOR SCIENTIFIC INFO.
Publication Processing Dept.
3501 Market St.
Philadelphia, PA 19104-3302

LIBRARY – DRDC OTTAWA
3701 Carling Avenue
Ottawa, Ontario, Canada K1A OZ4

LIBRARY of CONGRESS
Reg. Of Copyrights
Attn: 407 Deposits
Washington DC, 20559

LINDA HALL LIBRARY
5109 Cherry Street
Kansas City, MO 64110-2498

MISSOURI S&T
400 W 14th Street
Rolla, MO 56409

MIT LINCOLN LABORATORY
Periodicals Library
244 Wood Street
Lexington, MA 02420

NATIONAL CHI NAN UNIVERSITY
Lily Journal & Book Co, Ltd
20920 Glenbrook Drive
Walnut, CA 91789-3809

JOHN NORGARD
UCCS
20340 Pine Shadow Drive
Colorado Springs, CO 80908

OSAMA MOHAMMED
Florida International University
10555 W Flagler Street
Miami, FL 33174

NAVAL POSTGRADUATE SCHOOL
Attn:J. Rozdal/411 Dyer Rd./ Rm 111
Monterey, CA 93943-5101

NDL KAGAKU
C/O KWE-ACCESS
PO Box 300613 (JFK A/P)
Jamaica, NY 11430-0613

OVIEDO LIBRARY
PO BOX 830679
Birmingham, AL 35283

DAVID PAULSEN
E3Compliance
1523 North Joe Wilson Road
Cedr Hill, TX 75104-1437

PENN STATE UNIVERSITY
126 Paterno Library
University Park, PA 16802-1808

DAVID J. PINION
1122 E Pike Street #1217
SEATTLE, WA 98122

KATHERINE SIAKAVARA
Gymnasiou 8
Thessaloniki, Greece 55236

SWETS INFORMATION SERVICES
160 Ninth Avenue, Suite A
Runnemedede, NJ 08078

YUTAKA TANGE
Maizuru Natl College of Technology
234 Shiroya
Maizuru, Kyoto, Japan 625-8511

TIB & UNIV. BIB. HANNOVER
DE/5100/G1/0001
Welfengarten 1B
Hannover, Germany 30167

UEKAE
PO Box 830470
Birmingham, AL 35283

UNIV OF CENTRAL FLORIDA
4000 Central Florida Boulevard
Orlando, FL 32816-8005

UNIVERSITY OF COLORADO
1720 Pleasant Street, 184 UCB
Boulder, CO 80309-0184

UNIVERSITY OF KANSAS –
WATSON
1425 Jayhawk Blvd 210S
Lawrence, KS 66045-7594

UNIVERSITY OF MISSISSIPPI
JD Williams Library
University, MS 38677-1848

UNIVERSITY LIBRARY/HKUST
Clear Water Bay Road
Kowloon, Honk Kong

CHUAN CHENG WANG
8F, No. 31, Lane 546
MingCheng 2nd Road, Zuoying Dist
Kaoshiung City, Taiwan 813

THOMAS WEILAND
TU Darmstadt
Schlossgartenstrasse 8
Darmstadt, Hessen, Germany 64289

STEVEN WEISS
US Army Research Lab
2800 Powder Mill Road
Adelphi, MD 20783

YOSHIHIDE YAMADA
NATIONAL DEFENSE ACADEMY
1-10-20 Hashirimizu
Yokosuka, Kanagawa,
Japan 239-8686

INFORMATION FOR AUTHORS

PUBLICATION CRITERIA

Each paper is required to manifest some relation to applied computational electromagnetics. **Papers may address general issues in applied computational electromagnetics, or they may focus on specific applications, techniques, codes, or computational issues.** While the following list is not exhaustive, each paper will generally relate to at least one of these areas:

- 1. Code validation.** This is done using internal checks or experimental, analytical or other computational data. Measured data of potential utility to code validation efforts will also be considered for publication.
- 2. Code performance analysis.** This usually involves identification of numerical accuracy or other limitations, solution convergence, numerical and physical modeling error, and parameter tradeoffs. However, it is also permissible to address issues such as ease-of-use, set-up time, run time, special outputs, or other special features.
- 3. Computational studies of basic physics.** This involves using a code, algorithm, or computational technique to simulate reality in such a way that better, or new physical insight or understanding, is achieved.
- 4. New computational techniques** or new applications for existing computational techniques or codes.
- 5. “Tricks of the trade”** in selecting and applying codes and techniques.
- 6. New codes, algorithms, code enhancement, and code fixes.** This category is self-explanatory, but includes significant changes to existing codes, such as applicability extensions, algorithm optimization, problem correction, limitation removal, or other performance improvement. **Note: Code (or algorithm) capability descriptions are not acceptable, unless they contain sufficient technical material to justify consideration.**
- 7. Code input/output issues.** This normally involves innovations in input (such as input geometry standardization, automatic mesh generation, or computer-aided design) or in output (whether it be tabular, graphical, statistical, Fourier-transformed, or otherwise signal-processed). Material dealing with input/output database management, output interpretation, or other input/output issues will also be considered for publication.
- 8. Computer hardware issues.** This is the category for analysis of hardware capabilities and limitations of various types of electromagnetics computational requirements. Vector and parallel computational techniques and implementation are of particular interest. Applications of interest include, but are not limited to,

antennas (and their electromagnetic environments), networks, static fields, radar cross section, inverse scattering, shielding, radiation hazards, biological effects, biomedical applications, electromagnetic pulse (EMP), electromagnetic interference (EMI), electromagnetic compatibility (EMC), power transmission, charge transport, dielectric, magnetic and nonlinear materials, microwave components, MEMS, RFID, and MMIC technologies, remote sensing and geometrical and physical optics, radar and communications systems, sensors, fiber optics, plasmas, particle accelerators, generators and motors, electromagnetic wave propagation, non-destructive evaluation, eddy currents, and inverse scattering.

Techniques of interest include but not limited to frequency-domain and time-domain techniques, integral equation and differential equation techniques, diffraction theories, physical and geometrical optics, method of moments, finite differences and finite element techniques, transmission line method, modal expansions, perturbation methods, and hybrid methods.

Where possible and appropriate, authors are required to provide statements of quantitative accuracy for measured and/or computed data. This issue is discussed in “Accuracy & Publication: Requiring, quantitative accuracy statements to accompany data,” by E. K. Miller, *ACES Newsletter*, Vol. 9, No. 3, pp. 23-29, 1994, ISBN 1056-9170.

SUBMITTAL PROCEDURE

All submissions should be uploaded to ACES server through ACES web site (<http://aces.ee.olemiss.edu>) by using the upload button, journal section. Only pdf files are accepted for submission. The file size should not be larger than 5MB, otherwise permission from the Editor-in-Chief should be obtained first. Automated acknowledgment of the electronic submission, after the upload process is successfully completed, will be sent to the corresponding author only. It is the responsibility of the corresponding author to keep the remaining authors, if applicable, informed. Email submission is not accepted and will not be processed.

EDITORIAL REVIEW

In order to ensure an appropriate level of quality control, papers are peer reviewed. They are reviewed both for technical correctness and for adherence to the listed guidelines regarding information content and format.

PAPER FORMAT

Only camera-ready electronic files are accepted for publication. The term **“camera-ready”** means that the material is neat, legible, reproducible, and in accordance with the final version format listed below.

The following requirements are in effect for the final version of an ACES Journal paper:

1. The paper title should not be placed on a separate page.

The title, author(s), abstract, and (space permitting) beginning of the paper itself should all be on the first page. The title, author(s), and author affiliations should be centered (center-justified) on the first page. The title should be of font size 16 and bolded, the author names should be of font size 12 and bolded, and the author affiliation should be of font size 12 (regular font, neither italic nor bolded).

2. An abstract is required. The abstract should be a brief summary of the work described in the paper. It should state the computer codes, computational techniques, and applications discussed in the paper (as applicable) and should otherwise be usable by technical abstracting and indexing services. The word "Abstract" has to be placed at the left margin of the paper, and should be bolded and italic. It also should be followed by a hyphen (–) with the main text of the abstract starting on the same line.
3. All section titles have to be centered and all the title letters should be written in caps. The section titles need to be numbered using roman numbering (I. II.)
4. Either British English or American English spellings may be used, provided that each word is spelled consistently throughout the paper.
5. Internal consistency of references format should be maintained. As a guideline for authors, we recommend that references be given using numerical numbering in the body of the paper (with numerical listing of all references at the end of the paper). The first letter of the authors' first name should be listed followed by a period, which in turn, followed by the authors' complete last name. Use a coma (,) to separate between the authors' names. Titles of papers or articles should be in quotation marks (" "), followed by the title of journal, which should be in italic font. The journal volume (vol.), issue number (no.), page numbering (pp.), month and year of publication should come after the journal title in the sequence listed here.
6. Internal consistency shall also be maintained for other elements of style, such as equation numbering. Equation numbers should be placed in parentheses at the right column margin. All symbols in any equation have to be defined before the equation appears or right immediately following the equation.
7. The use of SI units is strongly encouraged. English units may be used as secondary units (in parentheses).
8. Figures and tables should be formatted appropriately (centered within the column, side-by-side, etc.) on the page such that the presented data appears close to and after it is being referenced in the text. When including figures and tables, all care should be taken so that they will appear appropriately when printed in black and white. For better visibility of paper on computer screen, it is good to make color figures with different line styles for figures with multiple curves. Colors should also be tested to insure their ability to be distinguished after

black and white printing. Avoid the use of large symbols with curves in a figure. It is always better to use different line styles such as solid, dotted, dashed, etc.

9. A figure caption should be located directly beneath the corresponding figure, and should be fully justified.
10. The intent and meaning of all text must be clear. For authors who are not masters of the English language, the ACES Editorial Staff will provide assistance with grammar (subject to clarity of intent and meaning). However, this may delay the scheduled publication date.
11. Unused space should be minimized. Sections and subsections should not normally begin on a new page.

ACES reserves the right to edit any uploaded material, however, this is not generally done. It is the author(s) responsibility to provide acceptable camera-ready files in pdf and MSWord formats. Incompatible or incomplete files will not be processed for publication, and authors will be requested to re-upload a revised acceptable version.

COPYRIGHTS AND RELEASES

Each primary author must execute the online copyright form and obtain a release from his/her organization vesting the copyright with ACES. Both the author(s) and affiliated organization(s) are allowed to use the copyrighted material freely for their own private purposes.

Permission is granted to quote short passages and reproduce figures and tables from and ACES Journal issue provided the source is cited. Copies of ACES Journal articles may be made in accordance with usage permitted by Sections 107 or 108 of the U.S. Copyright Law. This consent does not extend to other kinds of copying, such as for general distribution, for advertising or promotional purposes, for creating new collective works, or for resale. The reproduction of multiple copies and the use of articles or extracts for commercial purposes require the consent of the author and specific permission from ACES. Institutional members are allowed to copy any ACES Journal issue for their internal distribution only.

PUBLICATION CHARGES

All authors are allowed for 8 printed pages per paper without charge. Mandatory page charges of \$75 a page apply to all pages in excess of 8 printed pages. Authors are entitled to one, free of charge, copy of the printed journal issue in which their paper was published. Additional reprints are available for \$ 50. Requests for additional re-prints should be submitted to the managing editor or ACES Secretary.

Corresponding author is required to complete the online form for the over page charge payment right after the initial acceptance of the paper is conveyed to the corresponding author by email.

ACES Journal is abstracted in INSPEC, in Engineering Index, DTIC, Science Citation Index Expanded, the Research Alert, and to Current Contents/Engineering, Computing & Technology.